OAK RIDGE
NATIONAL LABORATORY
MANAGED BY UT-BATTELLE
FOR THE DEPARTMENT OF ENERGY

ORNL/MD/LTR-241
VOLUME 2

Letter Report

Implications of the PIE Results for the 40-GWd/MT-Withdrawal MOX Capsules

S. A. Hodge
L. J. Ott
F. P. Griffin

September 2003

Fissile Materials Disposition Program

UT-BATTELLE
ORNL-27 (4-00)

Revision History

Revision No.	Date Issued	Reason for Revision
0	September 2003	Initial issue of report.

OAK RIDGE NATIONAL LABORATORY

MANAGED BY UT-BATTELLE FOR THE DEPARTMENT OF ENERGY

Nuclear Science and Technology Division
P.O. Box 2009
Oak Ridge, TN 37831-8057
Tel: (865) 574-0573
Fax: (865) 574-8216
hodgesa@ornl.gov

September 12, 2003

Distribution

Implications of the PIE Results for the 40-GWd/MT-Withdrawal MOX Capsules—ORNL/MD/LTR-241, Volume 2

This is a companion document to the *MOX Test Fuel 40 GWd/MT PIE: Final Report,* ORNL/MD/LTR-241, Volume 1, issued in August 2003. Both documents pertain to the post-irradiation examination conducted at the Oak Ridge National Laboratory—Building 3525 hot cells for MOX Test Capsules 4 and 13, withdrawn from the Advanced Test Reactor in March 2002 at a fuel-average burnup of 40 GWd/MT.

Whereas Volume 1 describes how the PIE was conducted and what was seen with little additional comment or analysis, the primary purpose of Volume 2 is to explain the significance of the more important observations. Volume 2 also reports the results of a set of fuel performance calculations performed subsequent to the PIE with model modifications appropriate to the PIE observations.

This is a Level-2 document as defined in the *Fissile Materials Disposition Program Light-Water Reactor Mixed-Oxide Fuel Irradiation Test Project Plan*, ORNL/MD/LTR-78, Revision 2.

Sincerely,

Stephen A. Hodge, Manager
MOX Irradiation Test Project

Distribution:

D. Alberstein, NNSA
S. Basu, NRC
C. Beyer, PNNL
T. Blair, LANL (3)
B. S. Cowell
S. E. Fisher
F. P. Griffin
D. W. Heatherly
W. R. Hendrich
P. Kasik, MPRA
M. Kennard, NAC
R. Y. Lee, NRC
C. R. Luttrell
G. T. Mays
W. J. McAfee
G. E. Michaels
R. N. Morris (3)
D. L. Moses
L. J. Ott
D. J. Spellman
K. R. Thoms
G. A. Meyer, FANP (2)
R. C. Pedersen, INEEL (5)
P. T. Rhoads, NNSA (2)
H. H. Scott, NRC
J. S. Tucker, FANP (2)
Files–SAH–NoRC

ORNL/MD/LTR-241
Volume 2

Implications of the PIE Results for the 40-GWd/MT-Withdrawal MOX Capsules

S. A. Hodge
L. J. Ott
F. P. Griffin

September 2003

Oak Ridge National Laboratory

TABLE OF CONTENTS

Page

LIST OF FIGURES

LIST OF TABLES

ACRONYMS

ADU	Ammonium Diuranate (Process)
ARIES	Advanced Recovery and Integrated Extraction System
ATR	Advanced Test Reactor
AUC	Ammonium Uranyl Carbonate (Process)
BOL	Beginning of Life
BWR	Boiling Water Reactor
CARTS	Capsule Assembly Response—Thermal and Swelling (Code)
EFPD	Effective Full Power Days
FMDP	Fissile Materials Disposition Program
GWd/MT	Giga-Watt Days per Metric Ton
HYDOX	HYDride-OXidation metal-to-oxide conversion
INEEL	Idaho National Engineering and Environmental Laboratory
LANL	Los Alamos National Laboratory
LHGR	Linear Heat Generation Rate
LWR	Light Water Reactor
MCNP	Monte Carlo N-Particle (Code)
Mil	0.001 inch
MOX	Mixed Oxide
MOCUP	MCNP-ORIGEN2 Coupled Utility Program
MPa	Mega-Pascal
NRC	Nuclear Regulatory Commission
ORNL	Oak Ridge National laboratory
PIE	Postirradiation Examination
PNNL	Pacific Northwest National Laboratory
PPB	Parts Per Billion
PPM	Parts Per Million
PWR	Pressurized Water Reactor
RG	Reactor Grade
RMAL	Radioactive Materials Analysis Laboratory
WG	Weapons Grade

EXECUTIVE SUMMARY

Mixed-oxide (MOX) fuel prepared with plutonium derived from one or more weapons components is being irradiated in the Advanced Test Reactor (ATR) at the Idaho National Engineering and Environmental Laboratory (INEEL). This irradiation is proceeding under conditions more severe than will be encountered by fuel in the commercial reactors participating in the Fissile Materials Disposition Program. The plutonium-rich agglomerates within the test fuel are larger than those found in modern commercial MOX fuel in Europe. Gallium was introduced with the plutonium component and is present within the test fuel at 1–5 PPM. This test irradiation contributes experience with irradiation of gallium-containing fuel and, more generally, demonstrates the utilization of plutonium derived from weapons components in a light water reactor environment.

The post irradiation examination (PIE) performed for the two test capsules withdrawn in March 2002 is described in the companion *MOX Test Fuel 40 GWd/MT PIE: Final Report* (ORNL/MD/LTR-241, Volume 1), issued in August 2003. The observations reported in Volume 1 provide *prima facie* evidence that this weapons-derived fuel continues to perform in an acceptable manner similar to the European experience with reactor-grade MOX fuel. In addition, there is no evidence of any significant gallium migration from fuel to clad.

This Volume 2 to the final PIE report for the capsules withdrawn at 40 GWd/MT burnup is intended to explain the significance of the more important observations. Whereas Volume 1 describes how the PIE was conducted and what was found with little additional comment or analysis, Volume 2 examines the ramifications of these findings. These include the fission gas release fractions, the size and state of the plutonium-rich agglomerates, the appearance of halos surrounding these agglomerates, the extent of fuel densification and swelling, oxidation of the cladding inner surface, outward clad creep, and the presence of primary ridging at the clad sections overlying the pellet-pellet interfaces.

Fission Gas Release Fractions

Following puncture (drilling) of the fuel pin upper end cap, gas release fractions are determined by measuring the Krypton-85 activity of the released gas. (The fission gas release fraction is this activity divided by the ORIGEN-calculated total Kr-85 activity.) A check is provided by simultaneous measurement of the pressure in the post-puncture combined fuel pin and collection chamber, which can be compared with the expected pressure based on the gas release fraction derived from Kr-85 activity.

In view of a discrepancy in the initial fuel pin pressure check, the methods by which fission gas release fractions and fuel pin pressures are calculated were carefully scrutinized and several corrections were identified. These were applied not only to the gas release fractions for the current PIE, but also to those determined in previous PIEs (for which the adjustments were much smaller). With all corrections in place, the release fractions determined from the measured Krypton-85 activities for the four fuel pins withdrawn previously (with burnups of 21 and

30 GWd/MT) range from 0.013 to 0.023. These fuel pins occupied symmetric positions with respect to the ATR core during the irradiation and hence experienced similar linear heat generation rates (Phase II average 8.2 kW/ft; 9.7 kW/ft maximum). Thus, it is not surprising that their gas releases should fall within a range this narrow.

The fission gas release fractions for the two fuel pins withdrawn at 40 GWd/MT are four to five times larger. This is attributed to the significantly higher LHGRs (and fuel temperatures) that these pins encountered. Here the average linear heat generation rate (LHGR) during Phase II was about 9.1 kW/ft with a maximum of about 10.7 kW/ft. These pins occupied symmetric positions within the test assembly throughout their irradiation and have fission gas release fractions of 0.084 and 0.095, respectively.

One fuel pin in each withdrawn pair was prepared with PuO_2 powder subjected to the Thermally Induced Gallium Removal (TIGR) process, so that most of the gallium was removed before pellet sintering. The average gallium content of the TIGR-treated fuel is about 1.3 PPM. For the fuel pins prepared with untreated powder, most of the gallium was driven off during pellet sintering, leaving an average MOX gallium content of about 3.0 PPM.

While carrying out its primary purpose of gallium removal, the TIGR process also affects the powder (and pellet) morphology. Treatment at the temperatures (about 1200°C) for which the TIGR process is effective tends to increase the particle size while greatly reducing the specific powder surface area. The fission gas release percentages (1.88%–2.30%–9.51%) observed for the TIGR-treated fuels in the successive (21, 30, and 40 GWd/MT) PIEs are greater than those observed (1.32%–1.47%–8.37%) for their untreated counterparts. It is certainly plausible that the pre-sintering changes in particle characteristics associated with the TIGR process are contributing to the observed differences in fission gas releases between the TIGR-treated and untreated fuels.

Although greater than one percent, the fission gas releases for these weapons-derived MOX test fuel pins are low in comparison to the European experience for mixed-oxide fuel with similar irradiation histories. Until about ten years ago, it was common practice to plot measured fission gas release fractions against the final burnups of the associated fuels. In general, this approach is characterized by wide scatter in the plotted points. Beginning in about 1993, it has become generally recognized that the fission gas release fraction has a much stronger dependence on the maximum temperature experienced by the fuel than on the accumulated burnup. Review of the recent literature provides ample evidence that fission gas release fractions are proportional to and increase linearly with the highest LHGR experienced by the fuel.[*]

Recent papers and journal articles provide good discussions of the mechanisms for fission gas release in MOX fuel. Only a small portion of the fission gas generated during irradiation (corresponding to the solubility limit) is retained in the fuel matrix. Most fission gas accumulates in the pores of the plutonium-rich agglomerates or intragranularly in adjacent

[*]The release of fission gas is largely controlled by diffusion of the gas atoms, whose mobility (diffusivity) increases exponentially with temperature. Thus, fission gas release fraction is largely determined by the maximum temperature experienced by the fuel, and a short period at high temperature has a much greater impact than a long period at a low temperature.

grains, and release to the fuel pin free volume requires the development of a system of escape tunnels along the grain boundaries in the surrounding UO_2 matrix. High temperatures cause these tunnels to open, and the extent of the associated escape pathways depends on the highest local temperature that has been experienced.

Given that the measured fission gas release fractions exceed one percent, it is of interest to compare the irradiation experience of the current test fuel pins with the Halden criterion to check whether or not this is an expected result. The Halden Threshold, dating from 1979 and recently modified (lowered) for burnups greater than 22 GWd/MT, is an experimentally-derived curve of pellet centerline temperature versus burnup. If a superimposed trace of actual pellet centerline temperatures rises above this reference curve, then fission gas fractions greater than one percent are to be expected.

In making comparison to the Halden Threshold, it is important to recognize that the measured gas release fractions are actually averages for the fifteen pellets held within each fuel pin. Each initial pellet-to-clad gap can lie anywhere within the range afforded by the pellet and cladding fabrication tolerances, and the width of each gap affects the effective thermal conductance between pellet and cladding. Therefore, it is expected that the individual pellets have, for the same LHGR, different traces of calculated centerline temperatures.

For the 40 GWd/MT withdrawal capsules, the range of pellet centerline temperature traces has been defined by two bounding calculations based on the minimum and the maximum initial pellet-clad gaps. Gas releases of greater than one percent are indicated for both cases. The Halden Threshold is exceeded twice, first during nearly all of irradiation Phase II and later at burnups over 35 GWd/MT, just before withdrawal of these capsules for PIE. Thus, the measured gas releases conform to the Halden criterion and are considered normal for this irradiation experience.

Plutonium-Rich Agglomerates

Early MOX fuel was prepared by directly comilling the PuO_2 and UO_2 powders. The resulting fuel was heterogeneous, with the PuO_2 particles everywhere completely distinct from the UO_2. This “reference” process was used until about 1985, when it was generally abandoned due to inadequate solubility in nitric acid and the undesirable impact of this upon fuel reprocessing.

Several methods to improve MOX homogeneity have been developed in the last two decades, including the Short Binderless Route (SBR) in England, the Optimized Co-Milling (OCOM) in Germany, and the MIcronized MASter blend (MIMAS) process in Belgium and France. The weapons-derived MOX fuel being irradiated in the current test was prepared in a manner similar to the MIMAS fabrication process.

The MIMAS process is predicated on use of a master mix comprising all of the PuO_2 and a fraction of the UO_2. These two powders are simultaneously milled for several hours to produce an intimate mixing. The milling also modifies the powder physical characteristics (surface area, density, flowability) while electrostatic forces cause self-agglomeration. After sieving, the

master mix is blended with the remainder of the UO_2 to form the secondary blend, from which the pellets are pressed.

It is important to recognize that only a portion of the UO_2 (that in the master mix) undergoes milling in MIMAS. Thus, the physical characteristics (especially flowability) of the UO_2 powder introduced to surround the PuO_2-rich agglomerates in the secondary blend are preserved. A free-flowing press feed for automated die fill is achieved without precompaction or granulation of the MOX powders.

The MOX fuel for the current irradiation test was fabricated during 1997 at Los Alamos National Laboratory (LANL). This fuel comprises five percent PuO_2 and 95% depleted UO_2, the latter converted by the ammonium diuranate (ADU) process. All of the PuO_2 was introduced as 31% of the master mix. Thus, each 100 grams of the test MOX fuel includes five grams of PuO_2 and 11.11 grams of UO_2 that were milled together to form the master mix. This milling reduced the PuO_2 particle size while promoting a homogeneous dispersion of the PuO_2 particles in the UO_2. Employing a mixer/blender that does not alter particle characteristics (as does milling), these 16.11 grams of master mix were then diluted into the remaining 83.89 grams of depleted UO_2.

The plutonium concentration within the agglomerates is higher than the MOX fuel average, but does not exceed that of the master blend, which for the current test fuel has a plutonium concentration of 31%.

It was not intended that the secondary blending (dilution) process by which the plutonium-rich agglomerates are distributed into the matrix of depleted UO_2 be carried to completion. On the contrary, it is necessary to maintain the flowability of the UO_2 by limiting the energy input to the powders. However, the secondary blending of the current test fuel was not as effective as desired in dispersing the master mix into the UO_2 matrix. Relatively large residual agglomerates of the master mix are evident in the final fuel. The Pellet Processing Data packages prepared at Los Alamos subsequent to the test fuel fabrication indicate an average measured area fraction of about 1.5% for plutonium-rich agglomerate equivalent diameters greater than 400 microns. During irradiation, these agglomerates swell due to the accumulation of both solid and gaseous fission products. At 40 GWd/MT, the largest of the visible agglomerates have equivalent diameters in the 500–600 micron range.

Literature values for modern European commercial fuels indicate postirradiation agglomerate maximum equivalent diameters in the range of 250 to 400 microns for fuel average burnups in the vicinity of 45 GWd/MT. Thus, the current PIE results (and the measured preirradiation sizes) indicate that this test fuel began irradiation with a greater fraction of large agglomerates than is normally encountered in modern mixed-oxide fuels.

Two reasons are cited in the literature for limiting the size of plutonium-rich agglomerates. The first is to facilitate dissolution during reprocessing. Although there were no performance problems with the early simple fuel mixtures, steps were taken to introduce a master-mix and to minimize the size of the plutonium-rich agglomerates in order to improve the solubility of the irradiated fuel for reprocessing purposes. Facility of reprocessing (fuel solubility) is not among the goals of the FMDP mission.

The second reason for limiting agglomerate size, more pertinent to the current test irradiation, is the supposition that large agglomerates may tend to increase fission gas release. There has been no precise quantification of this in European fuel, and experimental investigations have detected no significant effects upon gas release for different agglomerate volume fractions and plutonium concentrations irradiated under the same conditions, or for different radial locations within the fuel. There is also no evidence of an increased gas release for the current test, although the capsules have reached 40 GWd/MT and the agglomerates are large relative to those of modern European fuel. Gas release will again be monitored when this test fuel reaches 50 GWd/MT.

When evaluating the extent of irradiation for a mixed-oxide fuel prepared with a MIMAS-type fabrication process, it is important to recognize that two additional burnups, besides the fuel-average burnup, are appropriately defined. These are the burnup within the plutonium-rich agglomerates and the much smaller burnup within the surrounding matrix of depleted uranium. For the current test fuel in the earliest stages of irradiation, it is reasonable to make the approximation that all of the fissions occur within the agglomerates and none within the surrounding depleted UO_2 matrix. About one-sixth of the total fuel mass resides within the agglomerates. Since burnup (GWd/MTHM) is the ratio of energy release to fuel mass, the burnup rate within the agglomerates is initially about six times that of the fuel average. At 2 GWd/MT for the mixed oxide, the burnup within the agglomerates is approximately 12 GWd/MT.

The ratio of agglomerate burnup to fuel-average burnup is reduced as irradiation proceeds due to the creation of fissionable isotopes (principally Pu-239) within the depleted uranium matrix. Calculations performed at INEEL based on the current test fuel provide estimates of the agglomerate and matrix burnups as functions of the local fuel average burnup. The agglomerates reach 60 GWd/MT when the average burnup is about 18.3 GWd/MT. At a predicted fuel average burnup of 40 GWd/MT, the associated burnups are 100 GWd/MT for the agglomerates and 28.4 for the UO_2 matrix.

High burnup within the plutonium-rich agglomerates is accompanied by considerable local swelling induced by the accumulated solid and gaseous fission products. Whereas the solid fission products stay with an agglomerate throughout fuel life, the fate of the fission product gases depends upon the temperature during irradiation of the region in which the agglomerate is located. In this connection, it is important to recognize that even the largest agglomerates are still sufficiently small that their internal temperatures only slightly exceed that of the immediately surrounding UO_2 matrix.

Agglomerates become highly visible when they have transformed into a “high burnup structure.” In general, a high burnup structure (small grains with a few large pores) evolves during irradiation when the local temperature is less than 1000°C and the local burnup exceeds about 60 GWd/MT. Prior to transformation, much of the fission gas is stored in nanometer-size cavities within the approximately 10-micron fuel grains. Subsequent to transformation, the grains are in the 0.5 to 1.0 micron range, in a structure interspersed with relatively large gas storage pores. Much of the gas displaced from the very small intragranular cavities is collected (at high pressure) in the facetted pores in the recrystallized microstructure.

Agglomerates in the outer regions of the MOX test fuel mount surfaces are clearly visible due to their high-burnup structure. The halos surrounding these agglomerates are fission gas in surrounding UO_2 grains, which either diffused (primarily athermally) prior to transformation or was displaced when the high burnup structure was formed. Faint agglomerate outlines can be discerned in the central regions of these fuel surfaces at a fuel-average burnup of 40 GWd/MT. These are the beginnings of the transformation to high-burnup structure for these agglomerates. Transformation of the agglomerates in the central region was delayed due to temperatures greater than 1000°C in the central region earlier in the irradiation.

No evidence of recrystallization was found in the fuel matrix around the pellet circumference. Although the rim area experienced low temperature and local burnups higher than the average for the depleted UO_2 matrix (the "rim effect"), rim area burnup obviously did not reach 60 GWd/MT. It is expected that some high-burnup structure will be observed along the outer rim at the next PIE, i.e., at a fuel-average burnup of 50 GWd/MT.

Clad Inner Surface Oxidation

Fuel and surrounding clad from the vicinity of the upper end of Pellet 2 in both 40 GWD/MT fuel pins were examined by SEM and EPMA. Areas of particular interest in both examinations were the "halos" (fission gas storage regions) surrounding the large agglomerates within the pellet and the nature of the corrosion layers intermittently located along the pellet-clad interface. Both fuel pin mounts exhibit corrosion layers along the portions of the clad inner surface where the fuel was in contact with the clad during irradiation.

The uneven and noncontiguous nature of the corrosion observed on the cladding inner surfaces is an artifact of the manner in which the pellet fragments came into contact with the cladding during irradiation. Inner surface oxidation requires that excess oxygen be available and that the fuel be in contact with the cladding to provide a path for solid-state athermal diffusion of the oxygen atoms. The thicker oxidation layers over the agglomerates follow directly from the narrower local pellet-clad gaps during irradiation. The observed clad corrosion patterns are in accordance with expectations based on U.S. and European experience with both UO_2 and MOX fuels.

Fuel Densification and Swelling

The Fuel Pin Measuring Apparatus (FPMA) developed at ORNL for this project provides a precise determination of the clad outer diameter profile. The clad outer diameter serves as the anchor point for derivation of the clad inner diameter, which, when compared to the measured pellet outer diameter, yields the pellet-clad gap.

Comparison of the clad and pellet dimensions as determined for successively higher burnups establishes the history of pellet swelling and clad creep as experienced during this test irradiation. For each of the four capsule withdrawals to date, the capsule and fuel pin metrological results were combined with measurements made directly (Imaging software) from photographic enlargements of the metallographic mounts to determine the clad thickness and internal diameter, the pellet outer diameter, and the effective gap between pellet and clad.

Fuel behavior (cracking, densification, and swelling) is found to be normal and prototypic of commercial MOX fuel. The cladding experienced an irradiation-assisted outward creep under the impetus of a tensile wall (hoop) stress that increased from zero to about 5 MPa as fuel pin internal pressure increased during the irradiation. (It should be noted that this clad movement differs from normal PWR behavior, where clad creep down is imposed by high external coolant pressure.) The outward clad creep (about 0.2%) observed in the current test is normal for the test fuel operating conditions and accumulated burnup, and is compatible with the experience documented in the literature.

The experiment-specific Capsule Assembly Response—Thermal Swelling (CARTS) code developed at ORNL for application to this test irradiation has been employed to provide the component temperature and pellet swelling histories necessary to facilitate interpretation of the PIE observations. Fuel swelling models are derived from those utilized in the NRC-sponsored FRAPCON-3 code. The user specifies the duration and extent of the fuel densification and the code calculates the swelling and net changes in pellet dimensions. (In effect, densification acts as a temporary period of negative swelling.)

CARTS code predictions accurately reproduce the swelling history (to 40 GWd/MT) for this fuel. For these simulations, the fuel densification parameters were varied until a best fit to the PIE data emerged. The best-fit parameters are 2% densification complete by 10 GWd/MT burnup. It is important to recognize that the goal is not to accurately identify densification *per se*, but rather to specify the densification parameters that, when combined with the code positive swelling models, best reproduce the observed pellet dimensional changes.

Pellet Hourglassing

The fuel pin outer diameter profiles measured by the FPMA exhibit local ridging (average radial height about 0.14 mil) over the pellet-to-pellet interfaces at all four burnup levels. This type of local clad deformation (denoted “primary ridging”) is commonly observed in commercially irradiated LWR fuel. The cause is differential thermal expansion within the fuel—the pellet centerline is much hotter than the outer cylindrical surface and expands axially to a greater extent. The pellets crack into pie-shaped segments, and the differential expansion in the axial direction causes these segments to warp into hourglass shapes.

The high coolant pressure in commercial PWRs causes inward creep of the cladding, which eventually comes into hard contact with the fuel over the pellet interfaces, where the hourglassing produces the largest (deformed) pellet diameters. The clad primary ridges are therefore artifacts of the hourglass (or saddle) shape of the underlying pellets.

Formation of ridges in the MOX test fuel pins is somewhat different than in commercial fuel, because of the outward pressure differential across the cladding. Although the clad does not creep inward in this test, localized contact between pellet and clad still occurs because the fuel pins were designed to have initial pellet-clad radial gaps (1.5 mil) much smaller than found in commercial fuel (3–4 mil). Here the pellet differential thermal expansion was sufficient to cause hourglass-enhanced local contact with the cladding at initial heatup. This hard contact over the pellet-to-pellet interfaces occurred before any fuel densification or swelling.

ABAQUS code finite-element calculations performed for the zero-burnup initial heatup with as-built dimensions for the pellet, fuel pin, and capsule, and with the actual initial linear heat generation rate are documented for the capsules withdrawn at 30-GWd/MT burnup. These calculations (not repeated for the 40 GWd/MT withdrawal) clearly predict pellet hourglassing (due to a greater axial thermal expansion along the pellet centerline) with clad contact at the pellet ends. The applied stress is sufficient to induce local yielding. This explains the small local cladding deformations ("primary ridges") measured in the PIEs.

To recap, ridging is predicted to have occurred on initial heatup at zero burnup. Primary ridging is commonly observed in PWR fuel, and does not constitute a mechanism for failure during normal operation. There is no indication in the PIEs for the current test fuel that such localized contact has had any detrimental effect on cladding integrity. The mission fuel will have larger initial gap widths and lower LHGRs, and hence will not experience clad deformation due to hourglassing either as early or to the extent observed in this test irradiation.

Overall Assessment of Fuel Performance Based on PIE Findings

This mixed-oxide test fuel continues to perform well. There is nothing in the current PIE findings that challenges the adequacy of the safety analyses carried out for the Phase-IV irradiation, which extends the planned burnup to 50 GWd/MT. Pellet temperatures will remain far below the fuel melting point. Clad contact will be limited to locations overlying the pellet-pellet interfaces corresponding to the hourglass shape assumed by the pellets under thermal expansion. Fission gas release and the associated clad wall tensile stress will continue to induce outward clad creep. Fuel swelling is normal, and pellet-clad contact is not expected at the pellet midplane. The gap between fuel pin and stainless steel capsule will remain open.

This test irradiation involves axial power generation rates higher than normal for commercial MOX fuel. There has been no indication of any significant relocation of gallium from fuel to cladding. Subsequent to the withdrawal of the remaining three capsules at 50 GWd/MT, the situation with respect to gallium transport will again be thoroughly analyzed.

Finally, it is important to recall that the mission fuel for the Fissile Materials Disposition Program will be improved relative to that employed in the test fuel pins discussed here. Use of modern fuel fabrication techniques will increase the PuO_2 homogenization within the mission fuel and reduce agglomerate size. Design and operational provisions will tend to reduce fission gas release fractions. The improved heat transfer afforded by clad creep down (instead of outward clad movement) will serve to reduce the pellet temperatures at comparable linear heat generation rates. Further, the power levels during mission fuel lifetime will be lower than those experienced by the weapons-derived MOX fuel irradiated in the current test.

ABSTRACT

This second volume of the Post Irradiation Examination (PIE) Report, ORNL/MD/LTR-241, discusses the implications of the observations obtained for the two MOX test capsules withdrawn from the ATR in March 2002 with burnups close to 40 GWd/MT. These PIE observations include the fission gas release fractions, the size and state of the plutonium-rich agglomerates, the appearance of halos surrounding these agglomerates, the extent of fuel densification and swelling, oxidation of the cladding inner surface, and the presence of primary ridging at the clad sections overlying the pellet-pellet interfaces. A model is presented for the outward clad creep as observed in this test irradiation. The bases for CARTS code modifications implemented toward a more accurate representation of the PIE findings are discussed, as are the results of new calculations of fuel conditions obtained with these modifications.

Implications of the PIE Results for the 40-GWd/MT-Withdrawal MOX Capsules

1. INTRODUCTION

The *MOX Test Fuel 40 GWd/MT PIE: Final Report,* ORNL/MD/LTR-241, Volume 1, describes the postirradiation examination performed on Capsules 4 and 13, which were withdrawn from the ATR in March 2002. Volume 1 explains how the PIE was conducted and presents the findings with limited additional comment and analysis. This companion Volume 2 complements that information by discussing the significance of the more important observations such as the fission gas release fractions, the plutonium-rich agglomerates, clad oxidation, fuel densification and swelling, and outward clad creep.

Chapter 2 addresses the measured fission gas release fractions and the significance of their magnitudes with respect to the European MOX fuel experience. The preparation of plutonium-rich agglomerates by the master-mix process and the particular characteristics of these agglomerates in the irradiated MOX test fuel as observed in the current PIE are discussed in Chapter 3.

Heavy metal oxide fission releases oxygen within the fuel. Most is taken up by fission products or by increasing the oxygen potential of the remaining heavy metal oxides, but one effect is cladding inner surface corrosion, which is discussed in Chapter 4. (There is no oxidation at the cladding outer surface, which remains in a helium atmosphere throughout the irradiation.)

The fuel swelling and densification history is derived by reviewing the changes in pellet dimensions from the initial unirradiated state through the successive PIEs conducted at burnups of 9, 21, 30, and 40 GWd/MT. Determination of the pellet structural changes depends in turn upon understanding the changes in cladding dimensions including the effects of outward clad creep as experienced during this test irradiation. These analytical processes and their results are discussed in Chapter 5.

The increases in cladding diameter associated with outward clad creep have been observed in all PIEs conducted to date for this MOX test fuel. This is contrary to the commercial fuel experience, where the cladding creeps inward under the impetus of coolant pressure. The development of a model to represent clad creep for this test irradiation is described in Chapter 6.

Chapter 7 reports the results of a set of fuel performance calculations performed subsequent to the PIE to illustrate the actual performance of Capsules 4 and 13 during irradiation. To this end, the code input for these calculations has been based specifically upon the PIE observations for these capsules.

The overall purpose of this PIE is to evaluate the performance of this weapons-derived MOX test fuel. The implications of the PIE findings have been discussed in this report. The conclusions with respect to fuel performance are summarized in Chapter 8.

Chapter 9 comprises the references cited in this report.

2. FISSION GAS RELEASE WITH COMPARISON TO EUROPEAN EXPERIENCE

2.1 Introduction

This Chapter addresses the fission gas release determinations for Fuel Pins 7 and 16 (Capsules 4 and 13). The method depends upon measurement of the Krypton-85 activity within the fuel pin free volume. To obtain this measurement, each capsule was mounted vertically with the upper end cap trimmed to reduce the path length into the capsule upper plenum. The vacuum-sealed drill press apparatus described in Reference 1 was then employed to drill downward through the capsule upper end cap. The capsule pressure and any Krypton-85 activity were recorded to identify any leakage that may have occurred from the fuel pin. (No such leakage has been found in any of the capsules drilled to date.) Subsequently, the drill was advanced through the fuel pin upper end cap to permit measurement of the pressure and Krypton activity in the pin upper plenum and connected free volume.

The fission gas release fraction is the Krypton-85 activity in the gas collected from the fuel pin divided by the total activity of this isotope within the pin. The results for Fuel Pins 7 and 16 are discussed in Section 2.2. These release fractions have been checked by use of the pin pressure before puncture as derived from the pressure measured (post-puncture) for the combined fuel pin and collection chamber. As described in Section 2.3, this check is obtained by comparing this measurement-derived fuel pin pressure with the expected pressure based on the fission gas release fraction.

Several corrections to the gas release fraction determination and check methodology were identified and implemented during the performance of the current PIE. These are discussed in Section 2.4, where updated results for all PIEs conducted to date are presented.

The fission gas release fractions obtained for Fuel Pins 7 and 16 are compared with the applicable European data in Section 2.5. To establish that these release fractions conform to expectations based upon their irradiation histories, the pellet centerline temperatures are compared with the Halden empirical threshold (for one percent gas release) in Section 2.6. Finally, Section 2.7 provides a discussion of the main points and the conclusions of this Chapter.

2.2 Fission Gas Release Per Krypton-85 Activity Ratio

Krypton-85 is a reliable fission gas release marker because it is created within the fuel only by fission, and has a half-life (about ten years) sufficiently long to make quantitative measurements feasible and practical. The measurements and associated fission gas release fraction determinations for Fuel Pins 7 and 16 are discussed in Chapter 4 of Volume 1. Briefly, the total Kr-85 activity present in the fuel pin after shutdown was obtained via an ORIGEN code run conducted at INEEL. This total (as of the time that the fuel pin was opened) was then divided into the activity present in the gas collected from the pin free volume. The resulting gas release ratio for Krypton-85 is a good approximation to the overall fission gas release fraction.

As explained in Reference 2, the process of diffusion is slowed somewhat for a gas undergoing radioactive decay. Basically, decay of the inventory remaining within the fuel lowers the gas concentration gradient for subsequent diffusion. Practically speaking, this means that the gas release fraction for Krypton-85 is slightly lower than the gas release fraction for the stable fission gas isotopes. For the 40-GWd/MT withdrawals irradiated for 2.5 years, the diffusion of Krypton-85 (10.7 year half-life) is 0.984 of what it would be without decay. Thus, the reduction is very small. Further, gas release in MOX fuel is not a pure diffusion mechanism; hence, this small correction factor has not been applied.

The fission gas release fractions for Capsules 4 and 13 (withdrawn at 40 GWd/MT) are listed in Table 2.1. The corresponding values for the 30-GWd/MT Capsules 3 and 10 and the intermediate-withdrawal (21 GWd/MT) Capsules 2 and 9 are included for comparison. These gas release fractions are considered accurate to within ±8% of the listed values.

Table 2.1. Fission Gas Release Fractions for the MOX Test Capsules Derived from Measured Kr-85 Activities

Parameter	Intermediate Withdrawal		30 GWd/MT Withdrawal		40 GWd/MT Withdrawal	
Capsule number	2	9	3	10	4	13
Fuel pin number	5	12	6	13	7	16
Kr-85 activities						
Collected (mCi)	3.78	5.37	5.65	9.01	39.61	44.78
Total created (mCi)	287	286	385	391	473	471
Implied fission gas release fraction	0.0132	0.0188	0.0147	0.0230	0.0837	0.0951

2.3 Gas Release Check Per Measured Fuel Pin Pressure

The free volume gas inventory is the sum of the helium initially loaded plus the released portions of the fission gases (krypton and xenon) and of the helium created within the fuel during the irradiation. [Other gases may be present in trace (negligible) quantities.] Knowledge of the fuel pin free volume and its gas content permits use of the perfect gas law to find the corresponding pin total pressure. This can then be compared with the measured fuel pin pressure.

2.3.1 Fuel Pin Free Volume

For the MOX test fuel pin design, the sum of the nominal cold volumes of the gas plenum, the pellet dish and chamfer cutouts, and the pellet-clad gap is derived as demonstrated in Appendix A of Reference 3. Using actual radial dimensions for fuel and clad, these sums are 1.066 and 1.045 cm^3 for Fuel Pins 7 and 16, respectively. During irradiation, the combined effects of fuel densification and clad expansion tend to increase these free volumes, while fuel thermal expansion and swelling tend to counteract these effects. The fuel pin free volume at the time that the gas measurement is taken is estimated by application of the CARTS code (described in Chapter 7).

Fuel Pins 7 and 16 have initial pellet stack lengths (5.816 and 5.790 in.) shorter than nominal (6.00 in.). The corresponding initial (preirradiation) free volumes were, therefore, larger than the nominal, at 1.318 and 1.333 cm^3, respectively. Subsequent to irradiation to 39.9 GWd/MT burnup, these free volumes were calculated to be 1.317 cm^3 for Fuel Pin 7 and 1.347 cm^3 for Fuel Pin 16 (for which outward clad creep was greater, as discussed in Chapter 5).

Subsequently, the Fuel Pin 7 free volume was measured by gas backfill (employing the apparatus described in Reference 4) as 1.326 cm^3, which is within 1% of the calculated estimate. As explained in Volume 1, this backfill technique could not be applied to Pin 16 because of upper end cap damage incurred when the Krypton-85 activity was measured.

2.3.2 Fission Gas in Pin Free Volume

The amount of fission gas created is taken from the ORIGEN runs performed at INEEL. Multiplying by the fission gas release fraction then yields the fission gas inventory in the fuel pin free volume. For Fuel Pin 7, the calculated fission gas generation (krypton plus xenon) at the time of puncture is 410.3E-5 mole. With a fission gas release fraction of 0.0837, the fission gas inventory in the fuel pin free volume is 34.34E-5 mole. This is listed as Item c in Table 2.2.

Table 2.2. Calculated Fuel Pin Pressure as Derived from Fission Gas Release Fraction for Fuel Pin 7

	Parameter	Value	Uncertainty or Range
a.	Fission gas release fraction	0.0837	0.0770–0.0904
b.	Fission gas created (x 10^{-5})	410.3 mole	None Assumed
c.	Fission gas in free volume (x 10^{-5})	34.34 mole	31.60–37.09 mole
d.	Helium initially loaded (x 10^{-5})	4.046 mole	3.865–4.236 mole
e.	Created helium released (x 10^{-5})	3.037 mole	1.518–4.555 mole
f.	Total free volume gas (x 10^{-5})	41.42 mole	36.98–45.88 mole
g.	Fuel pin free volume	1.326 cm^3	±1.2%
h.	Gas temperature	308.2 K	±2.7%
i.	Calculated pressure	116.1 psia	99.64–133.7 psia
j.	Measured pressure	114.8 psia	—

The corresponding values for Fuel Pin 16 are listed in Table 2.3. The gas release fraction from Kr-85 activity measurement is 0.0951 (Item a), while the ORIGEN-calculated total fission gas generation is 411.7E-5 mole (Item b). The fission gas inventory in the fuel pin free volume (Item c) is then 39.15E-5 mole.

2.3.3 Helium—Initially Loaded

The helium in each fuel pin free volume derives from two primary sources. The first is the initial charge introduced within the fuel pin (at atmospheric pressure) when the end caps were closed (welded) at Los Alamos National Laboratory (LANL). The pressure exerted by this helium fill gas during capsule irradiation has been considered in the Safety Analyses for this experiment as discussed in Chapter 5 of Reference 3. Applying the perfect gas law with the estimated

Table 2.3. Calculated Fuel Pin Pressure as Derived from Fission Gas Release Fraction for Fuel Pin 16

	Parameter	Value	Uncertainty or Range
a.	Fission gas release fraction	0.0951	0.0875–0.1030
b.	Fission gas created ($\times 10^{-5}$)	411.7 mole	None Assumed
c.	Fission gas in free volume ($\times 10^{-5}$)	39.15 mole	36.02–42.28 mole
d.	Helium initially loaded ($\times 10^{-5}$)	4.091 mole	3.909–4.282 mole
e.	Created helium released ($\times 10^{-5}$)	3.178 mole	1.589–4.767 mole
f.	Total free volume gas ($\times 10^{-5}$)	46.42 mole	41.52–51.33 mole
g.	Fuel pin free volume	1.347 cm^3	±1.8%
h.	Gas temperature	308.2 K	±2.7%
i.	Calculated pressure	128.1 psia	109.6–148.1 psia
j.	Measured pressure	134.8 psia	—

(Reference 5) LANL atmospheric pressure of 11.1 psia and glove box temperature of 80°F, the helium fill was 4.046E-5 mole for the initial free volume of 1.318 cm^3 in Fuel Pin 7. For Fuel Pin 16, 4.091E-5 mole helium was loaded into the initial free volume of 1.333 cm^3. These initial helium fills are listed as Item d in Tables 2.2 and 2.3, respectively.

2.3.4 Helium Created During and After Irradiation

The second primary source for the helium present in the free volumes when the fuel pins are opened is by creation within the fuel during and after irradiation. Most of the helium created within the fuel is formed via alpha-decay of the higher mass-number elements formed by successive transmutation of plutonium. Other sources, which include alpha particles formed by ternary fission and an (n, alpha) reaction between O-16 and fast neutrons, are relatively small. The helium created within the fuel is subject to diffusion and subsequent release from the fuel matrix. Information concerning the production and potential for release of this created helium is available in References 6 through 9.

Curium-242 is the major (90%) contributor to helium production by alpha decay. Its prominence derives from its half-life of 163 days, which is short relative to the half-lives of the competing transuranic elements. Because the transmutation chain to Cm-242 is shorter when plutonium is irradiated, the helium production rate in MOX is about four times the rate in UO_2 (Reference 8).

In general, release of the helium created within the fuel matrix is negligible in commercial PWR fuel due to the high partial pressure [25 bar (360 psia) cold] exerted by the initially charged helium in the fuel rod free volume. On the contrary, it is more probable that some of the initial fill gas will be absorbed or taken up within the PWR fuel matrix. Some helium release is observed in BWR rods, for which the initial fill gas pressure is lower.

For design conditions such as employed for the current MOX irradiation test fuel pins, where the initial helium charge was inserted at atmospheric pressure, release of created helium from the fuel matrix is expected. The amount of helium created is easily obtained from the ORIGEN calculations performed for this experiment at INEEL. For the times after shutdown at which the pins were punctured, these values are 6.073E-5 mole for Fuel Pin 7 and 6.356E-5 mole for Fuel

Pin 16. The next step is to consider what fraction of this created helium should be assumed to be released from the fuel matrix. The limited information on helium release from fuel available in the literature is primarily from Japanese researchers (References 8 and 9).

The mechanisms for helium release from fuel are discussed in Reference 8. Although helium diffuses about 30 times faster than xenon, diffusion to the free volume is not the major factor in helium release, primarily because of the long path lengths involved. Rather than migrating directly to a free volume boundary, it is more likely that the diffusing helium will intersect and coalesce with the existing fission gas bubbles located within the matrix and along the internal grain boundaries. In general, faster-diffusing helium atoms reach and reside within porosity originally created by the fission gases. Most of the created helium becomes mixed with the fission gas within these bubbles and subsequently follows the same release pathways. Thus, the release of helium to the rod free volume is observed to be proportional to the fission gas release and to exhibit the same initiation threshold.

For the experiments cited in Reference 8, the helium release (40%) from fuel was found to be five times greater than the fission gas release (8%). The approach taken for the current fuel pins is to assign a value of 0.50 as a first approximation to the helium release fraction. A 50% variance (release fractions from 0.25 to 0.75) then assures an adequate coverage of the possible range. As shown in Table 2.2 (Item e), the release range for created helium within Fuel Pin 7 is from 1.518E-5 to 4.555E-5 mole, with a central value of 3.037E-5 mole (one-half of the created amount). A similar approach is taken for Fuel Pin 16, as indicated by Item e of Table 2.3.

2.3.5 Total Fuel Pin Free Volume Gas Inventory

With the assumption that other gases are limited to trace (negligible) quantities, the total gas inventory within each fuel pin can now be calculated. For Fuel Pin 7, Table 2.2 (Item c) shows that the free volume contained 34.34E-5 mole of fission gas. Adding 4.046E-5 mole of initially loaded helium (Item d) plus 3.037E-5 mole of created helium released from the fuel matrix (Item e), the total free volume gas inventory is 41.42E-5 mole (Item f). As indicated, the associated range for this total inventory is estimated as 36.98E-5 to 45.88E-5 mole.

For Fuel Pin 16, the fuel pin gas inventory is somewhat larger, as indicated in Table 2.3 (Item f). Here the range is 41.52E-5 to 51.33E-5 mole, with a central value of 46.42E-5 mole.

2.3.6 Measured and Expected Fuel Pin Pressures

As discussed previously, the fuel pin gas pressures were obtained via application of the Fission Gas Pressure Measuring Apparatus described in Reference 1. Fuel pin pressures (before puncturing) were determined to have been 114.8 psia for Fuel Pin 7 and 134.8 psia for Fuel Pin 16, both at a gas temperature of about 95°F (308.2 K). This temperature and the fuel pin free volumes are utilized with the perfect gas law to calculate the expected gas pressures corresponding to the free volume gas contents (moles fission gas and helium).

Tables 2.2 and 2.3, items f through h, list, respectively, the parameters for the perfect gas law calculations for Fuel Pins 7 and 16. Results (Item i in both tables) are 116.1 psia for Fuel Pin 7

and 128.1 psia for Fuel Pin 16. The following Section provides an assessment of these expected pressures and the extent to which they agree with the measurement-derived values.

2.4 Assessment: Fission Gas Release Fraction Determination and Check

Gas release fractions are determined by measurement of Krypton-85 activity at the time when each fuel pin is punctured. A check is provided by simultaneous measurement of total gas pressure, which can be compared with the expected pressure based on the gas release fraction as derived from Kr-85 activity. The values listed in Tables 2.2 and 2.3 reflect a satisfactory check. However, when first applied, the measured pressure was higher than expected (based on Kr-85 activity) for the 40-GWd/MT fuel pins. (The gas release fractions for Fuel Pins 7 and 16 are about three times larger than those for previous withdrawals because of the very high LHGRs experienced during the second irradiation phase.)

In view of the discrepancy in the initial 40-GWd/MT fuel pin pressure check, the methods by which fission gas release fractions and total pin pressures are calculated, including the data inputs for these methods, were carefully scrutinized. As a result, several corrections were applied, three of which affected the calculated results to a noticeable extent. The following Section reviews for the record the corrections that were applied in obtaining the final values as presented in Tables 2.2 and 2.3.

2.4.1 Three Corrections to Release Fraction Determination and Check

First, it was decided that both the Kr-85 activity and the amount of fission gases generated during irradiation should be adjusted by the ratio [actual fuel mass/nominal fuel mass used in ORIGEN calculation]. For the capsules withdrawn to date, this ratio lies in the range 0.933–0.953, so that the amount of gas (and activity) available for release was decreased relative to the ORIGEN-predicted amount. Since the measured activity remains the same, the effect was to increase the calculated gas release fraction by 5 to 7%. The same amount of gas is released, so there was no change to the expected pressure.

The second correction affected only the measured gas pressure. Careful examination of the calibration data for the MOX Fission Gas Pressure Measuring Apparatus (Reference 1) revealed a small bias that requires an added adjustment factor (magnitude inversely proportional to pressure) for measured values in the 0–1000 psia range. Application of this bias removal factor served to reduce the measured pressure values by 3%–4%.

The third correction affected the measured Kr-85 activity in the form of a calibration curve for Kr-85 detection efficiency. This curve was developed by means of a series of checks designed to assess not only the accuracy of detector calibration but also the efficiency of the physical process of collecting all of the Kr-85 entering the system by freezing on cold traps. The contents (10, 30, 100, 1000, 3000, 4200, 5800, and 10,000 microcuries) of nine highly accurate Kr-85 calibration source containers purchased specifically for this purpose were collected in the detector cold traps and counted in the same manner as was the gas (about 4500 microcuries each for seven counting sessions) taken from each of the 40 GWd/MT MOX fuel pins.

The overall effort to calibrate detection efficiency is documented by letter report (Reference 10), including a basic description of the procedures by which the Kr-85 activity is measured for the irradiated MOX fuel pins. The detection efficiency was found to decrease as activity levels increase. Accordingly, application of the correction curve tends to increase the measured values at higher Kr-85 activity levels.

The effects of the three corrections may be summarized as follows: Consideration of the actual fuel mass increased the calculated fission gas release fraction but not the expected total pressure. Correction for the pressure measurement calibration bias lowered the measured pressure. Thus, the first two corrections slightly increased the calculated gas release fraction while slightly lowering the measured fuel pin pressure. Finally, application of the detection efficiency calibration curve decreased the measured Kr-85 activities for the 21- and 30-GWd/MT withdrawals but increased the measured activities (and associated calculated gas release fractions) for the 40-GWd/MT withdrawals.

With all corrections in place, the ranges for percent fission gas release and expected gas pressure based on Kr-85 activity measurements followed by the measured pressures are as listed in Tables 2.2 and 2.3 for the 40 GWd/MT withdrawals and summarized in Table 2.4 for all three capsule withdrawals to date. The width of each range is to a large extent established by the uncertainty (25%–75%) in the release of created helium.

Table 2.4. Fission Gas Release Ranges with Comparison of Expected and Measured Fuel Pin Pressures

Withdrawal	Gas Release Range Percent	Expected Pressure Ranges Psia	Measured Pressures Psia
21-GWd/MT			
Capsule 2 Fuel Pin 5:	1.21–1.43	18.17–24.54	20.25
Capsule 9 Fuel Pin 12:	1.73–2.03	21.03–28.15	23.61
30 GWd/MT			
Capsule 3 Fuel Pin 6:	1.36–1.59	23.85–33.70	26.71
Capsule 10 Fuel Pin 13	2.12–2.49	30.01–41.66	33.21
40 GWd/MT			
Capsule 4 Fuel Pin 7:	7.70–9.04	99.64–133.7	114.8
Capsule 13 Fuel Pin 16:	8.75–10.3	109.6–148.1	134.8

There is good overlap between the expected pressure ranges and the measured pressures for all three withdrawals. While the applied corrections have altered the specific values somewhat, the general conclusions remain the same. The fission gas releases calculated for the TIGR-treated fuel (Pins 12, 13, 16) are higher in every case. All calculated releases are lower than would be expected based on the European results for fuel irradiated at similar LHGRs.

The gas release fractions are larger for the 40-GWd/MT withdrawals because of the very high LHGRs experienced by these capsules during the second irradiation phase. It may also be noted that whereas the measured pressures fall below the middle of the expected ranges for the two earlier withdrawals, they are at or above this midpoint for the 40-GWd/MT withdrawals. This observation is discussed in the following Section.

2.4.2 Possible Cause for Increase of Measured Pressures Relative to Kr-85-Based Expected Pressure Ranges

The measured pressures fall higher within the expected ranges for the 40 GWd/MT withdrawals. Actual pressures would trend higher relative to the expected pressure ranges in successive PIEs if the helium release fraction were increasing with burnup, or if there were a burnup-dependent introduction of another gas, in addition to the fission gas and helium currently counted in the pressure calculation. Each fission frees two atoms of oxygen and hence, oxygen is a potential candidate for such a third gas in this conjecture.

A proportion of the oxygen released by fission of heavy metal oxides is bound to fission products. Reference 11 explains that this proportion is lower for plutonium fission. Most of the remaining oxygen is consumed by raising the oxidation potential of UO_2; however, Reference 12 describes a finding of lower-than-expected oxygen potentials in irradiated UO_2. A small portion enables the oxidation of the inner cladding surface, but Section 5.5 of Reference 13 reports that clad internal oxide layers are never found for burnups below about 25 GWd/MT. Reference 14 discusses the oxygen flux from pellet to cladding. The primary path for such transfer is by solid-state diffusion within regions where the pellet surface is in contact with the clad during irradiation. Nevertheless, the presence of thin uniform corrosion (ZrO_2) films over large portions of the cladding inner surfaces in the current fuel pins suggests that some oxygen may have existed, at least temporarily, as a constituent gas in the pellet-clad gap.

The amount of oxygen liberated increases with the accumulation of heavy metal oxide fissions. If the partial pressure of oxygen in the pin free volume increases with burnup, then the measured pin pressure would increase more than the measured Kr-85 activity in successive PIEs, i.e., with burnup.

Based upon literature review and the current observations of ZrO_2 films at the Fuel Pin 7 and 16 cladding inner surfaces, it seems plausible that very small fractions of the oxygen released by fission were present in the fuel pin free volumes during and after irradiation. A noticeable increase in fuel pin pressure can be produced by a very small fraction of the oxygen freed by fission. As an example, for the Fuel Pin 7 burnup of 39.9 GWd/MT, there were 7.51E21 fissions with 12.47E-3 gram-moles O_2 freed. A partial pressure of 5 psi would be produced if 1.78E-5 gram-moles or just 0.14% of this freed oxygen were present as a gas constituent in the fuel pin free volume. Such a presence would not be indicative of any fuel behavior anomaly. As discussed in Chapter 4, clad inner surface corrosion for these test fuel pins is no greater than expected from the European MOX database.

The thermodynamics of the $(U,Pu)O_2$ system precludes the existence of free oxygen in contact with these compounds. Whether or not a small quantity of oxygen resides in the fuel pin free volume can be determined directly by application of mass spectrometry to the collected gases.

A capability for such analysis is being developed for use in the next PIE, which will be for a burnup of 50 GWd/MT and will be performed in the summer of 2004. The primary purpose of this is to permit direct measurement of the fission gas inventories, but it will also settle the question as to whether or not there is sufficient oxygen in the fuel pin free volume to produce a noticeable partial pressure.

2.5 Fission Gas Release as Function of LHGR

Figure 2.1, which is adapted from Reference 15, displays literature values for fission gas release of European commercial test fuels plotted against the corresponding average linear heat generation rates (LHGRs) during the second irradiation cycle. This Figure also presents, in the upper left-hand corner, a bar chart illustrating the relative ranges for the axial powers (LHGRs) typically experienced during each of the irradiation cycles.

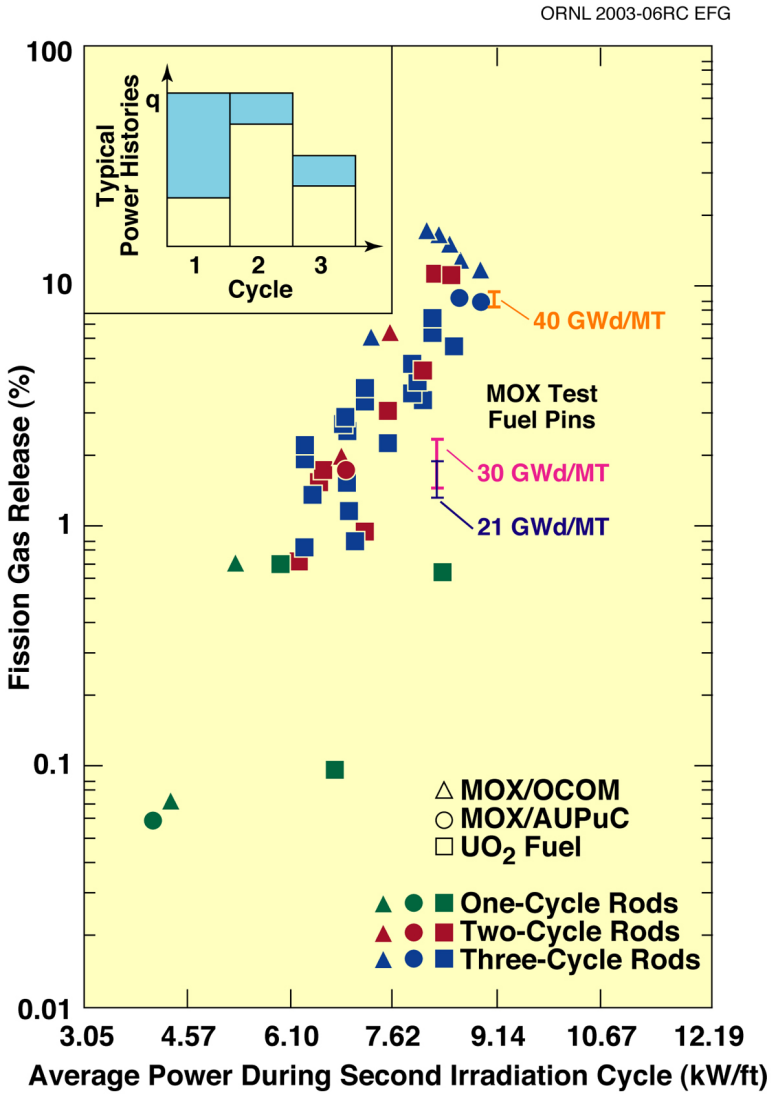

Fig. 2.1. The MOX test fuel pins exhibit gas release fractions proportional to their linear heat generation rate experience. (Basic plot is taken from Reference 15.)

The blue portions of the bar chart illustrate the extents of the LHGR variations for the first, second, and third irradiation cycles. In general, the LHGRs increase somewhat in proceeding from the first to the second cycle, and in all cases, decrease in proceeding from the second to the third cycle. It is important to recognize that the highest powers are experienced during the second irradiation cycle. This is why the average LHGR during the second irradiation cycle has been chosen as the abscissa parameter for the fission gas release plot. (The exception is those cases where the fuel was irradiated for just one cycle—in these cases, the fission gas release is plotted against the average LHGR during that single cycle.)

Since fuel temperatures are proportional to LHGRs, the points plotted in Figure 2.1 can also be considered to represent the linear relation (on a logarithmic scale) between the accumulated gas release at the end of the irradiation and the temperatures experienced by the fuel during the second cycle of the irradiation. This indicates that it is the highest temperature ever experienced by the fuel (which occurs during the second irradiation cycle) that primarily determines the fission gas release fraction, not the extent of the accumulated burnup. (The gas available for release does, of course, increase directly in proportion to burnup.)

Superimposed on the plot of Figure 2.1 are the implied fission gas release fractions (Table 2.1) as obtained by the Krypton-85 activity measurements for the intermediate (21 GWd/MT), 30 GWd/MT, and 40 GWd/MT withdrawals of the current MOX irradiation test. The abscissa values for these release fractions are the average LHGRs during Phase II of the MOX test irradiation.

All four “MOX Test Fuel Pins” of the 21 GWd/MT and 30 GWd/MT withdrawals were symmetrically located within the test assembly and hence had similar irradiation histories. Capsule-average LHGRs increased from 7.98 kW/ft for Phase I to 8.21 kW/ft for Phase II and then (30 GWd/MT Withdrawal Fuel Pins 6 and 13 only) fell to 5.48 kW/ft for Phase III. The highest LHGR experienced was 9.7 kW/ft at the beginning of Phase II.

Fuel Pins 7 and 16 withdrawn at 40 GWd/MT experienced higher LHGRs during their irradiation and hence exhibit a higher fission gas release fraction. These two pins were symmetrically located within the test assembly and hence share similar irradiation histories, which are described in detail in Chapter 3 of Volume 1. Capsule-average LHGRs increased from 5.88 kW/ft during Phase I to 9.05 kW/ft during Phase II (end burnup 20.1 GWd/MT). Subsequently, the average LHGR fell to 5.70 kW/ft (burnup range 20.1 to 29.0 GWd/MT) and further to 5.20 kW/ft (29.0 to 39.9 GWd/MT).

Because power (temperature) steps at higher burnups affect fission gas release, it should be noted that Fuel Pins 7 and 16 experienced a step increase in LHGRs during the two ATR irradiation cycles immediately prior to their withdrawal. This power boost (intentional) was gained by relocating the test assembly from the Northwest to the Southwest I-hole in the ATR reflector. As indicated in Table 3.4 of Volume 1, the average LHGR for these two capsules was increased from about 4.5 kW/ft during ATR Cycles 125B and 126A to about 6.4 kW/ft during Cycle 126B (burnup 35.4 to 37.7 GWd/MT) followed by 5.6 kW/ft during Cycle 127A (37.7 to 39.9 GWd/MT).

It is clear from Figure 2.1 that the fission gas release fractions obtained for the current test are low in comparison to the literature values (European experience) for the same LHGR history. For the MOX test fuel pins, the gas release fraction changed little for the 30 GWd/MT as opposed to the 21-GWd/MT withdrawals, since the highest LHGRs were similar for these two sets of fuel pins. The gas release fraction is significantly higher for the fuel pins withdrawn at 40 GWd/MT, but this is attributed not to the increase in burnup, but rather to the higher LHGRs (and fuel temperatures) experienced by these pins.

2.6 Halden Empirical Threshold

Several researchers have reported that the Halden empirical threshold for exceeding one percent fission gas release (described in Reference 16) applies to MOX fuel as well as to the UO_2 fuel for which this criterion was originally developed. Current fuels program publications often cite conformance with the Halden criterion as evidence that the fuel under study is performing in accordance with expectations.

In its original (and simplest) form, the Halden threshold is the burnup BU (GWd/MTHM) curve defined by the relation

$$BU = 0.00567e^{9800/Tc}$$

where T_c is the highest pellet centerline temperature (°C) ever experienced by the fuel. As an example, for burnups of 10.65 GWd/MT (or greater), fission gas release in excess of one percent is expected if the pellet centerline temperature exceeds 1300°C.

In its original form, the Halden threshold curve was constructed from available data extending to about 22 GWd/MT. It has subsequently been found that the portion of this curve extrapolated to higher burnups should be lowered. Recent data from Halden (Reference 17) have been employed to update the representation of this threshold for comparison with the fuel centerline temperatures as calculated for the current MOX test by the experiment-specific CARTS code. These comparisons are presented in Section 7.3, where it is shown that the Fuel Pin 7 and 16 centerline temperatures significantly exceeded the Halden threshold during most of irradiation Phase II and again during the last two ATR cycles prior withdrawal.

That the fuel centerline temperatures have exceeded the Halden threshold does not provide any quantitative information as to the extent of gas release (beyond one percent) to be expected. Nevertheless, given the degree to which the threshold was exceeded for Fuel Pins 7 and 16, and that the threshold was exceeded a second time at high (>35 GWd/MT) burnup, the observance of gas release fractions as high as eight and nine percent is not surprising.

2.7 Discussion and Conclusions

Fission gas release fractions are estimated within a reasonable uncertainty (±8%) for the MOX test fuel pins by measurement of the Krypton-85 activity in the gas collected from the fuel pin free volume. The fission gas release fractions as determined for the six MOX fuel pins withdrawn (two each) at burnups of 21, 30, and 40 GWd/MT are listed in Table 2.1. As

indicated, the values for the Intermediate (21 GWd/MT) and 30 GWd/MT withdrawals range from 0.0132 to 0.0230. These four fuel pins occupied symmetric positions with respect to the ATR core during the irradiation and have similar temperature histories through the end of Phase II, when the highest LHGRs (average 8.2 kW/ft; 9.7 kW/ft maximum) were imposed. Hence, it is not surprising that the fission gas release fractions for these four pins should fall within as narrow a range as 1.32 to 2.30 percent.

The fission gas release fractions for the two fuel pins withdrawn at 40 GWd/MT are four to five times larger. This is attributed to the significantly higher LHGRs (and fuel temperatures) that these pins encountered. Here the average LHGRs during Phase II were about 9.1 KW/ft with a maximum of about 10.7 kW/ft. Fuel Pins 7 and 16 occupied symmetric positions within the test assembly throughout their irradiation and have fission gas release fractions of 8.4% and 9.5%, respectively. While the Fuel Pin 16 LHGRs (as listed in Tables 3.1–3.5 of Volume 1) are slightly higher during much of the irradiation, other factors probably contribute to this pin's higher gas release.

With respect to Table 2.1, it should be noted that Fuel Pins 12, 13, and 16 each have higher fission gas release fractions than their symmetrically-placed pair Pins 5, 6, and 7. The PuO_2 powder for Fuel Pins 12, 13, and 16 was subjected to the Thermally Induced Gallium Removal (TIGR) process (Reference 18), so that most of the gallium was removed before pellet sintering. The average gallium content of fuel in these pins is about 1.3 PPM. (Gallium measurements for the unirradiated pellets are discussed in Reference 19.) Fuel Pins 5, 6, and 7 were prepared with untreated PuO_2 powder, so most of the gallium was driven off during pellet sintering, leaving an average MOX gallium content of about 3.0 PPM.

While carrying out its primary purpose of gallium removal, the TIGR process also affects the powder (and pellet) morphology. As discussed in Reference 18, TIGR treatment at the temperatures (about 1200°C) for which it is effective tends to increase the particle size while greatly reducing the specific powder surface area. It is certainly plausible that these pre-sintering changes in particle characteristics are contributing to the observed differences in fission gas releases between the TIGR-treated and the untreated MOX fuels.

The fission gas partial pressure is determined by use of the perfect gas law with the fuel pin free volume, the fission gas release fraction from the Kr-85 activity measurements, and the ORIGEN code prediction of the amount of fission gas created within the fuel. The expected fuel pin total pressure can then be estimated as the sum of the partial pressures of fission gas and helium. The expected pressure is inherently uncertain, however, because it is not known how much of the created helium (from decay of transuranics) has escaped from the fuel matrix and is thereby contributing. The available literature is limited with respect to the extent of helium release from fuel. There is some evidence, however, that 40% to 60% of the helium is released into low-pressure pins. (In general, helium release is not an important consideration for commercial PWR fuel, because the large backpressure associated with the initial helium charge tends to keep the created helium within the fuel matrix.)

With the amount of created helium that has escaped from the fuel not known, the uncertainty bounds for the current MOX test are set by first assuming that one-fourth escapes (lower bound for expected pressure) and then assuming that three-fourths escapes (upper bound for expected

pressure). Since the created helium at 40 GWd/MT is about 1.5 times the amount initially loaded for this test, these choices introduce an undesirably wide range (uncertainty) for the calculated helium partial pressure. Nevertheless, the fission gas contribution to the total pressure is much larger, so a meaningful check on the extent of fission gas release is obtained when the measured fuel pin pressures fall within the uncertainty range of the expected pressures. As indicated in Table 2.4, this is the case for all three withdrawals for which fission gas release has been evaluated.

Although greater than one percent, the fission gas releases for these weapons-derived MOX test fuel pins are low in comparison to the European experience for mixed-oxide fuel with similar irradiation histories. Until about ten years ago, it was common practice to plot measured fission gas release fractions against the final burnups of the associated fuels. In general, this approach is characterized by wide scatter in the plotted points. Beginning in about 1993 (Reference 15), it has become generally recognized that the fission gas release fraction has a much stronger dependence on the maximum temperature experienced by the fuel than on the accumulated burnup. When fission gas release fractions are plotted against the highest LHGR experienced by the fuel, a linear relation is displayed, as in Figure 2.1. (The variation in values, particularly at higher LHGRs is still quite large. This reflects factors such as differences in fuel microstructure, gap size, and extent of cracking, as well as use of average power as the independent parameter.)

Good discussions of the mechanisms for fission gas release in MOX fuel are provided in References 7, 15, 20, and 21. Only a small portion of the fission gas generated during irradiation (corresponding to the solubility limit) is retained in the fuel matrix. Most fission gas accumulates in the pores of the plutonium-rich agglomerates or intragranularly in adjacent grains, and release to the fuel pin free volume requires the development of a system of escape tunnels along the grain boundaries in the surrounding UO_2 matrix. High temperatures cause these tunnels to open, and the extent of the associated escape pathways depends on the highest local temperature that has been experienced. Subsequent temperature reductions have limited effect in closing these tunnels by grain boundary sintering.

Reference 15 is the source of the European fission gas release experience as displayed in Figure 2.1, against which the measured fission gas release fractions for the current test fuel are compared. Recognizing that the test fuel pin design, although similar, is not identical to the European design, it is fair to question whether the European fission gas release versus fuel power history experience shown in Figure 2.1 is a valid standard for comparison with the weapons-derived MOX test fuel measurements. As discussed previously, the fission gas release fraction is representative of the highest temperature that the fuel has attained, and the proportionality between fuel temperature and LHGR is design-dependent with strong contributions from the clad external surface temperature and the width of the pellet-cladding gap. Accordingly, Dr. Wolfgang Goll (Reference 15 author) has considered the temperatures experienced by the weapons-derived MOX test fuel and the use of Figure 2.1, and with respect to his European data, has concluded that the associated fission gas measurements are “largely comparable to our data base.”

Also pertinent to the current test MOX fuel is the discussion provided by Reference 20 concerning the effects of agglomerate distribution on fission gas release fractions. Tests

employing two different agglomerate volume fraction / plutonium concentration combinations irradiated under the same conditions found no significant differences in fission gas release. Almost all of the fission gas is released from the fuel lattice, but as explained in Reference 21, most is then retained either in the pores of the high-burnup structure within the agglomerates or in very small cavities within the UO_2 grains that abut the outer surfaces of the agglomerates. (The agglomerates and their surrounding fission gas "halos" are discussed in Chapter 3.)

Given that the measured fission gas release fractions exceed one percent, it is of interest to compare the irradiation experience of the current test fuel pins with the Halden criterion to check whether or not this is an expected result. The Halden Threshold, dating from 1979 and recently modified (lowered) for burnups greater than 22 GWd/MT, is an experimentally-derived curve of pellet centerline temperature versus burnup. If a superimposed trace of actual pellet centerline temperatures rises above this reference curve, then fission gas fractions greater than one percent are to be expected.

In making comparison to the Halden Threshold, it is important to recognize that the gas release fractions listed in Table 2.1 are averages for the fifteen pellets held within each fuel pin. Each initial pellet-to-clad gap can lie anywhere within the range afforded by the pellet and cladding fabrication tolerances, and the width of each gap affects the effective thermal conductance between pellet and cladding. Therefore, it is expected that the individual pellets have, for the same LHGR, different traces of calculated centerline temperatures.

The pellet centerline temperature traces for the 40 GWd/MT withdrawal fuel pins are shown in Chapter 7. The range is defined by bounding calculations based on the minimum and the maximum initial pellet-clad gaps. Gas releases of greater than one percent are indicated for both pins in all cases. It is of interest to note that the Halden Threshold is exceeded twice, first during nearly all of irradiation Phase II and later at burnups over 35 GWd/MT, just before withdrawal for PIE.

Finally, it is important to recall that the mission fuel for the Fissile Materials Disposition Program will be improved relative to that employed in the test fuel pins discussed here. Use of modern fuel fabrication techniques will increase the PuO_2 homogenization within the mission fuel and reduce agglomerate size. Design and operational provisions will tend to reduce fission gas release fractions. The improved heat transfer afforded by clad creep down (instead of outward clad movement) will serve to reduce the pellet temperatures at comparable linear heat generation rates. Further, the power levels during mission fuel lifetime will be lower than those experienced by the weapons-derived MOX fuel irradiated in the current test.

3. CHARACTERISTICS OF THE PLUTONIUM-RICH AGGLOMERATES

3.1 Introduction

This Chapter addresses the plutonium-rich agglomerates in the test MOX fuel as observed for Fuel Pins 7 and 16 (Capsules 4 and 13). Both of these fuel pins had been irradiated to approximately 40 GWd/MTHM at the time of withdrawal for PIE.

Following a brief discussion of MOX fuel fabrication processes in general, Section 3.2 describes the structure of the weapons-derived fuel being irradiated in the current test. The rationales for placing limits on mixed-oxide agglomerate size as found in the literature are discussed in Sections 3.3 (reprocessing) and 3.4 (reactivity insertion accidents). Examples of initial agglomerate size specifications proposed for application to mixed-oxide fuels for U.S. reactors (including the current test irradiation) are provided in Section 3.5.

The manner in which the structure of the plutonium-rich agglomerates changes with burnup is discussed in Section 3.6. The effects of agglomerate restructuring upon fission gas retention are discussed in Section 3.7. Section 3.8 summarizes the agglomerate distributions and size as observed in the current PIE. Finally, Section 3.9 provides a synopsis of the main points and the conclusions of this Chapter.

3.2 Structure of the MOX Test Fuel

The earliest method for production of mixed-oxide (MOX) fuel was to obtain the desired fissile plutonium concentration by directly comilling the PuO_2 and UO_2 powders. The resulting fuel is heterogeneous, with the PuO_2 particles everywhere completely distinct from the UO_2. This "reference" process was used until about 1985, when it was generally abandoned due to inadequate solubility in nitric acid and the undesirable impact of this characteristic upon fuel reprocessing.

Several methods to improve the homogeneity of MOX fuels have been developed over the last two decades, including the Short Binderless Route (SBR) in England, the Optimized Co-Milling (OCOM) in Germany, and the MIcronized MASter blend (MIMAS) process in Belgium and France. The mixed-oxide fuel being irradiated in the current test was prepared at Los Alamos National Laboratory (LANL) in a manner similar to the MIMAS process.

As explained in Reference 22, the MIMAS process is predicated on use of a master mix comprising all of the PuO_2 and a fraction of the UO_2. These two powders are simultaneously milled for several hours to produce an intimate mixing. The milling also modifies the physical characteristics of these powders. The comminution causes self-agglomeration due to electrostatic forces, thereby producing agglomerates which, while rich in plutonium, are not pure PuO_2. After sieving, the master mix is blended with the remainder of the UO_2 to form the secondary blend, from which the pellets are pressed.

It is important to recognize that only a portion of the UO_2 (that in the master mix) undergoes milling in MIMAS. The physical characteristics (especially flowability) of the UO_2 powder introduced to surround the PuO_2–rich agglomerates in the secondary blend are not altered by milling. Thus, a free-flowing press feed for automated die fill is achieved without precompaction or granulation of the mixed oxide powders.

The MOX fuel for this test irradiation was fabricated at LANL during 1997. The weapons-derived PuO_2 powder feedstock was obtained from Lawrence Livermore National Laboratory (LLNL). The baseline dry pyroprocess used at LLNL to convert the weapons components into the feed oxide powder was the three-step HYDOX, developed by the ARIES project. At Los Alamos, half of the PuO_2 feed was subjected to the Thermally Induced Gallium Removal (TIGR) treatment as described in Reference 18. The two PuO_2 powders (TIGR-treated and untreated) were then milled with UO_2 to form two separate master mixes. Each master mix was then blended (mixed, not milled) into pure UO_2 powder to form two secondary blends, from which the two sets of pellets were pressed.

Both mixed-oxide test fuels consist of five percent PuO_2 and 95% depleted UO_2, the latter converted by the ammonium diuranate (ADU) process. In each case, all of the PuO_2 was introduced as 31% of the master mix. Stated another way to give a better feel for the numbers, included with each 100 grams of the test MOX fuel are five grams of PuO_2 and 11.11 grams of UO_2 that were milled together to form the master mix. This milling reduced the PuO_2 and UO_2 particle size while promoting a homogeneous dispersion of the PuO_2 particles in the UO_2. Employing a mixer/blender that does not alter particle characteristics (as does milling), these 16.11 grams of master mix were then diluted and dispersed into the remaining 83.89 grams of depleted UO_2.

The plutonium-rich agglomerates are in essence clumps of master-mix. The secondary blending (dilution) process that distributed these agglomerates into the matrix of depleted UO_2 is incomplete, in the sense that residual particles (agglomerates) of the master mix remain intact with equivalent diameters ranging from very small to 200 microns or more within the final blend. Some degree of incompleteness is desirable, in order to maintain the flowability of the UO_2 by limiting the energy input to the powders. The plutonium concentration within the plutonium-rich agglomerates is higher than the MOX fuel average, but does not exceed that of the master mix, which is 31% for the current test fuel.

Irradiation of the test MOX fuel produces a heterogeneous fission distribution on a microscopic scale, with most fissions occurring within the agglomerates. The local burnup within the agglomerates is much higher than the average for the fuel, and the internal accumulation of fission products (solids and gas) causes the agglomerates to swell against the constraining matrix of UO_2.

As burnup increases, the plutonium concentration within the agglomerates decreases because of depletion by fission and a limited diffusion into the surrounding matrix. Simultaneously, the plutonium concentration increases within the UO_2 matrix due both to creation by neutron capture in the U^{238} nuclei and to a minor extent, diffusion from the agglomerates.

3.3 Rationale for Limiting the Size of Plutonium-Rich Agglomerates

The two reasons most often cited in the literature for limiting the size of the plutonium-rich agglomerates are to facilitate dissolution during reprocessing and to reduce any detrimental effects that large agglomerate size may have with respect to increasing the release of fission product gases. The first of these will be discussed very briefly, since facility of reprocessing (fuel solubility) is not among the goals of the FMDP mission.

Reference 15 reports with respect to Siemens fuel that

> "The irradiation experience of fuel assemblies with the MOX fuel, designated a 'former standard' … was excellent. However, this MOX fuel did not satisfy reprocessing requirements, such as complete solubility of plutonium in pure nitric acid (>99%). This led to the development of new MOX powder preparation processes: the ammonium uranyl plutonyl carbonate (AuPuC) and optimized co-milling (OCOM) processes, which yield pellets with better plutonium solubility in pure nitric acid …"

Similarly, Reference 22 (Chapter 5, Section 1.3.3) reports the French and Belgian experience:

> "Up to 1985, the 'reference' process used (BELGONUCLEAIRE process) consisted of a direct PuO_2–UO_2 blend by comixing which resulted in a heterogeneous fuel (100% local PuO_2) … Fuel elements of this type have reached 50 GWd/tU+Pu …, but this process was abandoned because of reprocessing problems (bad solubility).
>
> "The evolution of the 'reference' product led BELGONUCLEAIRE to the MIMAS process, which consists of the comilling of a mixture of PuO_2–UO_2 at 30% of maximum plutonium content, followed by a comixing of this first mixture with the UO_2 blend to obtain the nominal content …
>
> "MIMAS MOX always keeps a certain plutonium distribution heterogeneity, nevertheless it is much improved compared to the 'reference MOX' (agglomerates at 30% of maximum plutonium content, size < 100 μm)."

In summary, although there were no performance problems with the early simple fuel mixtures, steps were taken to introduce a master-mix and to limit the size of the resulting plutonium-rich agglomerates in order to improve the solubility of the irradiated fuel for reprocessing purposes.

The second rationale for limiting agglomerate size, based on the supposition that large agglomerates may tend to increase fission gas release, is more pertinent to the current MOX test irradiation. Nevertheless, there has been no precise quantification of such an increase in European fuel (Reference 23), and Reference 20 reports no significant difference in fission gas release for two different agglomerate volume fractions and plutonium concentrations irradiated under the same conditions, or for different radial locations within the fuel. As discussed in Chapter 2, although burnups have reached 40 GWd/MT and the agglomerates are large relative to those of modern European commercial fuel, there is no evidence of a detrimental effect upon gas release for the current test. Gas release will again be monitored when this test fuel reaches 50 GWd/MT.

3.4 Effect of Large Agglomerates in Reactivity Insertion Accidents (RIAs)

Transient power-burst tests to determine the effects of large pure PuO_2 microspheres were conducted in the SPERT reactor in 1969 and 1970. The following is taken from the "Summary and Conclusions" of the published results [Reference 24].

> "Transient tests were conducted on nonirradiated oxide pellet-containing thermal recycle fuel pins at SPERT to investigate the possible effects of large single 550-μm-diam PuO_2 particles, which could possibly be present in the fabricated fuel, on the transient behavior. The results are compared with the results of similar tests conducted on pins containing enriched UO_2 and UO_2–PuO_2 pellet fuel that did not contain abnormally large PuO_2 particles.
>
> "The results of these tests show that the effect of the large PuO_2 particles was to reduce slightly the cladding failure threshold energy … There were no indications of the effects of prompt fuel dispersal caused by the expulsion of the PuO_2 particles into the surrounding water when tested at these energy levels.
>
> "Because the presence of single 550-μm-diam PuO_2 particles in mixed-oxide fuels does not appear to affect significantly the cladding failure threshold energy from that of mixed-oxide fuels with the normal PuO_2 particle size and distribution, product specifications that limit the maximum PuO_2 particle size to 550-μm diam do not appear warranted from the standpoint of transient fuel performance considerations. Specifications should be developed which limit the maximum PuO_2 particle size. These experiments have shown that such a limit is >550-μm diam."

It is important to recognize that the dimensions discussed in the SPERT results pertain to discrete PuO_2 particles, not to the overall size of plutonium-rich agglomerates. The more recent experiment described by Reference 25 also addresses the effects of pure PuO_2 particles in RIAs. Here, seven MOX test rods were prepared with PuO_2 particles of either 400 or 1100 μm equivalent diameter artificially embedded at one pellet surface. These rods were then subjected to rapid power bursts in the Nuclear Safety Research Reactor in Japan.

As described in Reference 25, "A PuO_2 particle located on the surface of a pellet can affect the failure threshold because a local peak of cladding temperature due to the particle can lead to fuel failure at lower total energy disposition or the particle can act as a projectile moving at high velocity." What has not been established is the minimum particle size at which such effects occur. It is a conclusion of Reference 25 that "a PuO_2 particle up to 1100 μm on the surface of a pellet did not influence the failure behavior." It should be recognized that this is a much greater equivalent diameter than is found in the largest of the plutonium-rich agglomerates of mixed-oxide fuels.

3.5 Technical Specifications: Plutonium-Rich Agglomerates

Pellet Technical Specifications normally include provisions with respect to plutonium-rich particles or agglomerate size. This Section provides three examples of wording proposed for application to mixed-oxide fuel intended for irradiation in U.S. reactors.

3.5.1 American Society for Testing and Materials (ASTM)

The draft ASTM specification for mixed-oxide fuel (Reference 26) is crafted as follows:

> "No more than 5% of the plutonium-rich particles shall be greater than 100 μm in diameter. The average diameter of plutonium-rich particles will be less than 50 μm. The maximum equivalent diameter of plutonium-rich particles will be less than 400 μm."

It should be noted that this draft specification is intended for "finished sintered (uranium-plutonium) dioxide pellets for use in thermal reactors" and "applies to uranium-plutonium dioxide pellets containing plutonium additions up to 15% by weight."

3.5.2 Framatome Technologies

Reference 27 includes the "plutonium-rich particle size" specification for the Fissile Materials Disposition Program mission fuel as follows:

> "At least 95% of the plutonium-rich particles shall have an effective diameter of less than 100 μm. The mean plutonium rich particle distribution shall be less than 50 μm. No pure plutonium grain shall be greater than 400 μm."

It is of interest that this mission fuel specification invokes the important difference between plutonium-rich particles and pure plutonium grains. The plutonium content of the plutonium-rich particles in MIMAS-produced fuel is limited to that of the master mix or primary blend.

3.5.3 Technical Specifications for the MOX Test Irradiation

Provisions with respect to agglomerate size are included in the Technical Specification for the MOX test pellets (Reference 28). Section 4.10 "Microstructure," Subsection 4.10.2 "Homogeneity" provides that:

> "No more than 5% of the nominal PuO_2 content shall be present in PuO_2-rich (having a plutonium content greater than 150% of the nominal bulk composition) particles of diameter greater than 200 μm. … Area percent and volume percent should be considered equivalent …"

The "nominal PuO_2 content" for this test fuel is 5%, which, as explained in Section 3.2, is mixed with UO_2 to the extent that the resulting agglomerates constitute 16.11% of the total fuel mass.

In applying the specification, it is assumed that the milling is sufficient to ensure that the PuO_2 is evenly distributed among the agglomerates. Given that the volume fraction is approximately equal to the mass fraction, and with the guidance that "area percent and volume percent should be considered equivalent," this specification provides that PuO_2-rich agglomerates with equivalent diameters larger than 200 μm should occupy no more than 0.0081 (5% of 16.11%) of the unirradiated fuel cross-sectional area. A review of the raw data measurements taken at Los Alamos following fuel fabrication indicates that about five percent of the unirradiated fuel cross section was occupied by plutonium-rich agglomerates larger than 200 μm. Although this

exceeds the specification, it is not of concern since fuel reprocessing is not of interest to this experiment.

3.6 Agglomerate Growth and Restructuring During Irradiation

Most fissions occur within the plutonium-rich agglomerates, and although recoil and knockout processes cause a small portion of the fission products to migrate to the surrounding UO_2 matrix, most are retained within the agglomerates. Hence, these bodies swell as burnup increases due to the accumulation of both solid and gaseous fission products. An excellent discussion of the experimentally-observed agglomerate states at various locations across pellet cross-sections and at various stages of burnup is found in Reference 15.

When evaluating the extent of irradiation for a mixed-oxide fuel prepared with a MIMAS-type fabrication process, it is important to recognize that two additional burnups, besides the fuel-average burnup, are appropriately defined. These are the burnup within the plutonium-rich agglomerates and the much smaller burnup within the surrounding matrix of depleted uranium. For the current test fuel in the earliest stages of irradiation, it is reasonable to make the approximation that all of the fissions occur within the agglomerates and none within the surrounding depleted UO_2 matrix. As explained in Section 3.2, 16.11% (about one-sixth) of the total fuel mass resides within the agglomerates. Since burnup (GWd/MTHM) is the ratio of energy release to fuel mass, the burnup rate within the agglomerates is initially about six times that of the fuel average. At 2 GWd/MT for the mixed oxide, the burnup within the agglomerates is approximately 12 GWd/MT.

The ratio of agglomerate burnup to fuel-average burnup is reduced as irradiation proceeds due to the creation of fissionable isotopes (principally Pu-239) within the depleted uranium matrix. Calculations performed at INEEL (Reference 29) based on the current MOX test fuel provide estimates of the agglomerate and matrix burnups as functions of the local fuel average burnup. The agglomerates reach 60 GWd/MT when the average burnup is about 18.3 GWd/MT. At a predicted fuel average burnup of 40 GWd/MT, the associated burnups are 100 GWd/MT for the agglomerates and 28.4 for the UO_2 matrix. The extents of burnup differentials among the constituents of other MOX test fuels are discussed in References 15 and 20.

High burnup within the plutonium-rich agglomerates is accompanied by considerable local swelling induced by the accumulated solid and gaseous fission products. Whereas the solid fission products stay with an agglomerate throughout fuel life, the fate of the fission product gases depends upon the temperature during irradiation of the region in which the agglomerate is located. In this connection, it is important to recognize that the temperature of an agglomerate is only slightly higher than that of its immediate surrounding matrix, as explained in Reference 13.

Agglomerates become highly visible when they have transformed into a “high burnup structure.” This structure forms within fuel above a local irradiation threshold of about 60 GWd/MT, when the temperature is below about 1000°C (Reference 30—thermal restructuring and thermal fission gas release processes dominate at higher temperatures.) The high burnup structure is formed by a process of recrystallization that produces small (<1 micron) grains with many accompanying pores for storage of fission gas. For the MOX test irradiation intermediate (21 GWd/MT) and

subsequent withdrawals, the two conditions for formation of the high burnup structure (>60 GWd/MT at low temperature) exist within MOX agglomerates in the cooler outer regions of the fuel cross-section. It is their high-burnup structures that make the agglomerates in this region readily visible.

The overall volumetric swelling rate for fuel (MOX or UO_2) due to retention of fission product solids and individual gas atoms in the fuel lattice is about 0.7% per 10 GWd/MT. Applying this rate to a fuel-average burnup of 40 GWd/MT, the calculated swelling is approximately 2.8%. Local swelling within the agglomerates, where most of the fissions occur, is much higher. The agglomerate swelling is accommodated by plastic deformation of the surrounding UO_2 matrix, so that the net effect is a global swelling of the MOX fuel.

Gas storage within the pores of the agglomerate high-burnup structure adds to the effects of the fission product insertions into the fuel lattice, thereby inducing additional local swelling. Reference 15 reports bubble diameters as large as 4 μm for agglomerate burnups approaching 200 GWd/MT, with coalescence enabled as the increasing bubble diameters approached the initial separation distance between bubbles. Agglomerates in the outer portion of the test pellets (where the high-burnup structure evolved) were observed to swell by an additional 20 to 40% "due to the development of porosity within the agglomerates."

Reference 15 also reports observations with respect to agglomerates located at or very near the pellet surface, so that they are not completely surrounded by the restraining UO_2 matrix. With the "lack of compression to hinder swelling," these can grow out of the fuel surface. Such swelling agglomerates were observed (Reference 15) to have reached average heights of 6 to 8 μm above the pellet surface at fuel-average burnups above 20 GWd/MT.

3.7 Agglomerate High-Burnup Structure Effects Upon Fission Gas Retention

Most of the krypton and xenon generated in the 40 GWd/MT withdrawals was created by fissions occurring within the agglomerates. Within the fuel pellet, local temperature drives the local gas release because temperature "determines the diffusion of the fission gas to the grain boundaries with subsequent formation of release channels" (Reference 15). In the cooler outer regions of the pellet, much of the fission gas is retained in pores (large intragranular bubbles) within the high burnup structures of the agglomerates. In the pellet central region, where the agglomerates have not recrystallized, the higher temperatures cause most of the fission gas to exit the agglomerates via diffusion. In both regions, a significant portion of the fission gas transfers to the matrix grains surrounding the agglomerate, taking the form of very small intragranular bubbles occupying the nanometer-size cavities in the UO_2 matrix.

That there is room within the surrounding fuel matrix for such accumulations of fission gas atoms is discussed in Section 5.4 of Reference 21, which explains (based on measurements for irradiated UO_2)

> "*that the matrix contains a large population, $\approx 10^{24}$ m^{-3}, of small nanometre-size cavities. These quickly attain their final density and size, which appear to be largely independent*

of burnup. … These cavities grow by the capture of gas atoms and are destroyed by fission fragments which return the gases to solution; a steady-state morphology results."

For mixed oxide irradiation, the fission fragments chiefly originate within the agglomerates and hence tend to establish a directed radial migration of gas atoms farther into the surrounding grains of the UO_2 matrix.

3.8 PIE Observations: Agglomerate Structure, Size, and Surrounding "Halos"

Agglomerates that have transformed to the high-burnup structure can be easily discerned in irradiated fuel displayed in metallographic mounts. Such agglomerates have been evident for the PIEs conducted for the 21-, 30-, and 40-GWd/MT withdrawals. Observations from these PIEs with respect to agglomerate distribution and size are discussed in Section 3.8.1. Observations with respect to fission gas distribution are discussed in Section 3.8.2.

3.8.1 Agglomerate Structure and Size

The PIE conducted for Capsule 2 (Fuel Pin 5) and Capsule 9 (Fuel Pin 12) is documented in Chapter 5 of Reference 31. Four metallographic mounts were prepared representing the fuel cross-sections for Pellets 1 and 14, near the top and bottom of both fuel pins. At this approximately 21-GWd/MT average fuel burnup, agglomerate high-burnup structures were clearly visible as light gray patches, irregularly dispersed in the outer half of the pellet cross-section.

Each mount included 6 to 9 visible agglomerates with equivalent diameters in excess of 200 μm, the largest being about 420 μm. One mount exhibited an agglomerate at the pellet surface, which had apparently bonded during irradiation with the inner surface of the cladding. A separate (fifth) mount was prepared for Scanning Electron Microscope (SEM) and Electron Probe Micro Analyzer (EPMA) examination. Scanning over one of the agglomerates visible at pellet mid-radius and its surrounding UO_2 matrix confirmed the expected high degree to which plutonium is concentrated in the agglomerates.

Reference 32 documents the PIE of the 30-GWd/MT Capsules 3 and 10 (Fuel Pins 6 and 13). As discussed in Chapter 5 "Metallography," four metallographic mounts were prepared at fuel cross-sections taken from Pellets 1 and 15 in both fuel pins. The visible agglomerates were distinguished by the light gray patch shapes that outline their high-burnup structure, including the large internal pores in which their fission gases are concentrated. Similar to the earlier PIE, these (visible) agglomerates were irregularly dispersed over the portion of the pellet cross-section about one-quarter-radius inward from the pellet rim.

The largest of the agglomerates at 30 GWd/MT had an equivalent diameter of about 600 μm, some 50% larger than the maximum seen at 21 GWd/MT. Some sporadic bonding was evident between agglomerates at the pellet surface and the adjacent cladding.

There was virtually no evidence of high-burnup structure in the central (highest temperature) regions of the fuel cross-sections. Stated another way, the plutonium-rich agglomerates in the

fuel inner regions were not visible due to the absence of transformed grains and local gas-filled pores.

The PIE of the 40-GWd/MT Capsules 4 and 13 (Fuel Pins 7 and 16) is documented in the Volume 1 companion to this report, including discussion of the visible plutonium-rich agglomerates in Chapter 5 "Metallography." For Fuel Pin 7, four metallographic mounts represent fuel cross sections at Pellet 2 (upper end), Pellet 10 (upper end and middle), and Pellet 15 (upper end). Three mounts were taken from Fuel Pin 16—at Pellet 1 (lower end), Pellet 2 (upper end), and Pellet 15 (upper end).

The mounts containing fuel and surrounding cladding from the vicinity of the upper end of Pellet 2 in both fuel pins were examined by SEM and EPMA. The fuel held in these mounts must be very thin to reduce the dose rate. Because the TIGR-treated fuel from Fuel Pin 16 is more friable than the Pin 7 fuel, a thicker mount was used. Both mount surfaces were of excellent quality (very little pullout).

As in the previous PIEs, agglomerates in the outer regions of the fuel surfaces are clearly visible due to their recrystallization to a high-burnup structure. Areas of particular interest in all mounts were the "halos" (fission gas storage regions) surrounding the large agglomerates within the pellet (discussed in Section 3.8.2), the absence of high-burnup structure within the depleted UO_2 matrix at the pellet rim, and the nature of the corrosion layers intermittently located along the pellet-clad interface (discussed in Chapter 4). Also, first observed in this PIE are the beginnings of high-burnup structure transformation in the agglomerates located in the central pellet region.

As discussed previously, a high burnup structure (small grains with a few large pores) evolves during irradiation when the local temperature is less than 1000°C and the local burnup exceeds about 60 GWd/MT. Within the depleted UO_2 matrix, local burnup is highest near the pellet edge; nevertheless, no such recrystallization is found around the pellet circumference. Given that low temperatures did prevail in the rim area throughout the irradiation, the lack of high-burnup structure indicates that the depleted UO_2 in this region has not achieved local burnups of 60 GWd/MT (or higher). This is comparable with the European MOX experience, for which it is reported (Reference 13) that the microstructure of the UO_2 matrix at the rim "may just have begun to transform" at a fuel-average burnup of 44.5 GWd/MT.

On the other hand, burnups within the agglomerates in the central pellet region are much higher than 60 GWd/MT, but temperatures in this region were too high to permit recrystallization until local LHGRs declined as the plutonium in these agglomerates was consumed. The onset of recrystallization as temperatures lowered has produced the faint agglomerate outlines visible in the central pellet region fuel mounts of the 40 GWd/MT PIE.

3.8.2 Surrounding "Halos"

As discussed in Section 3.7, much of the fission gas generated within the agglomerates transforms to and is retained within the grains of the surrounding UO_2 matrix. This effect is explained in Reference 21, which describes detailed electron probe microanalysis (EPMA) studies of the microstructure and microchemistry of irradiated MOX fuel. These studies revealed the collection of an "encircling annulus of intragranular bubbles" of fission gas around the

"Pu-rich spots" (agglomerates). These surrounding bubbles are located in very small cavities within the UO_2 grains that abut the outer surfaces of the agglomerates. For our 40 GWd/MT withdrawal fuel, these fission gas annuli produce an optical effect, taking the form of "halos" visible around the agglomerates in the cross-section photographs.

Agglomerates of widely varying sizes all display the halo, a clear region distinct from both the fuel matrix and the high-burnup structure. These regions are visible because athermal (fission recoil) diffusion of fission products such as xenon from the agglomerate has altered the adjacent matrix in a manner that responds differently to polishing. Each halo comprises a swarm of very small gas bubbles within the adjoining UO_2 matrix grains. The presence of xenon in these regions has been confirmed by EPMA measurements in the current PIE (as discussed in Section 5.6 of Volume 1).

Halo thickness is on the order of a few fission fragment recoil distances (10–50 microns). The amount of gas generated is proportional to agglomerate volume, rendering it reasonable that the halos are, apparently, of nearly uniform thickness with volumes proportional to the agglomerate surface area. The halos are in effect gas storage sites that collect the athermal diffusion from the agglomerates. The gas within the halo regions is eligible for eventual release to the pin free volume by absorption/ejection from cavity to cavity until the process of random diffusion carries the individual atoms to a grain boundary and into a relatively large intergranular bubble.

3.9 Discussion and Conclusions

The mixed-oxide fuel currently fabricated for commercial purposes in European reactors by master-mix processes such as MIMAS and OCOM typically contains about 5 weight percent plutonium and comprises master-mix particles (plutonium-rich agglomerates) up to 200 μm in equivalent diameter, irregularly dispersed in a UO_2 matrix (Reference 20). The microstructure produced by the master-mix process differs from the dual structure of a simple (pure PuO_2 particles embedded in a UO_2 matrix) mixture because the initial master mix, prepared by milling a 30%–70% UO_2 powder combination, is diluted into a much larger (fivefold by mass) UO_2 matrix. Thus, the structure is more homogeneous since the plutonium content of the agglomerates is no more than 30%. When irradiated, this mixed-oxide fuel develops both high-burnup (agglomerates) and low-burnup (UO_2 matrix) regions.

The microstructure is also influenced by the characteristics of the UO_2 powder, which determines both the porosity distribution and the master mix distribution in the matrix (Reference 33). Pore size and distribution are affected in MIMAS by a proprietary pore-forming additive. The MOX test fuel being irradiated in the ATR was fabricated with a MIMAS-type approach, in that a master mix was prepared and then diluted into a secondary blend. However, there are important differences (Reference 34). The depleted UO_2 was not of the free-flowing kind employed in the MIMAS process, the pore-forming additive was not employed, the mill and mixer were not the same, and the master blend was not sieved. Milling and mixing parameters were not the same as normally used with MIMAS since these were not known at LANL at the time the test fuel was

made.* Because of these differences, the MOX fuel prepared for this test irradiation project should not be considered as MIMAS mixed oxide, but rather as a test fuel fabricated with weapons-derived plutonium utilizing a MIMAS-type approach.

The MOX test fuel comprises 5 percent PuO_2 derived from a weapons component and 95% depleted UO_2 (CAMECO powder) converted via the ammonium diuranate (ADU) process. The secondary blending was not as effective as desired in dispersing the master mix into the UO_2 matrix, so that relatively large residual agglomerates of the master mix are evident in the final fuel. The Pellet Processing Data packages prepared at Los Alamos subsequent to the test fuel fabrication indicate an average measured area fraction of about 1.5% for plutonium-rich agglomerate equivalent diameters greater than 400 microns. During irradiation, these agglomerates swell due to the accumulation of both solid and gaseous fission products. At 40 GWd/MT, the largest of the visible agglomerates have equivalent diameters in the 500–600 micron range.

Literature values for modern European commercial fuels indicate postirradiation agglomerate maximum equivalent diameters in the range of 250 to 400 microns for fuel average burnups in the vicinity of 45 GWd/MT. Thus, the current PIE results (and the measured preirradiation sizes) indicate that this test fuel began irradiation with a greater fraction of large agglomerates than is normally encountered in modern mixed-oxide fuels. Nevertheless, the subsequent swelling during irradiation has been as expected for the current burnup, and there have been no performance problems with this fuel. As discussed in Section 2.5, fission gas release has been no greater than that expected from the European experience.

The storage of fission gas in the vicinity of high-burnup structures is discussed in Reference 21. Fission gas initially collects in three locations: in solution in the fuel matrix, in very small (nanometer) intragranular bubbles, or in large intergranular bubbles at the grain boundaries. As irradiation proceeds, a fourth gas collection category comprises the large intergranular pores within regions in which the fuel has transformed into its high burnup structure. Whereas the large bubbles are visible by microscope, very small bubbles must be detected by EPMA, to which the larger gas collections are invisible. Stated another way, EPMA shows the fission gas in solution or in the very small intragranular bubbles, but the larger intergranular and high-burnup structure bubbles must be viewed by SEM. (See Reference 46.)

In general, a high burnup structure (small grains with a few large pores) evolves during irradiation when the local temperature is less than 1000°C and the local burnup exceeds about 60 GWd/MT. Prior to transformation, much of the fission gas is stored in nanometer-size cavities within the approximately 10-micron fuel grains. Subsequent to transformation, the grains are in the 0.5 to 1.0 micron range, in a structure interspersed with relatively large gas storage pores. The steps in the development of this structure are discussed in Reference 30. Much of the gas displaced from the very small intragranular cavities is collected (at high pressure) in the facetted pores in the recrystallized microstructure.

*This MOX test irradiation was initiated before the mission fuel was selected. It was not intended that this test fuel should be prototypic of the mission fuel, since this is the role that the lead test assemblies will play. The purpose of this test irradiation is to demonstrate the use of MOX fuel prepared with weapons-derived plutonium dioxide.

Agglomerates in the outer regions of the MOX test fuel mount surfaces are clearly visible due to their high-burnup structure. The halos surrounding these agglomerates are fission gas in surrounding UO_2 grains, which either diffused prior to transformation or was displaced when the high burnup structure was formed. Faint agglomerate outlines can be discerned in the central regions of these fuel mount surfaces at a fuel-average burnup of 40 GWd/MT. These are the beginnings of the transformation to high-burnup structure for these agglomerates. Transformation of the agglomerates in the central region was delayed due to temperatures greater than 1000°C in the central region earlier in the irradiation.

No evidence of recrystallization was found in the fuel matrix around the pellet circumference. Although the rim area experienced low temperature during irradiation, local burnups in the depleted UO_2 matrix have not reached 60 GWd/MT. It is expected that some high-burnup structure will be observed in the rim region at the next PIE, i.e., at a fuel-average burnup of 50 GWd/MT.

4. CLADDING INNER SURFACE OXIDATION

4.1 Introduction

This Chapter addresses the MOX test fuel cladding inner surface oxidation as observed for Fuel Pins 7 and 16 (Capsules 4 and 13). Both of these fuel pins had been irradiated to approximately 40 GWd/MTHM at the time of withdrawal for PIE.

There is no oxidation (or uptake of hydrides) on the cladding outer surface because the fuel pin is contained in a helium atmosphere within a stainless steel capsule during irradiation.

The observed oxidation patterns are reviewed in Section 4.2. Section 4.3 describes the means by which oxygen becomes available at the cladding inner surfaces. The European experience with cladding inner surface corrosion is discussed in Section 4.3. Finally, Section 4.4 provides a synopsis of the main points and the conclusions of this Chapter.

4.2 Oxidation Patterns

The PIE of the 40-GWd/MT Capsules 4 and 13 (Fuel Pins 7 and 16) is documented in the Volume 1 companion to this report. Chapter 5 "Metallography" includes descriptions of the oxide layers as observed at the cladding inner surfaces.

Oxidation is heaviest in regions where the pellet surface was in contact with the cladding during irradiation. The best evidence of this is in Figures 5.18 through 5.27 of Volume 1, which show the pellet-clad interface regions along an axial section (half pellet—pellet—half pellet) taken from the lower middle of the pin 7 fuel stack. Oxidation is much more prevalent along one side of the cladding than the other. However, in no case does the oxidation penetrate more than a few microns into the cladding surface.

Fuel cross-sections show arcs of relatively thick oxidation whereas the remainder of the pellet-clad circumference carries either light or spotty oxidation or is clean. Where oxidation is present, it is much thicker (10–20 microns) over surface agglomerates than the 5–10 micron thickness observed over the immediately adjacent UO_2 matrix. It is worth noting, however, that in the less-oxidized side of the axial section, even the areas over the surface agglomerates (Figures 5.24 and 5.27 of Volume 1) show little oxidation.

In some of the thicker oxidation regions, it is evident that a portion of the fuel that bonded to the cladding during irradiation remained adhered to the cladding when the pellet contracted upon cooldown. Where this occurs, cracks open within the fuel roughly parallel to the cladding surface. Good examples of this may be seen in Figure 5.11 of Volume 1.

4.3 Sources of Oxygen

Almost no oxygen was present in the MOX test fuel pin atmospheres at the time the fuel pins were sealed. Procedures at Los Alamos required a glovebox atmosphere of 99.995% helium purity with less than 10 PPM oxygen and less than 1.0 PPM moisture. Measured oxygen levels were between 0.40 and 1.65 PPM while the pellet stacks were loaded and between 0.4 and 0.8 PPM when the pin upper end caps were welded. Moisture was always recorded as less than 0.1 PPM.

There is, of course, a great deal of oxygen stored in the UO_2 and PuO_2 molecules of the fuel. Each fission thereby frees two atoms of oxygen. As discussed in Section 2.4.2, almost all of this oxygen is either bound to solid fission products (primarily Zirconium or Molybdenum) or consumed by increasing the oxygen potential of the remaining UO_2.

"Oxide Chemistry" is the subject of Chapter 5 of Reference 22. There it is explained that whereas UO_2 readily becomes hyperstoichiometric in the presence of excess oxygen, PuO_2 cannot. [The oxygen-to-metal (O/M) ratio for PuO_2 cannot exceed 2.0.] Furthermore, PuO_2 fission is more oxidizing, in the sense that a lower proportion of the fission product mix can take up oxygen. (More oxygen is released into the fuel lattice because more of the fission products are noble metals, which do not oxidize.)

When UO_2 becomes hyperstoichiometric, its oxygen potential increases dramatically. Reference 35 explains for mixed-oxide fuels that the oxygen potential "exhibits its maximum variation with O/M when the O/M = 2. Here, the anion vacancies are just all filled and any additional oxygen incorporated into the lattice must then enter interstitial positions, thereby accounting for the large increase in (oxygen potential) at this point."

4.4 Cladding Inner Surface Corrosion (Oxidation)—European Experience

Cladding inner surface oxidation has been observed in PIEs of the mixed-oxide fuel irradiated for commercial purposes in European reactors. An excellent discussion is found in Section 5.5 of Reference 13. Comparison is made of two oxide layers at a fuel-average burnup of 44.5 GWd/MT, one over a surface agglomerate and the other over a length of UO_2 matrix. The oxide layer over the agglomerate is more than twice as thick and contains slightly higher solid fission product concentrations. Both oxygen layers are similar to those observed in the current PIE.

Surface agglomerates actually protrude above the pellet surface during irradiation, pressing hard against the overlying cladding in some cases. Figure 6 of Reference 13 shows the marks left on the cladding inner surface by raised MOX agglomerates during irradiation to 44.5 GWd/MT.

There is nothing in the current PIE observations of the MOX test fuel that would tend to contradict the cladding internal oxidation process as proposed by L. Desgranes in Reference 14. Basically, the oxygen is passed from fuel to cladding by athermal diffusion promoted by the energy release of fission products. (Transport by thermal diffusion is specifically discounted.) The athermal diffusion requires that the fissioning fuel be in close range (within about 10 microns) or in contact with the cladding inner surface. Energy release by the fission products

slowing down in the fuel creates secondary recoil atoms, including oxygen, which then reach (and are implanted within) the cladding.

The prerequisite that the fuel be in close proximity to the cladding also explains the European experience that cladding internal corrosion thicknesses of about 5 microns appear quite suddenly, when fuel burnups have reached about 25 GWd/MT. Until the cladding becomes "in-range," the oxygen freed by fission is consumed by occupying interstitial positions in the remaining UO_2 lattice and thereby rendering the fuel hyperstoichiometric. This interstitial oxygen is more lightly bound, and when the pellet-clad gap is sufficiently narrowed, this excess oxygen is unloaded into the cladding, causing a very rapid initial formation of the corrosion layer. Subsequently, the layer thickness increases slowly as additional oxygen is freed.

Fission products that penetrate the cladding inner surface by direct recoil also play a role in preparing the surface for oxidation. This concept is buttressed by the interesting experiment described in Reference 36. The in-reactor corrosion rates of Zircaloy-4 were found to be significantly accelerated by trace levels of fissile impurities "due to irradiation-enhanced diffusion of the oxidizing species as a result of fissioning within the oxide along with easier diffusion paths created by the fission tracks." "Fissioning of the fissile impurities yields energetic fission fragments that tear through the growing oxide and affect the corrosion process by (1) accelerating the pre-transition and post-transition corrosion rates and (2) delaying the transition…"

4.5 Discussion and Conclusions

There was no indication of cladding inner surface corrosion in the early (8 GWd/MT) PIE. An isolated instance of surface agglomerate—clad bonding was observed (Figure 5.9 of Reference 31) in the intermediate (21 GWd/MT) PIE. Additional instances of bonding over surface agglomerates were noted at 30 GWd/MT (Figures 5.7 and 5.8 in Reference 32). Widespread bonding over agglomerates and sporadic areas of general corrosion in the absence of agglomerates are first seen in the current (40 GWd/MT) PIE.

Based on the European literature, cladding inner surface corrosion requires that excess oxygen be available and that the fuel be in contact with the cladding to provide a path for solid-state athermal (fission-fragment-induced) diffusion of the oxygen atoms. Excess (interstitially-located) oxygen becomes increasingly available as the oxygen freed by fission brings the UO_2 to a hyperstoichiometric state. Thus, the amount of loosely bound oxygen available for athermal diffusion to the cladding inner surface increases with burnup.

The amount of pellet surface in contact with the cladding is not easily characterized. Pellet hourglassing due to a greater axial thermal expansion along the pellet centerline distorts the initial fuel shape. For the MOX test fuel, this brought the pellet ends in contact with the cladding on initial heatup. Subsequent cracking (both radial and axial) brought fuel fragments located more toward the pellet midplane into one-sided or point contact with the cladding. In general, wherever a portion of fuel surface approached the cladding, contact was first made over any surface agglomerates, since these protrude above the surrounding pellet surface during irradiation.

Thus, the uneven and noncontiguous nature of the observed corrosion is simply a matter of the manner in which the pellet fragments came into contact with the cladding during irradiation. The thicker corrosion over the agglomerates follows directly from the narrower pellet-clad gap at their location during irradiation. It is concluded that the observed cladding corrosion patterns are in accordance with expectations based upon the documented European experience.

5. MOX FUEL DENSIFICATION AND SWELLING

5.1 Introduction

Three metallographic mounts were prepared from Capsule 1 (Fuel Pin 2) after Phase I of the MOX test, see Reference 38 [early (9 GWd/MT) PIE final report]. Following completion of Phase II, two mounts were prepared from Capsule 2 (Fuel Pin 5) and two from Capsule 9 (Fuel Pin 12); descriptions of the sample preparation, polishing and etching techniques are presented in Chapter 5 of Reference 31 [intermediate (21 GWd/MT) PIE final report]. Following completion of Phase III, two mounts were prepared from Capsule 3 (Fuel Pin 6) and two from Capsule 10 (Fuel Pin 13), see Chapter 5 of Reference 32, Volume 1 (30 GWd/MT PIE final report). After completion of Phase IV-Part 1, five mounts were prepared from Capsule 4 (Fuel Pin 7) and three from Capsule 13 (Fuel Pin 16), see Chapter 5 of the companion Volume 1 (Reference 39) of this report.

Altogether, nineteen metallographic mounts of diametral cross-sections have been prepared from fuel pins withdrawn after Phases I, II, III, and IV-Part 1 of the weapons-derived MOX test irradiation. The mount identification numbers, fuel type, and axial locations are given in Table 5.1. (Pellet 1 is located adjacent to the fuel pin gas plenum; fuel type B was TIGR-treated.)

Table 5.1. Fuel Pin Metallographic Mount Identification

Irradiation Phase	Met. Mount Ident. Number	Capsule	Fuel Pin	Fuel Type	Axial Location (Pellet Number)	Comments
I	6139	1	2	A	5	
I	6140	1	2	A	5/6 interface	
I	6141	1	2	A	6	
II	6143	9	12	B	1	
II	6144	9	12	B	14	
II	6145	2	5	A	1	
II	6146	2	5	A	14	
III	6161	3	6	A	1	
III	6162	3	6	A	15	
III	6163	10	13	B	1	
III	6164	10	13	B	15	
IV-Part 1	6217	4	7	A	Bottom of 1	Excessive pull-outs, not used
IV-Part 1	6218	4	7	A	Top of 2	
IV-Part 1	6219	4	7	A	Top of 10	
IV-Part 1	6220	4	7	A	Middle of 10	
IV-Part 1	6222	4	7	A	Top of 15	
IV-Part 1	6223	13	16	B	Bottom of 1	
IV-Part 1	6225	13	16	B	Top of 15	
IV-Part 1	6240	13	16	B	2	

In addition to the diametral metallographic mount cross-sections, two axial metallographic mounts have been prepared. MET Mount 6167 was prepared from Phase III Fuel Pin 13 comprising pellets 7 through 9; and MET Mount 6221 was prepared from Phase IV-Part 1 Fuel Pin 7 comprising pellets 11 through 13. Both axial mounts indicate stable fuel behavior with distinct pellet dishing and chamfer clearly visible; also, no significant pellet/cladding interaction effects are seen.

The PIE metrology of the Phase I capsules (1 and 8) and fuel pins (2 and 11) is contained in Chapter 4 of Reference 38. The Phase II capsule (2 and 9) and fuel pin (5 and 12) PIE metrology is given in Chapter 4 of Reference 31. The Phase III capsule (3 and 10) and fuel pin (6 and 13) PIE metrology is given in Chapter 4 of Reference 32. The Phase IV-Part 1 capsule (4 and 13) and fuel pin (7 and 16) PIE metrology is given in Chapter 4 of the companion Volume 1 (Reference 39).

Subsequent to issue of the Phase II final PIE report and before the Phase III PIE, an innovative Fuel Pin Measuring Apparatus (FPMA) was developed (Reference 40) for precise measurement of the outer cladding surface profile. Additionally, an improved dial indicator and V-block type apparatus was employed for the Phase III quick-look PIE report (Reference 41). Both the V-block and the FPMA were calibration-verified before and after measuring the Phase III fuel pins. The V-block reproduced the calibration standard within 0.0002 inches and the FPMA within 0.0001 inches. Also, for the Phase III fuel pin measurements, there was excellent correspondence between the two methods of measurement (agreement within the apparatus uncertainties at all measurement locations).

The FPMA profilometry measurements of the Phase III and Phase IV-Part 1 fuel pins (approximately 300 axial points per pin over the six inch fuel length) indicate localized diametral peaks (“ primary ridging”) of the cladding overlying the pellet-to-pellet interfaces. This ridging is caused by hard pellet-to-clad interactions due to differential axial thermal expansion within the fuel pellet during power operation; engineering models and calculations illustrating this “hourglassing” phenomena are presented in Chapter 6 of the 30 GWd/MT PIE Implications report (Reference 37). After ridging was observed in the Phase III fuel pins, long segments of the archived Phase I and II fuel pins were defueled and then measured via the FPMA. These measurements also show ridges indicating that hard pellet-to-clad contact (sufficient to cause local yielding) occurred early in the irradiation, during the initial heatup in the ATR.

FPMA takes two sets of measurements on a fuel pin. Each measurement consists of four diametral measurements 90 degrees apart for each of several hundred axial positions. The second set of diametral measurements is taken after rotating the fuel pin 45 degrees from the first set (same axial locations). This allows the determination of the fuel pin diameter and circumferential distortion of the clad. To date, no cladding ovality or distortion has been discerned, even with the Phase I and II fuel pin cutting and defueling operations. The fact that the fuel pins could be easily withdrawn from their very close fitting capsules provides mechanical verification that there are no gross fuel pin distortions.

The FPMA profilometry of the fuel pins provides reproducible diametral measurements, much more accurate than the dial indicator and V-block type metrology apparatus employed in the Phase I and II PIEs. Furthermore, the FPMA can automatically collect large amounts of data in a

short time and is not as susceptible to the operational and mechanical difficulties of manual operations in a hot cell as is the V-block metrology device. Because of these advantages, FPMA profilometry of the fuel pins has been used exclusively for the 40 GWd/MT PIE and is now the method of choice. The ability to collect large amounts of accurate data has made the detailed analysis of the fuel pin ridging and creep possible.

This Chapter performs a re-assessment of the MOX fuel densification and swelling given the additional data from the 40 GWd/MT PIE. (The previous assessment is found in Chapter 5 of Reference 37.)

The capsule and fuel pin metrological results and measurements made directly from photographic enlargements of the metallographic mounts are employed in this Chapter to determine:

- the fuel pin Zircaloy cladding thickness and internal diameter,
- the free area within the fuel pin (that is, the peripheral gap between the fuel and the clad, and the internal cracks within the fuel pellet), and
- the fuel pellet equivalent outer diameter (representing all internal cracks as closed, with their areas added as part of the corresponding pellet-clad gap).

These quantities are determined for each of the Phase IV-Part 1 metallographic mounts using the imaging software Image-Pro Plus, Version 4.1 (Reference 42).

These data are presented as functions of fuel burnup in Section 5.2. Conclusions are discussed in Section 5.3. These data are used as described in Section 5.4 to assess the fuel densification assumptions currently employed with the CARTS code fuel swelling models.

5.2 Capsule Component Dimensions

Note: This Section describes in detail the measurement methods (metrology) used and the actual data analyses performed to determine the cladding and pellet dimensions from observations of the irradiated fuel metallographic (MET) mounts. Readers not interested in the pursuit of such detail are encouraged to skip ahead to Section 5.3, where the results are summarized.

5.2.1 As-Built Dimensions

A compilation of the as-built MOX capsule and fuel pin dimensions, taken from the ORNL component inspection reports and the LANL fuel QA reports, is provided in Table 5.2. Also included are the construction tolerances for these components. Per the construction drawings, the MOX pellet outer diameter, the capsule and cladding inner and outer diameters, and the capsule and cladding inner and outer diameter concentricities are specified. The cladding thickness and pellet-to-clad gaps are derived values based on the construction or as-built component ranges.

Table 5.2. MOX Capsule and Fuel Pin Dimensions

Item	Construction Tolerance (in.)	As-Built Range[1] (in.)	As-Built Mean and Uncertainty[1] (in.)
Capsule OD	0.4640 – 0.4650	0.4643 – 0.4649	0.4646 ± 0.0003
Capsule ID	0.3830 – 0.3835	0.3830 – 0.3835	0.38325 ± 0.00025
Cladding OD	0.3805 – 0.3810	0.3805 – 0.3808	0.38065 ± 0.00015
Cladding ID	0.3290 – 0.3295	0.3290 – 0.3294	0.3292 ± 0.0002
Cladding Concentricity	Radius 0.0010	Radius 0.00045[2]	
MOX Pellet OD	0.3260 – 0.3270	0.3260 – 0.3265	0.32625 ± 0.00025
Cladding Thickness (calculated)	0.0245 – 0.0270	0.0251 – 0.02635	0.02573 ± 0.00063
Pellet to Cladding Radial Gap (calculated)	0.0010 – 0.00175	0.00125 – 0.0017	0.00148 ± 0.00023
Cladding to Capsule Radial Gap (calculated)	0.0010 – 0.0015	0.0011 – 0.0015	0.0013 ± 0.0002

[1]For the eight withdrawn capsules (irradiated during Phases I, II, III, and IV-Part 1).
[2]Maximum observed.

5.2.2 Capsule Outer Diameter

The preirradiation value for the stainless steel capsule outer diameter for Capsules 1, 2, 3, 4, 8, 9, 10, and 13 is reported as 0.4643-to-0.4649 inches (Table 5.2). Here 0.4643 inches is the minimum measured outer diameter, while 0.4649 inches is the maximum measured outer diameter.

The post-irradiation hot cell capsule measurements are given in Table 5.3. The estimated accuracy of the hot cell capsule diametral measurement is ±0.0005 inches; these measurements were performed with a dial indicator and V-block type apparatus.

As shown in Table 5.3, using the preirradiation dimensions for the stainless steel capsule, the measured capsule temperature (at the mid-point, within the fueled region) in the hot-cell and the

Table 5.3. Measured Capsule Outer Diameters

Irradiation Phase	Capsule Number	Meas. Capsule Surf. Temp./ Hotcell Ambient Temp. (°C)	Calc. Capsule Diameter Range (inches)	Meas. (Hotcell) Capsule Dia. (av. of 6 obs.) (inches)	Standard Dev. About the Mean (mils)
I	1	40.4/28.8	0.46445–0.46505	0.46462	0.16
I	8			0.46515	0.12
II	2	51.8/30.0	0.46453–0.46513	0.46532	0.17
II	9	53.2/30.2	0.46454–0.46514	0.46510	0.18
III	3	47.5/29.8	0.46450–0.46510	0.46557	0.12
III	10	47.8/30.0	0.46450–046510	0.46498	0.10
IV-Part 1	4	56.5/30.0	0.46456–0.46516	0.46550	0.23
IV-Part 1	13	56.8/29.8	0.46456–0.46516	0.46542	0.10

thermal linear expansion formulation for 304 stainless steel (from CARTS), the calculated hot-cell capsule outer diameter lies in the range from 0.46445-to-0.46516 inches. This range essentially spans the observed measurements (with uncertainties); there is no observed change in the measured capsule outer diameter that can not be explained simply by thermal expansion.

5.2.3 Fuel Pin Cladding Outer and Inner Diameters

The nominal as-constructed outer diameter of the fuel pin Zircaloy cladding is 0.3810 inches (with tolerances of +0.0000 and –0.0005 inches). The preirradiation value for the Zircaloy cladding outer diameter for Fuel Pins 2, 5, 6, 7, 11, 12, 13, and 16 is reported as 0.3805-to-0.3808 inches (Table 5.2).

The PIE metrology results for the cladding outer diameter include positions outside the six-inch fueled region, which extends from one to seven inches as measured from the top of the fuel pin. Table 5.4 contains averages of the FPMA fuel pin diameter measurements taken within the fueled region during the PIEs conducted to date.*

Figure 5.1 shows how the average irradiated cladding outer diameters measured at hot cell temperature during the sequential PIEs increase with burnup. Applying the thermal linear expansion formulation for Zircaloy (from CARTS) with the measured cladding temperatures, the diameters of the fuel pins would range from 0.38054-to-0.38084 inches as measured in the hot cell. The average cladding outer diameters (including the computed uncertainty) plotted in Figure 5.1 for the 30 and 40 GWd/MT withdrawal fuel pins are greater than this range of values, and hence cannot be accounted for by thermal expansion alone.

The FPMA profiles of all withdrawn fuel pins (all PIEs to-date) contain “peaks” (ridges corresponding to pellet-to-pellet interfaces) and “valleys” (corresponding to the low points over the pellet midplanes). The profilometry of Fuel Pin 7, illustrating the peaks and valleys, is shown in Figure 5.2.

The Fuel Pin 7 average outer diameter plotted in Figure 5.1 (for Phase IV-Part 1) is the average of the outer diameters (from 0.618 to 6.038 inches along the fuel pin length, excluding the distortions caused by the weldments of the upper and lower fuel pin plugs) including the peaks and valleys. As shown in Figure 5.2, there is a difference of approximately 0.27 mils between the average peak height and the average valley. Figure 5.1 can be expanded, as shown in Figure 5.3, to indicate the trends for the peaks and valleys for all withdrawn fuel pins.

The peaks or ridging are caused by hard pellet-clad interactions due to differential axial thermal expansion within the fuel pellet during irradiation. Ridging has been observed in all of the withdrawn fuel pins via the FPMA measurements. This indicates that hard pellet-clad contact occurred early in the irradiation, at the initial heatup for the first cycle in the ATR.

*The FPMA was developed subsequent to the PIEs for Irradiation Phases I and II. Thus, full-length metrology for Fuel Pins 2, 5, 11, and 12 is not available. For these pins, FPMA measurements were taken (during the Phase III PIE) on the cladding segments that had been retained for later clad ductility testing.

Table 5.4. Measured Fuel Pin Outer Diameters

Irradiation Phase	Burnup (Radio. Chem.) (GWd/MT)	Burnup (MCNP[1]) (GWd/MT)	Burnup (FRAPCON-3[2]) (GWd/MT)	Fuel Pin	Clad Average Outer Diameter (inches)	Standard Dev. About the Mean (mils)
I	7.95[3] ± 0.40	8.63 ± 0.60	8.553 (+1.197/–0.253)	2	0.38073	0.07
I		8.54 ± 0.60	8.493 (+1.197/–0.253)	11	0.38090	0.15
II	22.2[3] ± 1.11 21.3[4] ± 1.07	20.90 ± 1.46	20.853 (+3.747/–1.073)	5	0.38084	0.14
II	21.5[4] ± 1.08	20.95 ± 1.47	20.935 (+3.755/–1.075)	12	0.38096	0.16
III	27.6[5] ± 1.38	29.66 ± 2.08	29.068 (+4.452/–1.898)	6	0.38104	0.11
III	27.8[5] ± 1.39 26.9[6] ± 1.35	29.61 ± 2.07	29.603 (+4.547/–1.933)	13	0.38118	0.11
IV-Part 1	41.8[7] ± 2.09 38.7[8] ± 1.94 38.0[9] ± 1.90 41.1[4] ± 2.06	38.98 ± 2.73	38.921 (+2.979/–0.511)	7	0.38148	0.11
IV-Part 1	41.9[7] ± 2.10 39.2[10] ±1.96 41.1[4] ± 2.06	38.98±2.73	38.920 (+3.700/–0.930)	16	0.38176	0.12

Notes:

[1]LHGR-estimated burnup from MCNP calculations performed by G. Chang at INEEL.

[2]R-Z FRAPCON-3 model with 15 axial segments (one for each MOX pellet in fuel stack); based on MCNP calculated cycle-average LHGRs and axial peaking, and actual cycle EFPDs.

[3]Pellet number 2 (from fuel pin gas plenum).

[4]Pellet number 15.

[5]Pellet number 10.

[6]Pellet number 9.

[7]Pellet number 1.

[8]Pellets number 2 through 9.

[9]Pellet number 11.

[10]Pellets number 2 through 14.

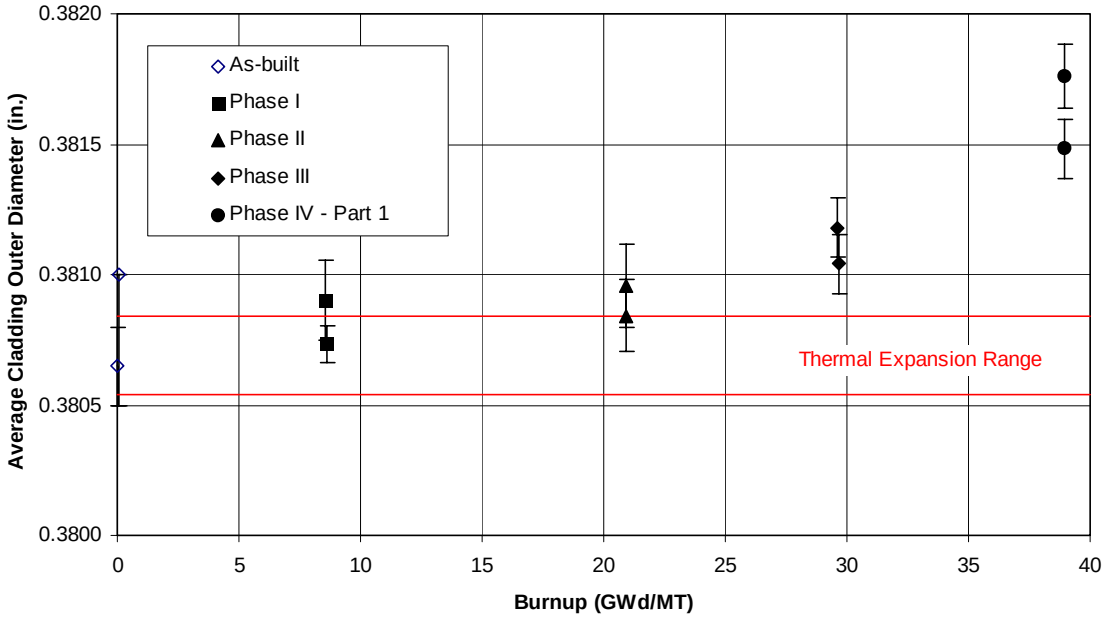

Fig. 5.1. Cladding outer diameter vs burnup—cold dimensions.

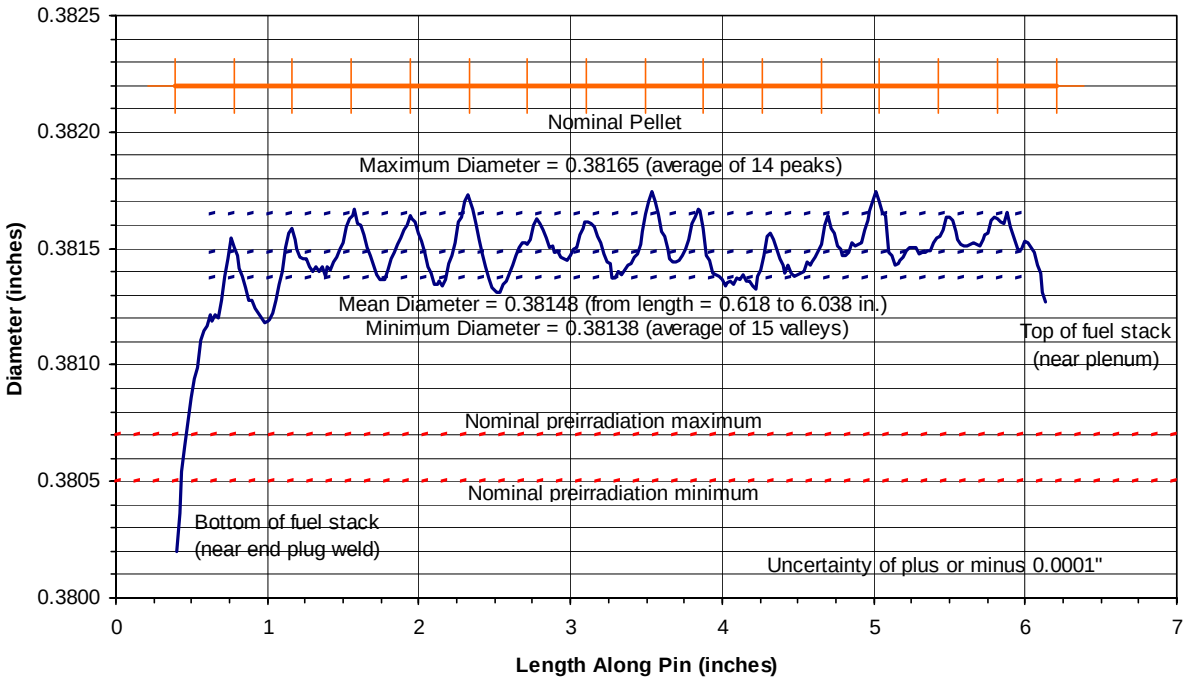

Fig. 5.2. Fuel Pin 7 profilometry—cold dimensions.

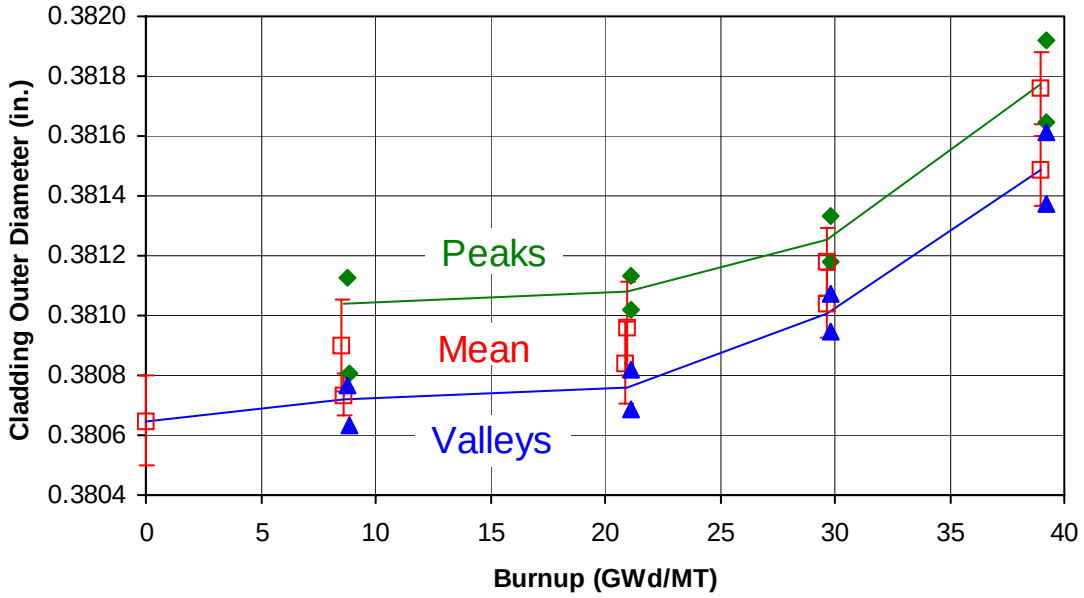

Fig. 5.3. Cladding outer diameter with "peaks" and "valleys" vs burnup—cold dimensions.

In the 30 GWd/MT PIE Implications report, it was stated that the observed outward cladding expansion was greater than would be expected for irradiation creep under the low (~1–2 MPa) wall tensile stresses calculated for the Phase III fuel pins. It was also conjectured that the major contributing factor must be mechanical dragging due to pellet hourglassing, which forces the cladding outward at points overlying the pellet-pellet interfaces. As shown in Figure 5.3, the relative difference between the "peaks" and "valleys" is approximately the same for all withdrawn MOX fuel pins. The apparent cladding creep outward is not a function of the formation of the cladding ridges; as shown in Figure 5.3, the valleys at burnups of 9- and 21 GWd/MT are within the as-built outer diameter tolerances.

With increased irradiation exposure and higher fuel pin internal pressures (due to additional fission gas release), the valleys of the 30 and 40 GWd/MT fuel pins are greater than the as-built outer diameter tolerances. Furthermore, Figure 4.26 of Volume 1 (Reference 39) clearly shows that small wall tensile stresses (~5 MPa) in the pressurized Fuel Pin 16 produced a measurable increase (0.2–0.3 mil) in the FPMA-determined fuel pin outer diameter (as compared with the unpressurized fuel pin).

Irradiation induced growth in anisotropic materials such as Zircaloy requires no applied stress to produce a shape change at constant volume (Ref. 22, pp 176–177). Cold-working purposefully orients the hexagonal lattice such that the major <c> axis is normal to the axial direction of the cladding tube. Irradiation then produces a contraction in the <c> direction and expansion normal to this direction. The cladding tube lengthens slightly while the wall thins to maintain constant volume.

On the other hand, the outward cladding creep occurring during the MOX test irradiation is the product of an applied wall stress. It is believed that the valley diameters are representative of the extent of outward relocation. (The ridges, caused by pellet hourglassing, are independent of creep.) All the ingredients for creep are present: neutron irradiation, cladding wall tensile stress; and a cladding temperature during irradiation of 320°–400°C.

Chapter 6 of this report discusses the observed cladding creep for these fuel pins and develops an appropriate empirical correlation (a function of the integral of the product of the cladding wall stress and exposure). This correlation is compared with Halden creep data and literature creep correlations. However, in general, literature values are usually derived from PWR experience, where the creep is inward, not outward. Where outward clad creep experiments have been performed, the tensile wall stresses are almost always 60 MPa or greater.

There is slightly greater creep-out of the cladding for the TIGR-treated fuel; this behavior is illustrated in Figure 5.4. As shown in Table 2.4, the measured pressures in the fuel pins with TIGR-treated fuel were always higher than those for their untreated counterparts. With a greater wall hoop stress, additional creep is to be expected. The post-PIE CARTS calculations (Chapter 7) employ empirical models for the cladding creep histories shown in Figure 5.4, as functions of fuel type and burnup.

The fuel pin cladding inner diameter will now be considered. The nominal construction inner diameter of the Zircaloy cladding is 0.3290 inches (with tolerances of +0.0005 and –0.0000 inches). The preirradiation value for the cladding inner diameter for Fuel Pins 2, 5, 6, 7, 11, 12, 13, and 16 is reported as 0.3290-to-0.3294 inches (Table 5.2).

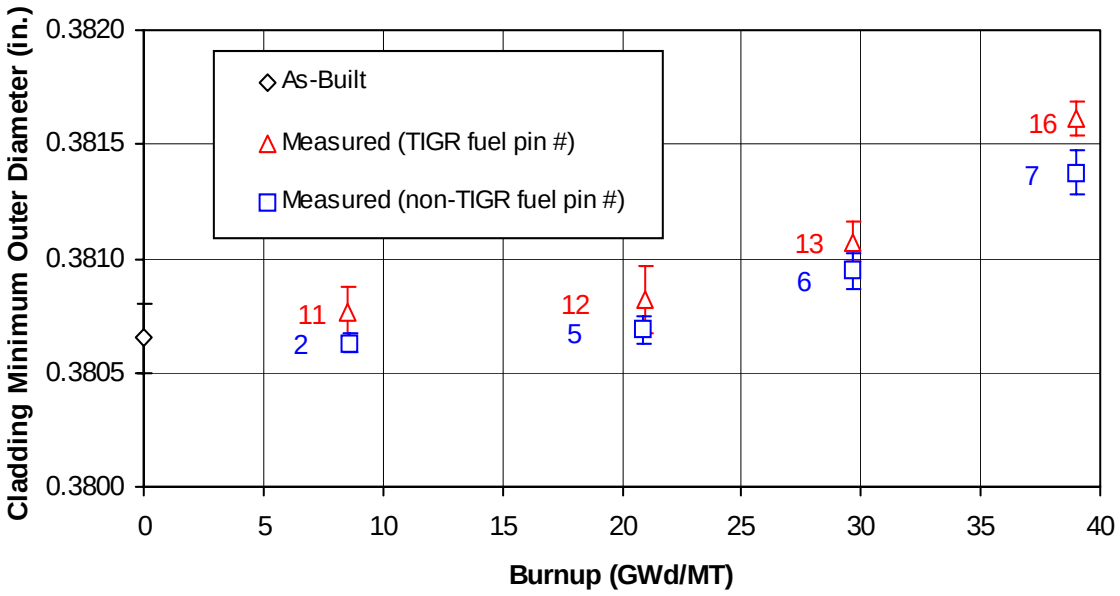

Fig. 5.4. Cladding outer diameter valleys as functions of fuel type and burnup.

The post-irradiation inner diameter is obtained from the PIE measurement of the outer diameter by subtracting the cladding thickness as measured directly from photographic enlargements of the metallographic mounts. For the 30 and 40 GWd/MT PIE MET mounts, the original location of the mount face is precisely known; therefore, the cladding outer diameter is known within the uncertainty range of the FPMA measurement. However, for the 9- and 21-GWd/MT mounts, diametral measurements cannot be precisely correlated with the original locations of the mount faces. Hence, the average of the FPMA measurements for these fuel pins is used as the cladding outer diameter, from which the inner diameter is calculated. Finally, the uncertainties* in the cladding outer diameter and cladding thickness are propagated inward to yield the uncertainty in the inner diameter.

The cladding internal diameter is not determined directly from the mounts. What appears to be full cross-sections of the cladding and fuel in Volume 1 (Figure 5.28, for example) are actually reduced composites (ergo collages) of high-magnification photographs of the mounts. There is distortion in the composite images. The cladding thicknesses reported in Table 5.5 are means of approximately 40 measurements (per MET mount) from the more accurate high-magnification photographs.

A compilation of the mean measured cladding thickness for each metallographic mount is given in Table 5.5 and plotted versus fuel burnup in Figure 5.5. As shown, the measured cladding thicknesses of all mounts lie within the pre-irradiation as-built values plus uncertainties.

Table 5.5. Fuel Pin Cladding Thickness

Irradiation Phase	Met. Mount Ident. Number	Capsule	Fuel Pin	Clad Thickness (inches)	Uncertainty in Clad Thickness (mils)
I	6139	1	2	0.02592	0.24
I	6140	1	2	0.02603	0.24
I	6141	1	2	0.02582	0.30
II	6143	9	12	0.02583	0.26
II	6144	9	12	0.02578	0.22
II	6145	2	5	0.02571	0.23
II	6146	2	5	0.02565	0.21
III	6161	3	6	0.02569	0.20
III	6162	3	6	0.02546	0.11
III	6163	10	13	0.02554	0.19
III	6164	10	13	0.02536	0.18
IV-Part 1	6218	4	7	0.02575	0.15
IV-Part 1	6219	4	7	0.02559	0.13
IV-Part 1	6220	4	7	0.02557	0.15
IV-Part 1	6223	13	16	0.02562	0.18
IV-Part 1	6225	13	16	0.02537	0.07

*Because their mount faces may represent anywhere between valley and peak, the uncertainties stated in Table 5.4 for the cladding outer diameters of Fuel Pins 2, 11, 5, and 12 are probably underestimated. Referring to Figure 5.3, the average difference between peak and valley is about 0.3 mil, which is as much as four times greater than the uncertainties listed in Table 5.4. These uncertainties will be reevaluated when the measurements for the 50 GWd/MT fuel pins become available.

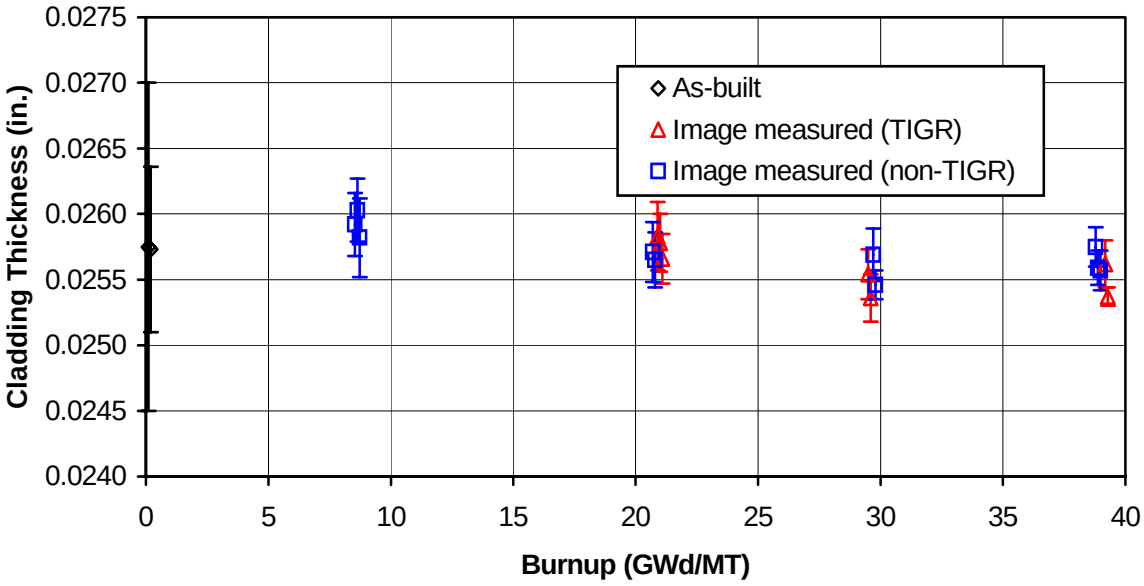

Fig. 5.5. Cladding thickness vs burnup—cold dimensions.

With both cladding growth and the observed outward creep, the cladding thickness should decrease with burnup. Considering constant volume with the maximum observed creep (Fuel Pin 16, Table 5.4 and Figure 5.1), the associated decrease in cladding thickness is about 0.09 mil. The uncertainties listed for the thickness measurements in Table 5.5 are generally 2–4 times this value. In other words, the measurement uncertainties are much greater than the expected decrease in the cladding thickness.

The calculated cladding inner diameter and associated uncertainty for each metallographic mount are presented in Table 5.6.

The cladding inner diameters are shown as a function of burnup in Figure 5.6. The derivation of the pellet diameters is discussed in the next two Sections. However, it is of interest to consider these in conjunction with the cladding diameters, so the pellet diameters are shown in the lower portion of Figure 5.6.

Figure 5.6 shows a decrease in the pellet equivalent diameters from the unirradiated state to the Phase-I burnup (~9 GWd/MT), then an increase in diameter (at ~21 GWd/MT burnup) followed by another decrease (at ~29.6 GWd/MT). Obviously, if taken literally, the behavior suggested by the 21 GWd/MT data would be contrary to expected fuel response. Fuel densification and swelling occur simultaneously in the early phases of fuel irradiation; and with the rate of densification being greater than the swelling rate, the pellet equivalent diameter will decrease. Once densification is complete (by about 10–15 GWd/MT burnup), solid and gaseous fission product induced fuel swelling will increase monotonically with irradiation.

Table 5.6. Fuel Pin Cladding Inner Diameter

Irradiation Phase	Met. Mount Ident. Number	Capsule	Fuel Pin	Clad Inner Diameter (inches)	Uncertainty in Inner Diameter (mils)
I	6139	1	2	0.32890	0.48
I	6140	1	2	0.32868	0.48
I	6141	1	2	0.32909	0.61
II	6143	9	12	0.32933	0.54
II	6144	9	12	0.32943	0.48
II	6145	2	5	0.32942	0.48
II	6146	2	5	0.32955	0.44
III	6161	3	6	0.32958	0.42
III	6162	3	6	0.33007	0.24
III	6163	10	13	0.33007	0.38
III	6164	10	13	0.33068	0.37
IV-Part 1	6218	4	7	0.33006	0.31
IV-Part 1	6219	4	7	0.33035	0.27
IV-Part 1	6220	4	7	0.33018	0.32
IV-Part 1	6223	13	16	0.33060	0.37
IV-Part 1	6225	13	16	0.33066	0.17

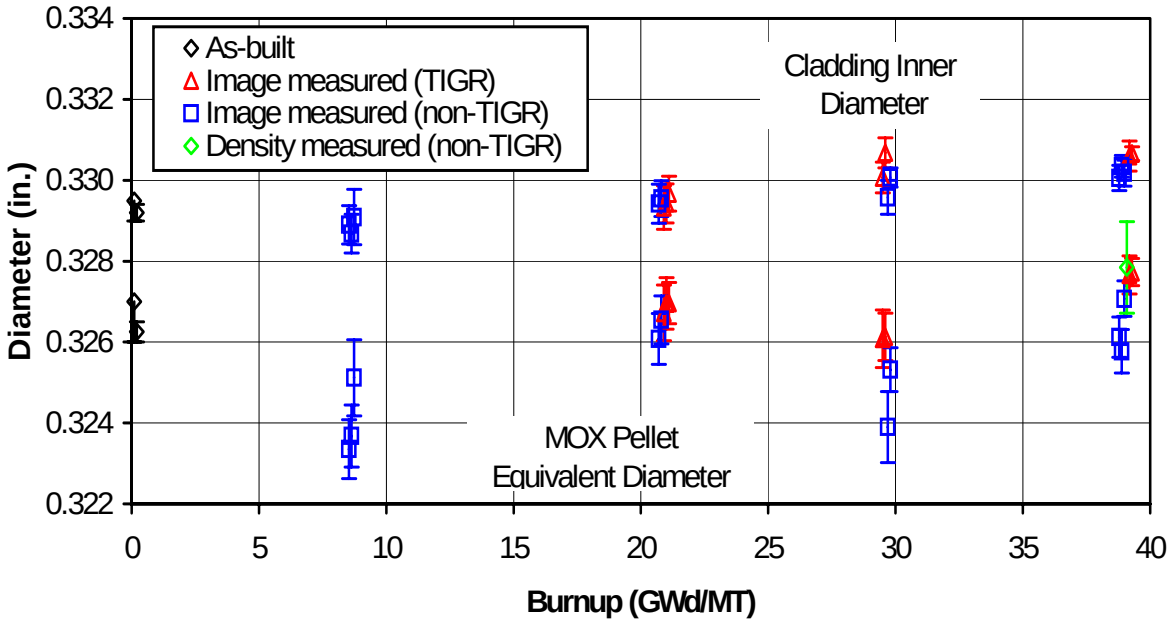

Fig. 5.6. Clad and pellet diameters vs burnup—cold dimensions.

The data shown in Figure 5.6 represent fuels irradiated at different axial positions relative to the ATR core at different LHGRs and should be treated as independent observations. R. N. Morris (ORNL) has assessed the data in Table 5.6 assuming an uncertainty of 0.5% for the diameter measurements. With this uncertainty, he is able to pass a smooth curve representative of densification followed by swelling through all data ranges. His results are close to those obtained by CARTS and discussed in Section 5.4, with a slightly lower extent and period of densification, and a swelling rate of 0.07% as compared with the 0.077% used with CARTS and FRAPCON-3. This demonstrates that the ranges for the 9- and 21-GWd/MT burnups appear out of place in Figures 5.6 and 5.7 only because the plotted uncertainty ranges are too small.

As discussed previously, it is believed that the uncertainties in the 9- and 21-GWd/MT measurements are underestimated. These will be reassessed when the measurements for the 50 GWd/MT fuel pins are available. Section 5.4 assesses the "general" trends in the fuel densification and swelling behavior.

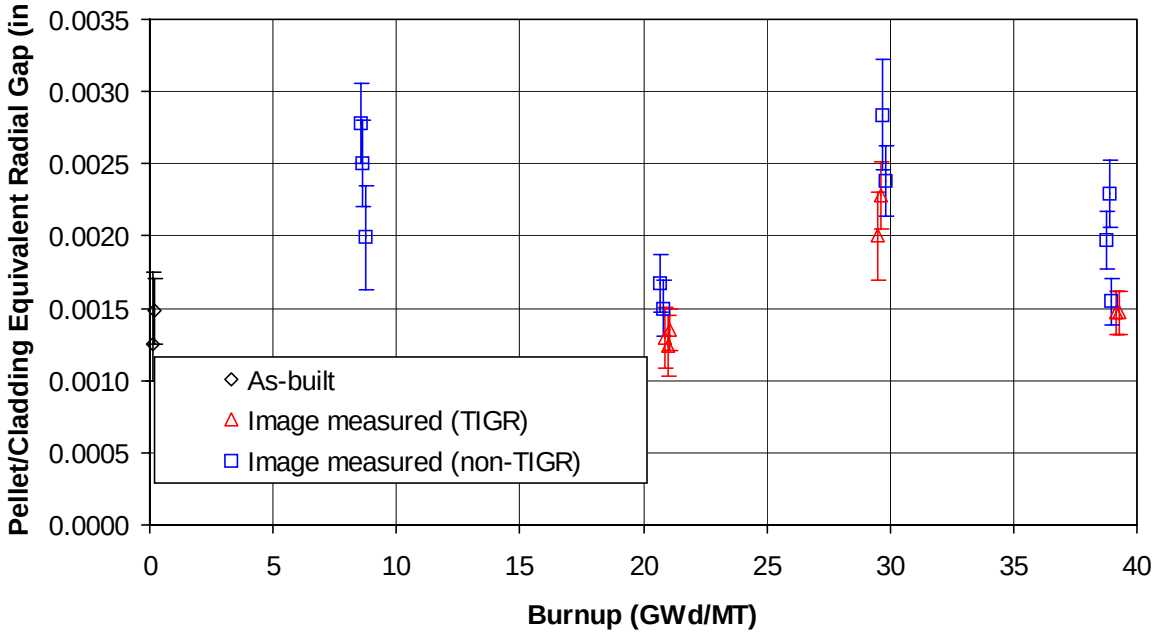

Fig. 5.7. Equivalent radial gap vs burnup—cold dimensions.

5.2.4 Fuel to Clad Radial Gap

Reviewing the metallographic mounts illustrated for the 40 GWd/MT withdrawals in Chapter 5 of Volume 1, the appearance of the fuel is normal (with cracks caused by thermal stresses during ATR operation and thermal cycling, i.e., startups and shutdowns), and is consistent with the appearances of MET mounts prepared during previous PIEs.

Under hot cell conditions, there is less than 1°C difference between capsule surface and fuel centerline temperatures, both of which are within 25°C of the hot cell ambient temperature (about 30°C). At such low temperatures, there is little thermal expansion of the capsule components; thus existing cracks within the fuel and the peripheral gaps between fuel and cladding are all larger than during reactor operation. High fuel temperatures during operation and the associated thermal expansion tend to close the internal cracks and peripheral gaps.

From the enlarged photographs of the metallographic mounts, the free area within the fuel pin (gaps and cracks) can be estimated. This free area does not include the porosity within the fuel or the "pullouts" in the mounts (which did not exist during irradiation and were subsequently caused by loss of friable material during mount preparation).

Generally, the portion of the free area within the cracks (at hot cell conditions) for these metallographic mounts is greater than the portion in the peripheral gap. The total free area can be used to calculate an equivalent peripheral gap (that is, an adjusted gap between the fuel and cladding which includes all the free area within the fuel pin). In effect, the pellet segments are considered to be pushed together so that the internal cracks disappear. This approach is consistent with the manner in which fuels codes treat the gap and cracks within the fuel pin. This equivalent gap can then be compared with the predictions of the fuels codes (such as CARTS).

The adjusted fuel-to-clad peripheral gap and uncertainty for each metallographic mount are listed in Table 5.7.

The fuel-to-clad radial gap is shown as a function of burnup in Figure 5.7. Prior to irradiation, the construction tolerances allow the radial gap to range from 1.00 to 1.75 mils. This

Table 5.7. Fuel to Clad Radial Gap

Irradiation Phase	Met. Mount Ident. Number	Capsule	Fuel Pin	Adjusted Gap (mils)	Uncertainty in Gap (mils)
I	6139	1	2	2.78	0.28
I	6140	1	2	2.50	0.30
I	6141	1	2	1.99	0.36
II	6143	9	12	1.30	0.21
II	6144	9	12	1.24	0.21
II	6145	2	5	1.67	0.20
II	6146	2	5	1.50	0.19
III	6161	3	6	2.84	0.38
III	6162	3	6	2.38	0.24
III	6163	10	13	2.00	0.30
III	6164	10	13	2.28	0.23
IV-Part 1	6218	4	7	1.97	0.20
IV-Part 1	6219	4	7	2.29	0.23
IV-Part 1	6220	4	7	1.55	0.16
IV-Part 1	6223	13	16	1.47	0.15
IV-Part 1	6225	13	16	1.47	0.15

construction range and also the smaller as-built range are illustrated at the zero burnup point in Figure 5.7.

As shown in Figure 5.7, the gap at ~8.6 GWd/MT burnup is wider than the gap at BOL. This behavior is prototypic of commercial fuel; that is, the fuel densifies (i.e., shrinks in volume) in the early phase of irradiation.

The fuel densification and swelling phenomena are discussed in Reference 43 (Chapter 6), including an excellent graphical presentation (Figure 6.1) of commercial fuel (Siemens) densification and swelling. In general, densification is very rapid in the first 10 GWd/MT of burnup and is complete by 10–15 GWd/MT. Fuel densification and swelling are essentially competing effects; early in the irradiation densification dominates and the fuel volume shrinks, but after densification is complete, swelling continues in direct proportion to the burnup.

As noted near the end of Section 5.2.3, the irradiation histories and axial positions relative to the ATR core midplane are different for the fuel pins withdrawn after each irradiation phase. These independent observations should be treated as test data. Section 5.4 assesses the general trends in the observed fuel behavior.

5.2.5 Fuel Pellet Outer Diameter

Given the Zircaloy cladding inner diameter (from Section 5.2.3) and the equivalent peripheral gap between fuel and cladding (from Section 5.2.4), the fuel outer diameter (i.e., in the absence of internal cracking) can be calculated by subtracting the latter from the former. The fuel pellet outer diameter and uncertainty for each metallographic mount are given in Table 5.8.

The range of pellet equivalent diameters is shown as a function of burnup in Figure 5.6. Prior to irradiation, the construction tolerances allow a range in the pellet diameter of 0.3260 to 0.3270 inches. This is the initial range shown at zero burnup.

During the Phase IV-Part 1 PIE, a device (Fuel Pin Volume Measuring Apparatus, see Reference 4) was developed to determine the fuel pin free volume via a gas-back-fill technique. An adaptation of this device also allows the determination of a specimen volume. The volume of a small sample (~0.5 inch) of cladding and fuel from Fuel Pin 7 was measured; and, given the sample mass, the fuel density was determined (Section 4.7.2 of Volume 1) to be 10.2 g/cm^3. This irradiated fuel density (at a burnup of ~40 GWd/MT) compares with an initial unirradiated density of 10.4 g/cm^3. Given the irradiated fuel density of 10.2 g/cm^3 and data from the LANL QA report on the non-TIGR treated fuel pellets, the pellet diameter can be estimated.

The density-based pellet diameter is 0.32785 inches (±1.1 mils). This diameter range is plotted (green symbol) in Figure 5.6 and agrees very well with the pellet diameters determined via the FPMA and MET mount measurements.

As explained previously, Figure 5.6 demonstrates the initial fuel densification. After the initial densification phase, pellet expansion (due to fuel swelling, which is directly proportional to burnup) will continue until the irradiation is stopped.

Table 5.8. Fuel Outer Diameter

Irradiation Phase	Met. Mount Ident. Number	Capsule	Fuel Pin	Fuel Pellet Outer Diameter (inches)	Uncertainty in Diameter (mils)
I	6139	1	2	0.32335	0.73
I	6140	1	2	0.32368	0.77
I	6141	1	2	0.32512	0.94
II	6143	9	12	0.32672	0.69
II	6144	9	12	0.32696	0.64
II	6145	2	5	0.32608	0.63
II	6146	2	5	0.32655	0.59
III	6161	3	6	0.32390	0.88
III	6162	3	6	0.32532	0.54
III	6163	10	13	0.32608	0.71
III	6164	10	13	0.32613	0.59
IV-Part 1	6218	4	7	0.32612	0.50
IV-Part 1	6219	4	7	0.32577	0.54
IV-Part 1	6220	4	7	0.32707	0.44
IV-Part 1	6223	13	16	0.32766	0.47
IV-Part 1	6225	13	16	0.32773	0.34

5.3 Conclusions from Dimensional Inspections of the Metallographic Mounts

Two primary conclusions can be drawn from the PIE metrological results and the dimensional inspections of the fuel pin metallographic mounts:

- Outward creep of the fuel pin Zircaloy cladding in the MOX test irradiation is conclusive. For the 30 GWd/MT withdrawal fuel pins [6 and 13, Reference 37)], the cladding diameter (at hot-cell conditions) had expanded by about 0.45 mil (an increase of 0.12%). The 40 GWd/MT withdrawal fuel pins (7 and 16) are found to be expanded by ~0.22% (or 0.84 mils).

  By contrast, the valleys along the 9- and 21-GWd/MT withdrawal fuel pin surfaces were within the as-built tolerances of the unirradiated cladding. Cladding creep must be included in the predictive analyses of the fuels codes (and especially the CARTS analyses) for higher fuel burnups (30 GWd/MT and above) for this MOX test irradiation.

- Taken literally, the data ranges corresponding to 9- and 21-GWd/MT burnups in Figures 5.6 and 5.7 might be interpreted to indicate an unexpected variation in the extent of fuel swelling. However, it is believed that the associated measurement uncertainties have been underestimated. These uncertainties will be reassessed when the PIE for the 50 GWd/MT withdrawals is undertaken. In the meantime, it has been demonstrated that with uncertainty increased to just 0.5% for these fuel pins, a smooth curve representative of the expected densification and swelling can be passed through all data ranges.

  The fuel behavior (cracking, densification and swelling) of the MOX test fuel is normal and prototypic of commercial fuel. The appropriate degree of fuel densification (corresponding

to the fuel swelling models employed by the individual calculations) is included in CARTS predictive analyses for higher burnups.

5.4 Assessment of MOX Fuel Densification and Swelling

The CARTS code employs two fuel densification and swelling models (as selected by user input):

- the first is from ESCORE (Reference 44), which is an industry-derived code approved by the US NRC,
- the second is from FRAPCON-3 (Reference 45), which is the NRC's audit code.

Both models have been used in the CARTS safety analyses conducted previously for the MOX test irradiation. The only degrees of freedom in applying these models are the amount of fuel densification and the period during which the densification occurs, both user-input.

In the 30 GWd/MT PIE Implications report (Reference 37), the CARTS code was employed in simulating the MOX test Phase I, Phase II, and Phase III irradiations. For these simulations, a fuel densification and swelling model (either ESCORE or FRAPCON) was selected and then the ultimate fuel densification and the densification period were varied until a best fit to the measured data was accomplished. For the ESCORE model, this best fit was obtained with 4.0% densification complete by 15 GWd/MT. For the FRAPCON model, the best fit was obtained with 2.0% densification complete by 10 GWd/MT.

The ESCORE fuel swelling model is different for constrained and unconstrained fuel/clad configurations; in Reference 37, this resulted in a cross-over of the predicted fuel pellet equivalent diameters for the CARTS simulations [(1) dimensions predicted for maximum initial gas gaps and (2) dimensions predicted for minimum initial gas gaps, see Figure 5.8 in Reference 37]. Given this unusual model behavior and the very high "best fit" fuel densification of 4% for the ESCORE model, the decision was made to use only the FRAPCON-3 fuel densification/swelling model in subsequent CARTS calculations. In addition, the "best fit" value of 2.0% densification (complete by 10 GWd/MT) for the FRAPCON-3 model is very reasonable with respect to the commercial LWR fuel experience (where 1–2% fuel densification is normally observed).

The data developed in Sections 5.2.4 and 5.2.5 permit a reassessment of the MOX test fuel densification, based on PIE observations, that is appropriate when applying the FRAPCON model in CARTS in describing the MOX fuel behavior. The CARTS simulations employ a model for the actual cladding creep (function of fuel type and burnup) as illustrated in Figure 5.4.

For this reassessment of the fuel densification, the CARTS code has been employed in simulating the MOX test Phase I, Phase II, Phase III, and Phase IV-Part 1 irradiations. For these simulations, only the FRAPCON-3 fuel densification and swelling model is used. The ultimate fuel densification and densification period are then varied until a best fit to the test data (i.e., Figures 5.6 and 5.7) emerges. For the FRAPCON model, the best fit value is 2.0% with densification complete by 10 GWd/MT—the same as obtained for the 30 GWd/MT withdrawals as documented in Reference 37.

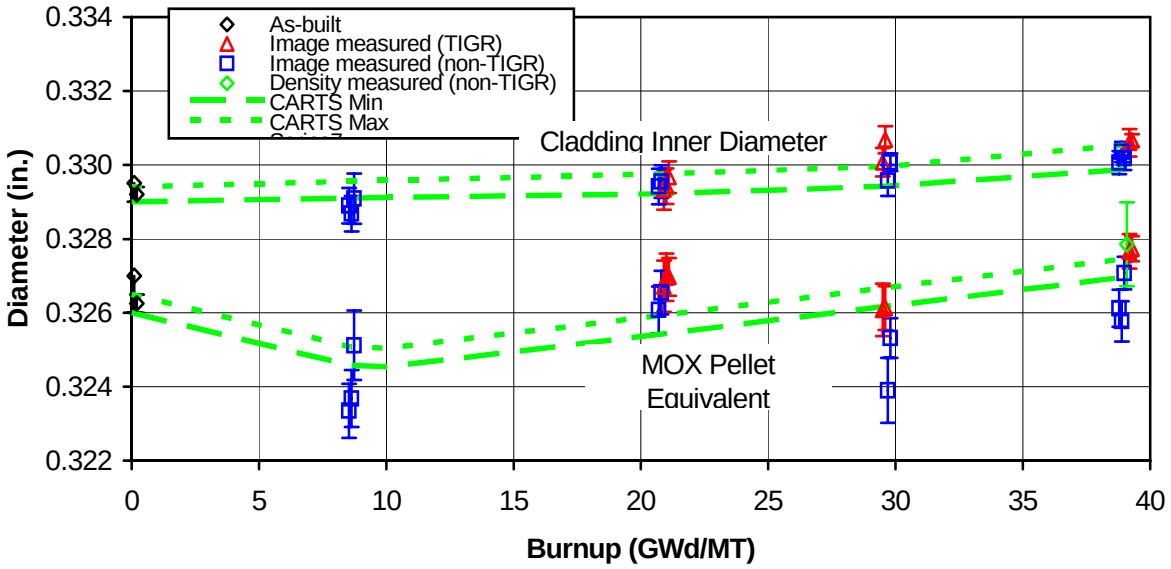

Fig. 5.8. Clad and pellet diameters vs burnup—cold dimensions. CARTS with the FRAPCON-3 swelling model: 2.0% densification ending at 10 GWd/MT.

The results of these simulations and model predictions using these values are illustrated in Figures 5.8 and 5.9. The two dashed lines represent the results of CARTS simulations employing the FRAPCON-3 fuel swelling model for minimum and maximum initial gas gaps. As shown, the predicted pellet diameters and the pellet-to-clad gaps for the two gas gap extremes are essentially parallel throughout the irradiation.

The FRAPCON-3 fuel swelling model is relatively simple in that it includes a constant swelling rate (solid fission product induced) of 0.77% per 10 GWd/MT; there are no model components for (1) gaseous fission products, (2) temperature dependence, or (3) constrained/unconstrained fuel. The FRAPCON-3 model represents a least squares fit to experimental and industrial data.

In addition to the CARTS simulations, the ORNL version of FRAPCON-3 (version 1.3, modified at ORNL for MOX usage) was executed for the MOX test Phase I, II, III, and IV-Part 1 irradiations. The FRAPCON-3 models contain 15 axial segments (one per fuel pellet) and use the axial power peaking factors (as a function of burnup) calculated by G. Chang at INEEL. The results of these FRAPCON-3 calculations are presented in Figures 5.10 and 5.11. Since the axial power in the fuel rod is determined via the mean LHGR and the axially-dependent peaking factors, the burnup of each individual pellet is different; the burnup ranges are given in Table 5.4 and illustrated in Figures 5.10 and 5.11.

The FRAPCON-3 code does not have a model for cladding creep-out, as used in CARTS; thus, as shown in the top of Figure 5.10, the inner diameter remains constant (which reduces the computed pellet-to-cladding gap as given in Figure 5.11). The FRAPCON-3 prediction of the

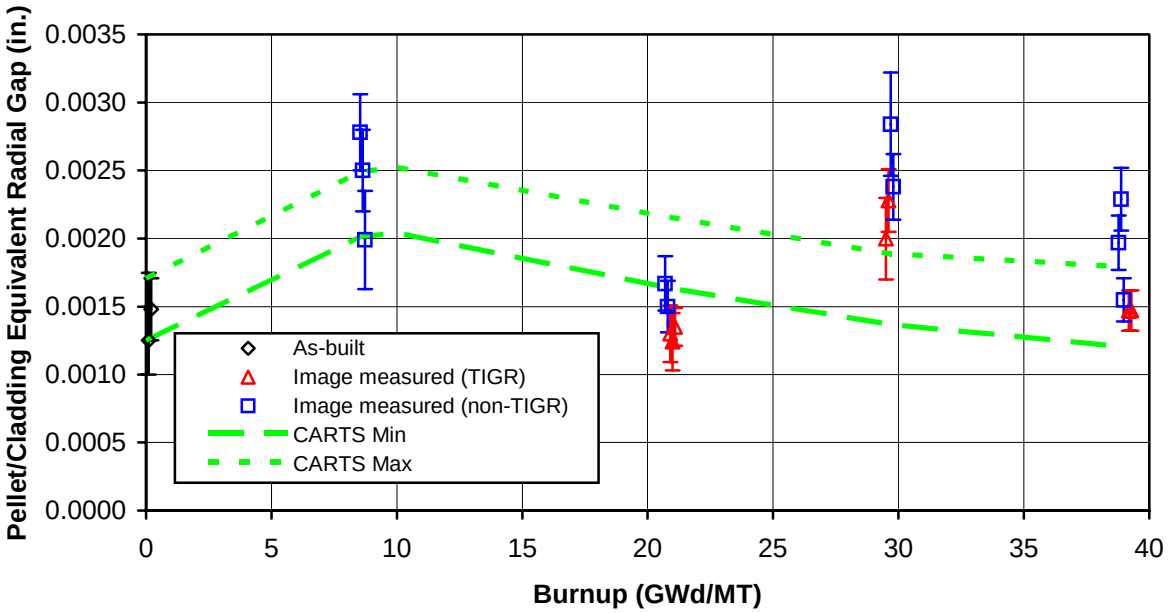

Fig. 5.9. Equivalent radial gap vs burnup—cold dimensions. CARTS with the FRAPCON-3 swelling model: 2.0% densification ending at 10 GWd/MT.

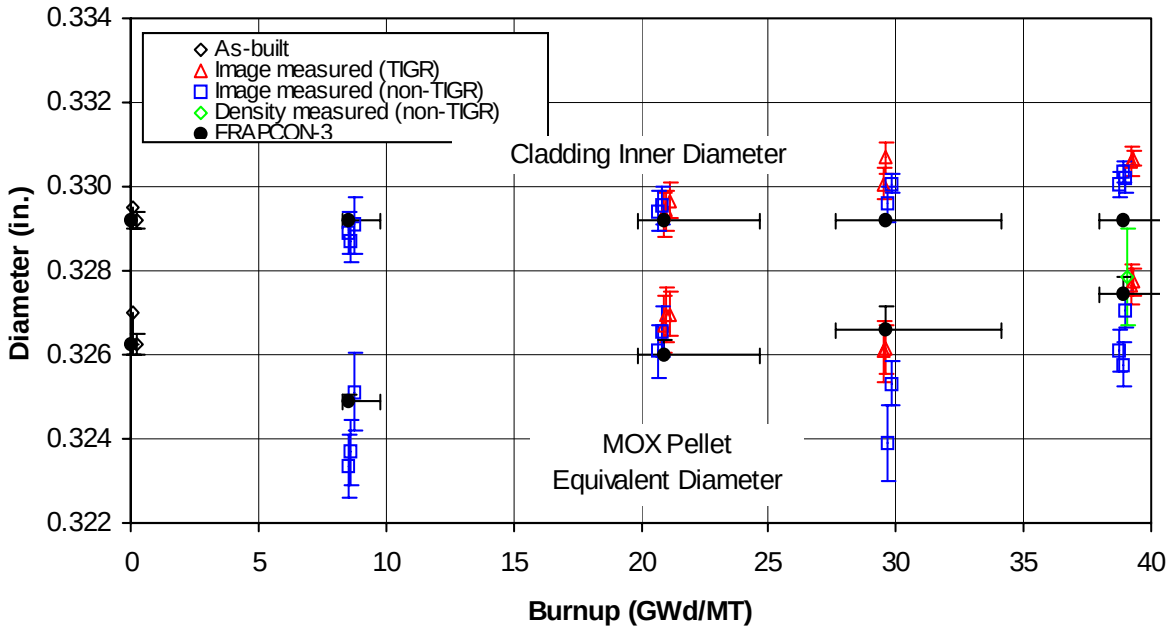

Fig. 5.10. Clad and pellet diameters vs burnup as predicted by the ORNL-modified FRAPCON-3 with 2.0% fuel densification.

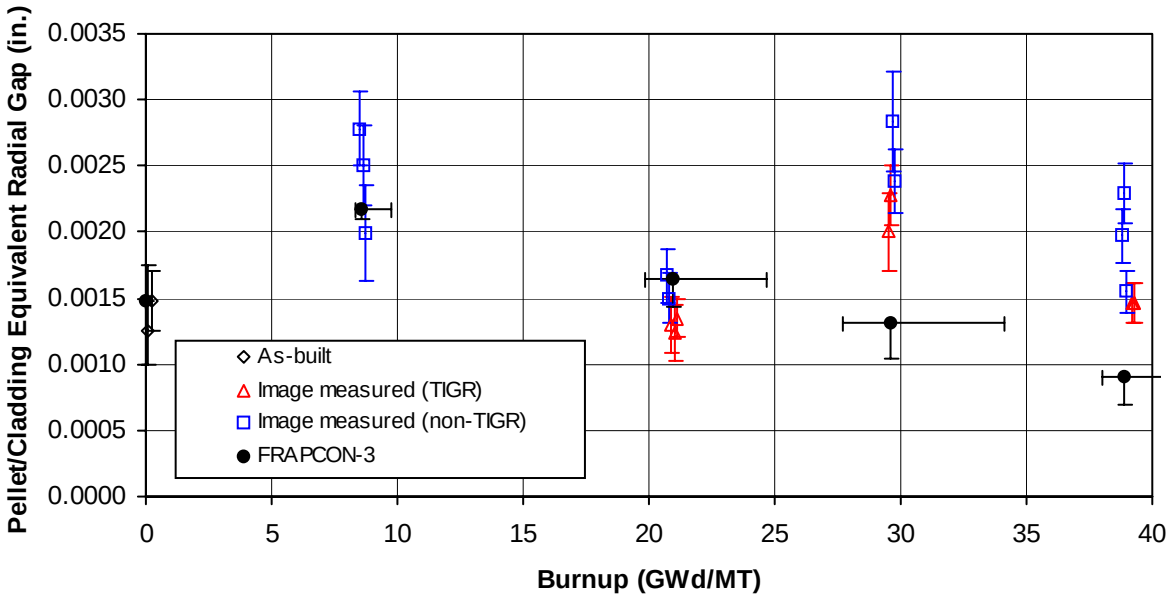

Fig. 5.11. Equivalent radial gap vs burnup as predicted by the ORNL-modified FRAPCON-3 with 2.0% fuel densification.

fuel pellet diameter (using 2.0% fuel densification) reasonably reflects the MOX test results (see bottom of Figure 5.10) and is very close to the CARTS predictions in Figure 5.8.

A comparison of the CARTS and FRAPCON-3 calculated fuel centerline temperatures for Capsule 4/Fuel Pin 7 (non-TIGR, 40 GWd/MT withdrawal capsule) is given in Figure 5.12.

In Figure 5.12, the results of four CARTS simulations are illustrated: three runs include cladding creep and differ only in the initial size of the pellet-to-cladding gaps (minimum/mean/maximum per as-built tolerances); the fourth simulation employs mean initial dimensions and does not include cladding creep. The mean with-creep and "no creep" calculated temperatures agree through the Phase II irradiation.

Deviations between the mean creep/no-creep temperatures start at about 300 reactor-days and the divergence increases through the end of irradiation. At 904 days, the no-creep simulation centerline temperature is ~120°C lower than the with-creep temperature of ~1125°C; this difference is entirely due to the better heat transfer across the smaller pellet-to-clad gas gap for the "no-creep" case (0.136 mil vs 0.334 mil).

The CARTS simulations are one-dimensional; the code uses the average LHGR for the 15-pellet stack and therefore does not recognize local variations in power due to axial peaking. The FRAPCON-3 simulations represent individual pellets and therefore do represent the axial power variation. Two FRAPCON-3 axial node centerline temperature plots are included in Figure 5.12: pellet 7 (local power below the average LHGR—Node 8) and pellet 1 [top pellet (next to gas plenum) with the highest local rod power—Node 15].

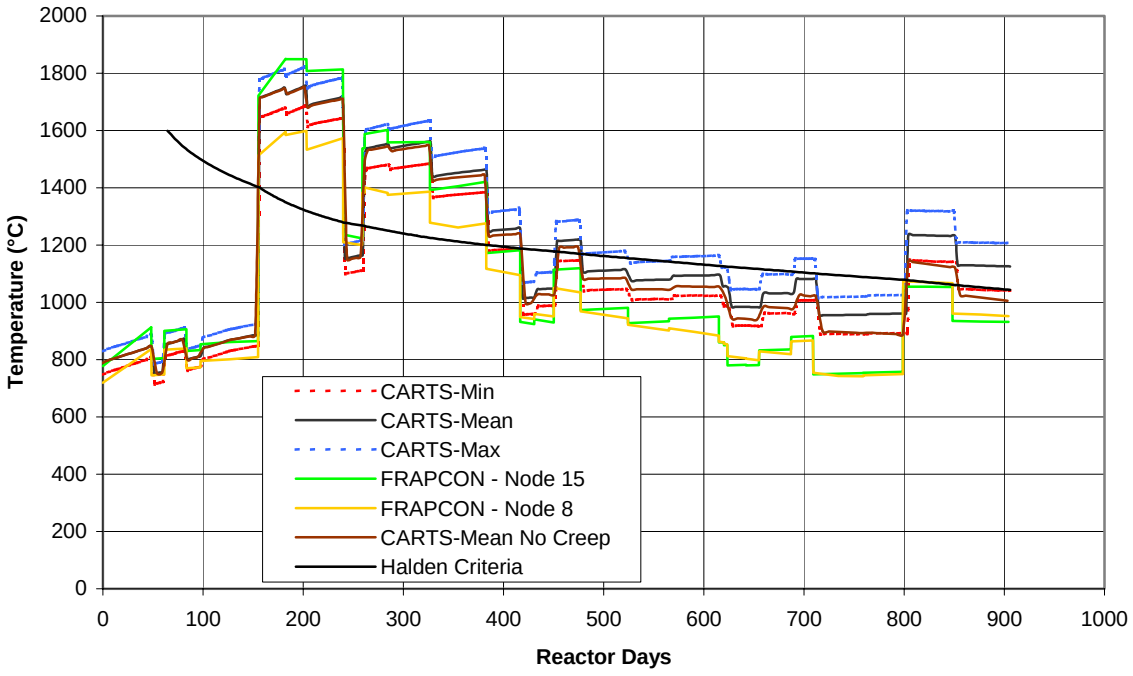

Fig. 5.12. Comparison of CARTS/FRAPCON-3 calculated centerline temperatures for Capsule 4/ Fuel Pin 7.

There is good agreement between the CARTS and FRAPCON-3 results through ~300 reactor-days. Subsequently, the FRAPCON-3 computed temperatures converge (due to reduced end peaking) and become increasingly lower than the CARTS results. These lower temperature predictions are caused by two factors: first, CARTS accounts for cladding creep outward and FRAPCON-3 does not; and, secondly, FRAPCON-3 employs a model for pellet cracking and relocation (essentially closing the pellet-to-clad gap) while CARTS does not.

Both factors yield smaller pellet-to-clad gas gaps in the FRAPCON-3 simulations after ~300 reactor-days and, as a result, lower calculated fuel centerline temperatures. The FRAPCON-3 simulations represent mean initial capsule dimensions and, at 904 days, the computed centerline temperatures are 170–190°C below the "Mean" CARTS-predicted temperature of 1125°C.

Both codes predict high centerline temperatures for the Phase II portion of the irradiation (from 155 to 383 reactor-days) except for one 19-day cycle at ~250 reactor-days. For the majority of Phase II, the predicted fuel temperatures exceed 1400°C. [There is evidence from the capsule gamma scans (Section 4.4 of Volume 1) of Cs^{137} migration within the fuel stack; this Cs^{137} migration is in itself evidence that temperatures were in excess of ~1200°C. On the other hand, the absence of columnar grains in the examined MET mounts indicates that these fuel centerline temperatures did not exceed about 1700°C.]

After ~300 reactor-days, CARTS predicts conservatively higher fuel temperatures (than FRAPCON-3) due to the combined effects of outward cladding creep representation and FRAPCON-3's fuel relocation model. Generally, for irradiation Phase III and IV-Part 1 (from 383 to 904 reactor-days), CARTS predicts fuel centerline temperatures greater than 1000°C while FRAPCON-3's centerline temperatures range from 800 to 1000°C. From the metallography of Fuel Pins 7 and 16 (Chapter 5 of Volume 1), agglomerates are now becoming visible toward the centerline of the fuel. The transformation to high-burnup-structure that makes these agglomerates readily visible requires local fuel temperatures lower than about 1000°C.

The actual fuel temperature was probably higher than the FRAPCON-3 prediction because FRAPCON-3 does not model the outward cladding creep, but the metallographic evidence (beginning emergence of central region agglomerates) indicates that the fuel temperature was not as high as predicted by CARTS. The CARTS prediction is conservatively high, because the outward movement of fuel fragments (gap closing) associated with pellet cracking is not represented. Together, the CARTS/FRAPCON-3 predictions probably bound the actual fuel temperature trace.

Also shown in Figure 5.12 are the Halden criteria for fission gas release (greater than 1%). The predicted fuel temperatures exceed the Halden threshold for nearly all of the Phase II irradiation and again just prior to withdrawal. (Temperatures may also have exceeded this threshold at several other times during the irradiation.) Thus, per the conclusions in Chapter 2, fission gas releases for Fuel Pins 7 and 16 of 8.4% and 9.5%, respectively, are reasonable, given the predicted fuel temperatures.

6. MODEL FOR OUTWARD CLADDING CREEP

6.1 Introduction

Two types of permanent deformations are observed in the MOX fuel cladding: (1) ridges located at axial positions adjacent to the pellet-to-pellet interfaces and (2) irradiation-enhanced outward creep. In Chapter 6 of the previous (30-GWd/MT PIE) implications report (Reference 37), cladding ridges were found to be caused by differential thermal expansion of the fuel pellets in the axial direction. At hot conditions during reactor operation, the MOX pellets warp into hourglass shapes, and localized contact with the cladding occurs with sufficient force to cause yielding of the cladding at locations adjacent to the pellet-to-pellet interfaces. Because of the unique design of the MOX test fuel pins with small initial gap widths between the MOX pellets and the cladding, this yielding occurs on initial heatup before initiation of any pellet densification or swelling.

The reader is invited to refer to the previous discussion in Chapter 6 of Reference 37 for further information on pellet hourglassing and the finite element (ABAQUS code) analyses performed for the pellet/cladding/capsule wall interactions. These clearly demonstrate the high cladding stresses (>yield) imposed by pellet-clad mechanical interaction at the pellet-to-pellet interfaces. Subsequent ABAQUS analyses (with component relocations associated with yielding) predicted permanent plastic deformations (ridges) overlying the pellet ends while low cladding stresses prevailed at the pellet midplane.

The other type of permanent cladding deformation, irradiation-enhanced creep, is discussed in this chapter. Because the MOX test fuel pins are contained inside of stainless steel capsules, they are exposed to low pressure on the outer surfaces of their cladding, rather than the high pressures that exist on the outside of commercial light water reactor fuel. As fuel pin internal pressures increase during the MOX test irradiations (primarily because of fission gas releases, but also enhanced by helium releases), the MOX cladding experiences small tensile hoop stresses and slow outward creep, rather than the more normal compressive hoop stresses and inward creep-down of commercial fuel. In addition to cladding hoop stresses, other parameters that affect creep rates include fast neutron flux and cladding temperatures.

The measurements and calculations performed to determine the outward creep of the MOX test cladding are presented in Section 6.2. These measurements are then compared in Section 6.3 with similar data found in the literature. Finally, an empirical cladding creep correlation for use in the CARTS code is presented in Section 6.4.

6.2 MOX Cladding Outward Creep Measurements

A summary of the measured outer diameters of the MOX test cladding has been provided in Section 5.2.3. Figure 5.2 shows an example of an outer profile measured along the length of Fuel Pin 7. This profile results from the combined effects of ridging caused by pellet hourglassing and irradiation-enhanced creep. In order to separate the amount of creep from the

ridging effects, an average value was calculated for the minimum diameters of the 15 valleys visible in the Figure 5.2 profile. The average minimum diameter of 0.38138 inches for Fuel Pin 7 is then plotted in Figure 5.4 along with diameters calculated in similar manners for the other fuel pins. Figure 5.4 therefore displays the measured cladding creep in the absence of ridging effects as a function of burnup.

One observation about Figure 5.4 is that there is negligible cladding creep at low burnup. The uncertainty bands at burnups of 8 and 21 GWd/MT overlap the uncertainty band associated with the drawing and as-built tolerances at zero burnup. A second observation about Figure 5.4 is that the fuel pins with TIGR-treated pellets undergo more cladding creep than the non-TIGR fuel pins. This second observation is consistent with the measured fission gas release ranges and fuel pin internal pressures presented in Table 2.4. At each burnup level in Table 2.4, the fission gas releases and internal pressures are greater for the TIGR-treated fuel (Fuel Pins 12, 13, and 16) than for the non-TIGR fuel. The higher internal pressures generate higher tensile hoop stresses in the cladding, which increases the outward cladding creep.

Traditional creep theory splits the process into the two stages illustrated in Figure 6.1: an initial period with a rapid (but declining) creep rate (called primary creep) followed by a second period with a lower constant creep rate (called secondary creep). For cladding that is exposed to a constant hoop stress, the inelastic creep strain ε as a function of exposure time t is typically expressed with the following equation:

$$\varepsilon = \varepsilon_p\left(1 - e^{-a\,t}\right) + \dot{\varepsilon}_s\, t \tag{6-1}$$

where ε_p is the total primary strain, $\dot{\varepsilon}_s$ is the constant secondary strain rate, and a is a decay constant.

Special treatment is necessary for applying Equation 6-1 to the MOX cladding measurements (discussed at the beginning of this section) because the fuel pin internal pressures P_{fp} and associated cladding hoop stresses S_h increase during the MOX test irradiations, and these stresses are not measured at the hot conditions during reactor operation. First, the CARTS code

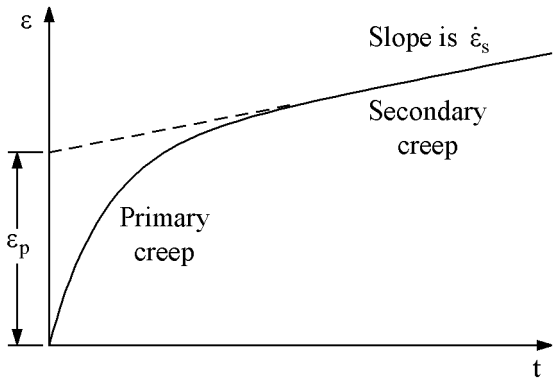

Fig. 6.1. Illustration of traditional creep theory with process divided into primary and secondary creep regions.

is used to estimated the cladding hoop stresses as a functions of exposure time during the irradiations using the following equation:

$$S_h = \frac{P_{fp}\,ID - P_c\,OD}{OD - ID} \tag{6-2}$$

where P_c is the capsule internal pressure and ID and OD are the inner and outer cladding diameters, respectively. The CARTS calculations are described in Section 5.4; the predicted results used for this creep analysis are those representing the mean initial gas gap widths. Other relevant input parameters for the individual CARTS calculations were selected such that the predicted results best match the fission gas releases and fuel pin pressures measured in the ORNL hot cell after completion of the irradiations.

Then Equation 6-1 is converted into a special form by combining the effects of cladding hoop stress and exposure time together into a "cumulative cladding stress × exposure product" y as follows:

$$y = \int_0^t S_h\,dt \tag{6-3}$$

$$\varepsilon = \varepsilon_p\left(1 - e^{-b\,y}\right) + c\,y \tag{6-4}$$

where b and c are similar to a and $\dot{\varepsilon}_s$ in Equation 6-1, but have different units.

The fuel pin and capsule internal pressures predicted by CARTS for Fuel Pin 7 are shown in Figure 6.2, and the associated cladding hoop stresses (calculated from Equation 6-2) are shown in Figure 6.3 as functions of effective-full-power exposure time. Although the CARTS code does not represent the fuel pin conditions during the refueling outages (which is why both curves are smoothly increasing), it does predict the conditions when measurements are made in the ORNL hot cell after completion of the irradiations. The CARTS-predicted fuel pin internal pressures in Figure 6.2 reach a maximum of 152.9 psia, before falling to a final value of 114.9 psia in the hot cell, which agrees well with the measured value of 114.8 psia for Fuel Pin 7 in Table 2.4. The cladding hoop stresses in Figure 6.3 reach a maximum tensile value of 6.19 MPa.

When Equation 6-3 is applied to Figure 6.3, a cumulative cladding stress × exposure product of 1885 MPa•day is calculated for Fuel Pin 7, which represents the area under the curve in Figure 6.3. Similar CARTS calculations were performed for Fuel Pins 5, 6, 12, 13, and 16, and values for the cumulative cladding stress × exposure products are listed in Table 6.1. Table 6.1 also lists the cladding inelastic hoop strains calculated from the measured minimum outer diameters shown in Figure 5.4. When the last two columns of Table 6.1 are plotted in Figure 6.4, they begin to resemble the shape of the curve in Figure 6.1.

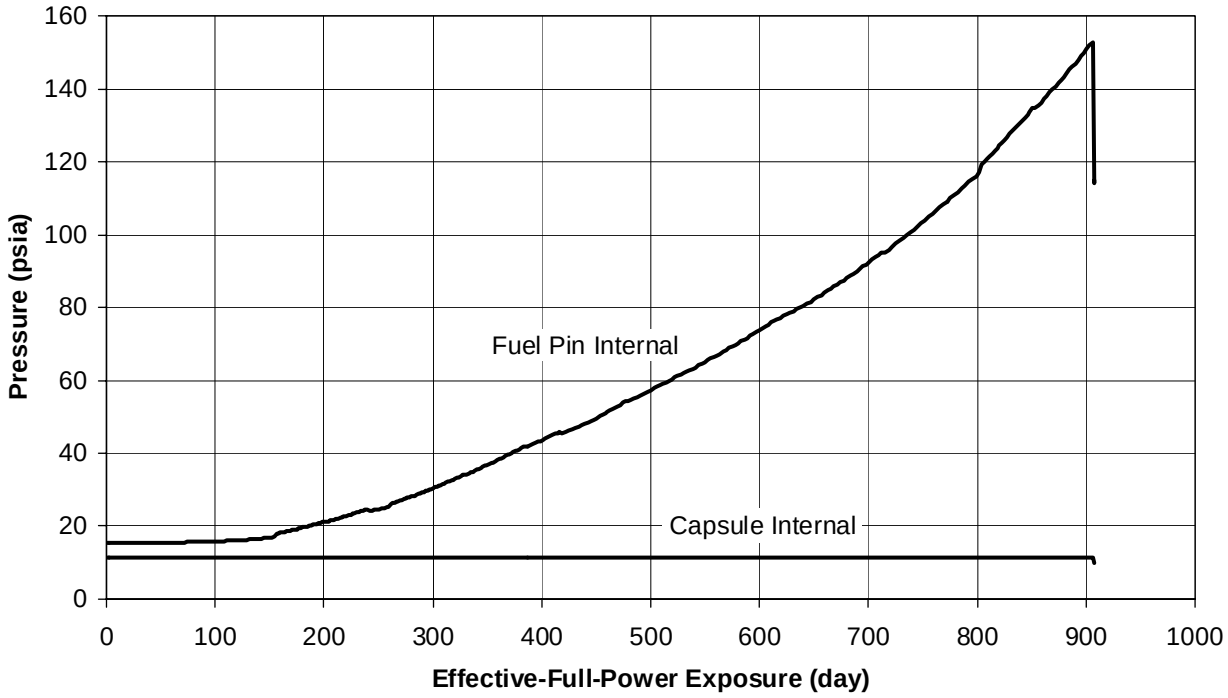

Fig. 6.2. Fuel pin and capsule internal pressures predicted by CARTS for Fuel Pin 7.

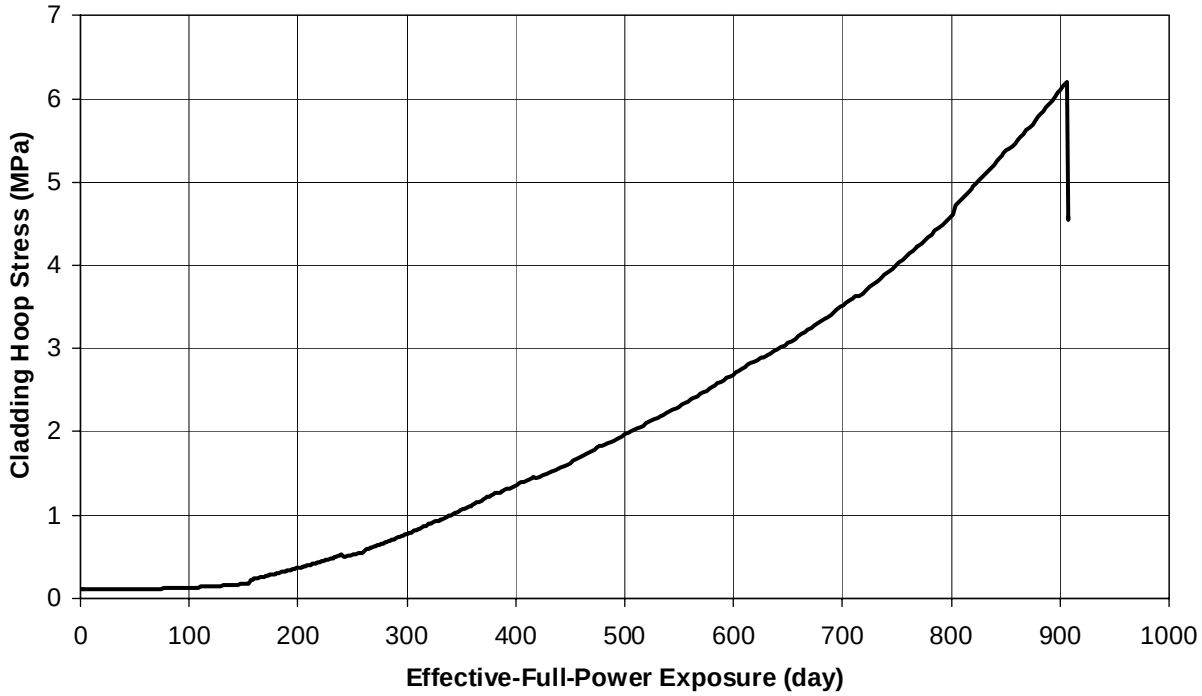

Fig. 6.3. Cladding hoop stresses (tensile) predicted by CARTS for Fuel Pin 7.

Table 6.1. MOX Test Cladding Stress and Strain Parameters

Fuel Pin No.	Total Exposure (Effective-Full-Power Days)	Max. Cladding Hoop Stress (MPa)	Cumulative Cladding Stress × Exposure Product (MPa•day)	Cladding Inelastic Hoop Strain
5	384	0.66	114	0.000102
12	384	0.86	137	0.000441
6	629	1.01	276	0.000775
13	617	1.40	351	0.001109
7	908	6.19	1885	0.001907
16	908	7.37	2132	0.002527

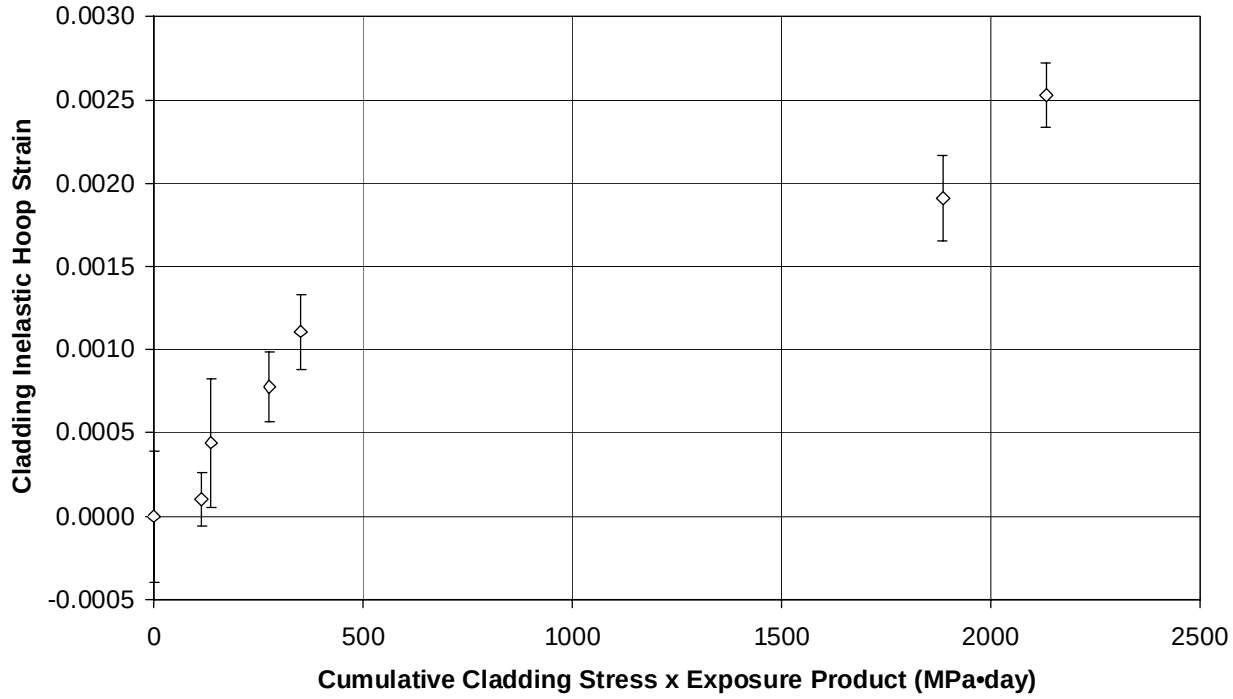

Fig. 6.4. MOX test cladding outward creep with error bars indicating measurement uncertainties.

6.3 Outward Creep Data Found in Literature

Limited creep data are available in the literature for cladding with tensile (rather than compressive) hoop stresses caused by high internal pressures. Other factors that also have a significant impact on cladding creep include (1) fast neutron flux, (2) cladding temperature, and (3) the type and initial state of the cladding (pre-irradiated, stress relieved, etc.). The MOX test cladding is fresh (not previously irradiated), stress-relieved annealed (SRA) Zircaloy-4. During

the MOX fuel irradiations, cladding temperatures range from 200 to 400 °C and fast neutron fluxes are about $2(10)^{13}$ neutron/(cm^2•s).

Three sources of outward creep data were located for cladding and operating conditions similar to the MOX test irradiations. Reference 47 provides creep data measured in a dedicated test rig in the Halden Reactor in Norway. Of particular interest is Figure 6 in Reference 47, which is for fresh SRA Zircaloy-4 cladding irradiated at a constant tensile hoop stress of 52 MPa for an exposure time of 208 effective-full-power days. Other relevant Halden parameters are a cladding temperature of 375°C and a fast neutron flux of $4.3(10)^{13}$ neutron/(cm^2•s). Figure 6 in Reference 47 also provides a curve fit of the creep data in the form of Equation 6-1. This curve fit was converted into the form of Equation 6-4 (using Equation 6-3), and the Halden data is plotted in Figure 6.5 along with the MOX test cladding data from Figure 6.4. Although there is a large difference in the hoop stresses associated with the Halden data (52 MPa) and the MOX data (<7.4 MPa), the use of the cumulative cladding stress × exposure product appears to provide a good way for correlating the creep strains.

Reference 48 by Soniak et al. contains outward creep data measured at the SILOE Test Reactor in France for SRA low-tin Zircaloy-4 cladding exposed to constant tensile hoop stresses ranging

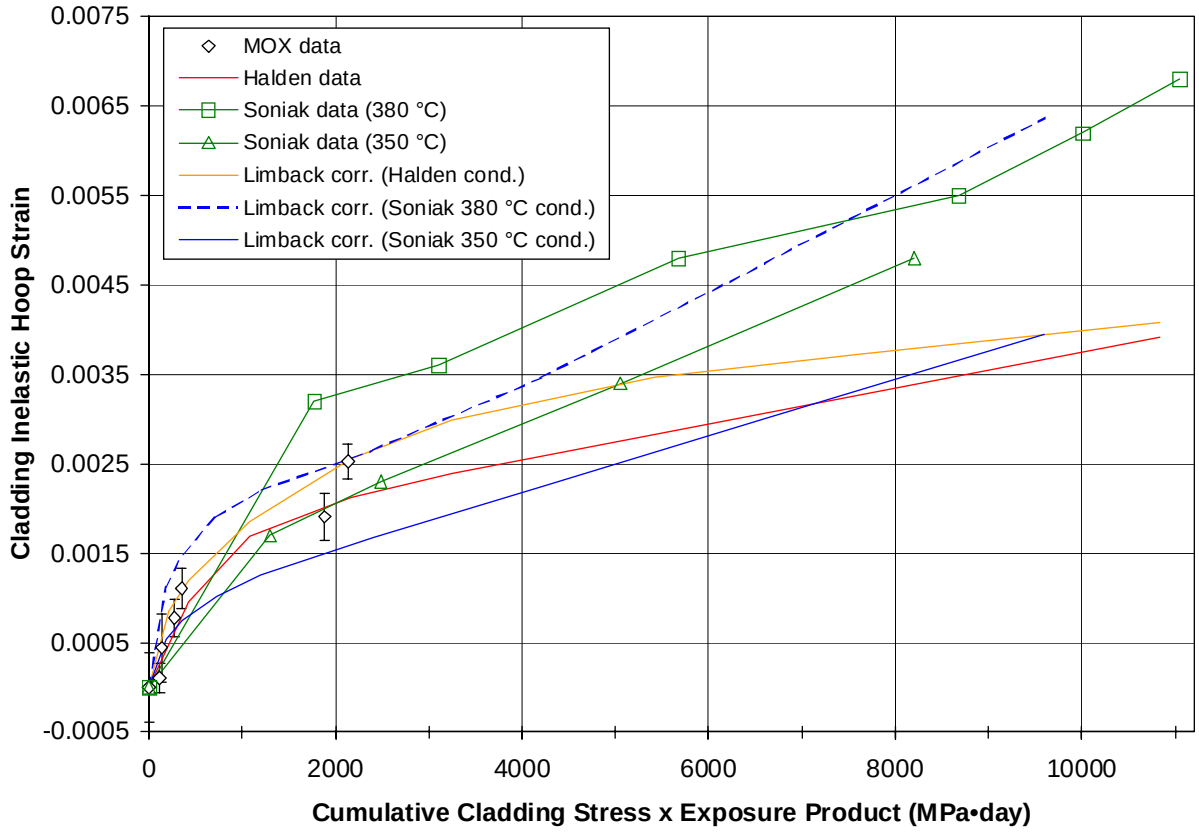

Fig. 6.5. Comparison of MOX test measurements with other outward creep data for SRA Zircaloy-4 claddings.

from 60 to 120 MPa. Two of the 60-MPa-stress datasets were selected for comparison with the measured MOX cladding outward creep. The first Soniak et al. dataset is for a cladding temperature of 380°C and a fast neutron flux of $2.08(10)^{14}$ neutron/(cm^2•s); the other dataset is for a cladding temperature of 350°C and a fast neutron flux of $1.65(10)^{14}$ neutron/(cm^2•s). The relevant creep data was obtained from Figure 4 of Reference 48, and then converted into a format suitable for plotting with the other data in Figure 6.5. Although the lowest-exposure points of the Soniak et al. data only overlap the highest-exposure points of the MOX test data, the Soniak et al. data for the 350°C cladding temperature appears to be in better agreement with the MOX data.

A detailed correlation for outward cladding creep is presented by Limback and Andersson in Reference 49. This correlation was calibrated against an extensive series of thermal and in-reactor creep tests for both Zircaloy-2 and Zircaloy-4 claddings. This Limback/Andersson correlation has been used (with proper SRA Zircaloy-4 input parameters) to calculate cladding creep strains for the Halden and Soniak et al. test conditions (cladding hoop stress, temperature, and fast neutron flux) described in the preceding paragraphs. The predicted results from the Limback/Andersson correlation are plotted in Figure 6.5, and generally good agreement is observed with the respective test data. Note that the Limback/Andersson correlation could not be directly applied for the MOX test conditions because the low cladding hoop stresses (<7.4 MPa) are below the range for which the correlation was calibrated.

6.4 CARTS Outward Creep Empirical Correlation

Figure 6.5 provides strong evidence that Equations 6-3 and 6-4 can be used to accurately represent the cladding outward creep that occurs during the MOX test irradiations. The MOX data points are located in the primary creep region, except for the two points for burnups of 40 GWd/MT, which appear to be near the transition between the primary and secondary creep regions.

An empirical correlation based upon Equation 6-4 that fits the MOX test outward creep data is:

$$\varepsilon = 0.0018\left(1 - e^{-0.00181\,y}\right) + 2.5(10)^{-7}\,y \qquad (6\text{-}5)$$

where the inelastic creep strain is unitless and y is the cumulative cladding stress × exposure product (defined in Equation 6-3) with units of MPa•day. Figure 6.6 illustrates the Equation 6-5 empirical correlation and also shows the MOX test and other experimental data in greater detail for the low exposures. The secondary strain rate of $2.5(10)^{-7}$ in Equation 6-5 was selected to best represent the slope of the experimental data above 3000 MPa•day. The other parameters of Equation 6-5 were determined to best fit the MOX test data points.

This empirical correlation applies for limited conditions: SRA Zircaloy-4, tensile hoop stresses, and cladding temperatures and fast neutron fluxes similar to the MOX irradiation conditions. Also, because the time-dependent cladding hoop stresses upon which the correlation is based were estimated from CARTS code calculations (e.g., Figure 6.3), this correlation is only considered applicable for use within CARTS. It will be employed for the Pre-PIE predictions for the next set of capsules, to be withdrawn at 50 GWd/MT.

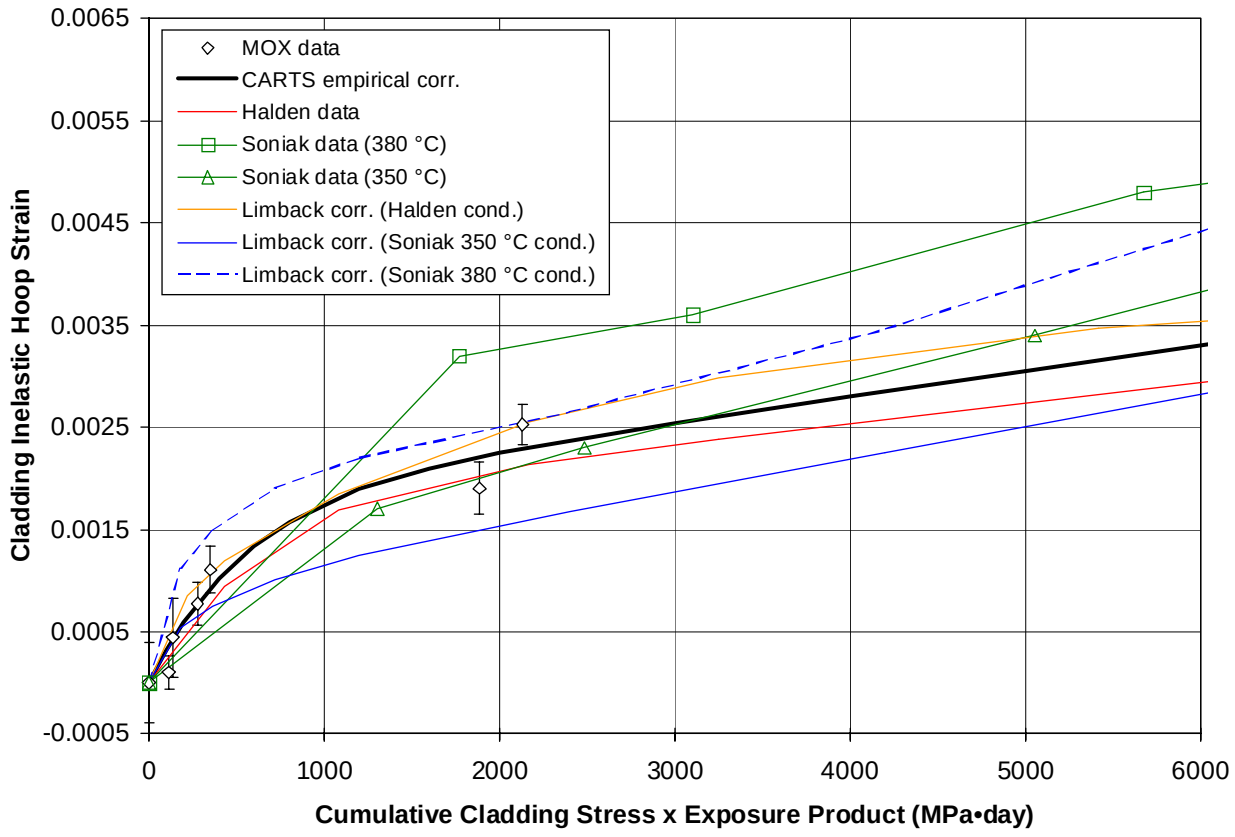

Fig. 6.6. Empirical correlation used in CARTS code for MOX test cladding outward creep.

7. POST-PIE CARTS CALCULATIONS OF CAPSULES 4 AND 13 IRRADIATION RESPONSE

7.1 Introduction

The CARTS calculations for Capsules 4 and 13 presented in Chapter 2 of the 40 GWd/MT Quick Look Report (Reference 50) were performed in advance of the PIE. Given the re-assessment of the MOX fuel densification and swelling through an approximate burnup of 40 GWd/MT presented in Section 5.4, the degree of cladding creep discussed in Section 5.2, and various CARTS code improvements, it is desirable to determine the extent to which these modeling changes (fuel densification, length of densification period, cladding creep during irradiation, etc.) affect the predicted behavior of Capsules 4 and 13. These post-PIE CARTS analyses are presented in this Section, together with a comparison to the earlier predictions.

The CARTS calculations predict the conditions at the pellet midplane as a function of increasing burnup, and do not include representation of pellet cracking and relocation, or pellet end-effects such as hourglassing.

7.2 Differences in Pre- and Post-PIE CARTS Modeling Assumptions

The cold, un-irradiated capsule and fuel pin dimensions employed in the Reference 50 analyses and in this Chapter are based on the as-built component dimensional ranges given in Table 5.2.

The irradiation histories for Capsules 4 and 13 were provided in Sections 2.1 to 2.4 of Reference 50; the final version of the irradiation histories is given in Sections 3.1 to 3.4 of Volume 1 (Reference 39). The only differences in these histories are the LHGRs of the last six ATR cycles in Phase IV-Part 1, for which final values were received after the Quick Look Report had been issued. The adjustment in the LHGRs for cycle 125A(2) is about 4.6% and, for the remaining five cycles, the adjustments are less than 1.7%.

As noted in Chapter 6, cladding creep (outward) is occurring during the MOX test irradiation. For the pre-PIE analyses, the assumed creep-out of the cladding was linear [a numerical fit to the fuel pin "average" outer diameters (for data through 30 GWd/MT), as shown in Figure 5.2 of Reference 37]. The post-PIE CARTS calculations directly represent the cladding "valleys" as functions of fuel type and burnup, as depicted in Figure 5.4. As shown in Figure 6.6, these points are the bases for the empirical correlation (Equation 6-5) that will be employed for the next (50 GWd/MT) set of pre-PIE calculations.

The post-PIE creep models predict greater cladding expansion than the pre-PIE linear formulation; thus, there is potential for the width of the predicted pellet-to-clad gas gaps to increase, with a concomitant increase in fuel temperatures due to lower gap conductances.

CARTS modeling of fuel densification requires user-input of the degree of densification, and the length of the densification period. The pre-PIE parameters are based on the assessment given in Section 5.3 of Reference 37 while the post-PIE parameters are based on the re-assessment given

in Section 5.4 of this report. It develops that these densification parameters are the same for both the pre- and post-PIE CARTS calculations, as follows:

- FRAPCON-based models: a maximum of 2% fuel densification achieved during the period of 0–10 GWd/MT burnup.

The cumulative fission gas release affects the gap conductance throughout the CARTS calculation and is controlled via a code input parameter specifying the percent released at 45 GWd/MT. The two values considered for the pre-PIE analyses are defined from the European MOX experience as best-estimate (4.2%) and conservative as determined by maximum LHGR (16.5% for Capsule 4 and 16.9% for Capsule 13).

The fission gas release percentages employed in the post-PIE calculations for Capsules 4 and 13 correspond to the PIE-measured 8.37% and 9.51%, respectively, at 40 GWd/MT (see Table 2.1).

Both the pre- and post-PIE calculations use the Duriez model for MOX thermal conductivity, but the post-PIE analyses also employ a model for the thermal conductivity burnup degradation and high temperature behavior (Reference 51, modification introduced by FRAPCON staff at PNNL). This new model yields lower fuel thermal conductivity for the same temperature and burnup than the pre-PIE degradation model; therefore, given the same LHGR and burnup, the fuel temperatures will be higher.

The Halden fission gas release threshold criterion (Reference 16) cited in the Quick Look report (Reference 50) dates to 1979. An improved version (Reference 17) of the Halden criterion, issued in 2003 and applicable for high burnups, has been employed in Chapter 5 and in these post-PIE CARTS calculations.

Other than these noted differences, all CARTS code input and models for the pre- and post-PIE calculations are the same.

7.3 CARTS Post-PIE Results for Capsule Conditions During the Irradiation

Each capsule surrounds a fuel pin containing 15 MOX pellets. Each pellet has unique dimensions within the specified fabrication tolerances, so that a spectrum of initial pellet-to-clad gaps exists within each fuel pin. In the following discussions, results are reported for the minimum, mean, and maximum initial gap widths as defined by the measured as-built fuel pin inner diameter and the as-built tolerance range for pellet outer diameter as listed in Table 5.2. Pre-PIE CARTS calculated results are italicized in parenthesis for comparison purposes.

7.3.1 Results for Capsule 4

Figure 7.1 illustrates the cycle-by-cycle LHGRs as calculated by the MCNP code for Capsule 4, with the corresponding CARTS predictions of pellet mean and centerline temperatures and variations in pellet-clad diametral gap. These parameters are plotted against the integrated

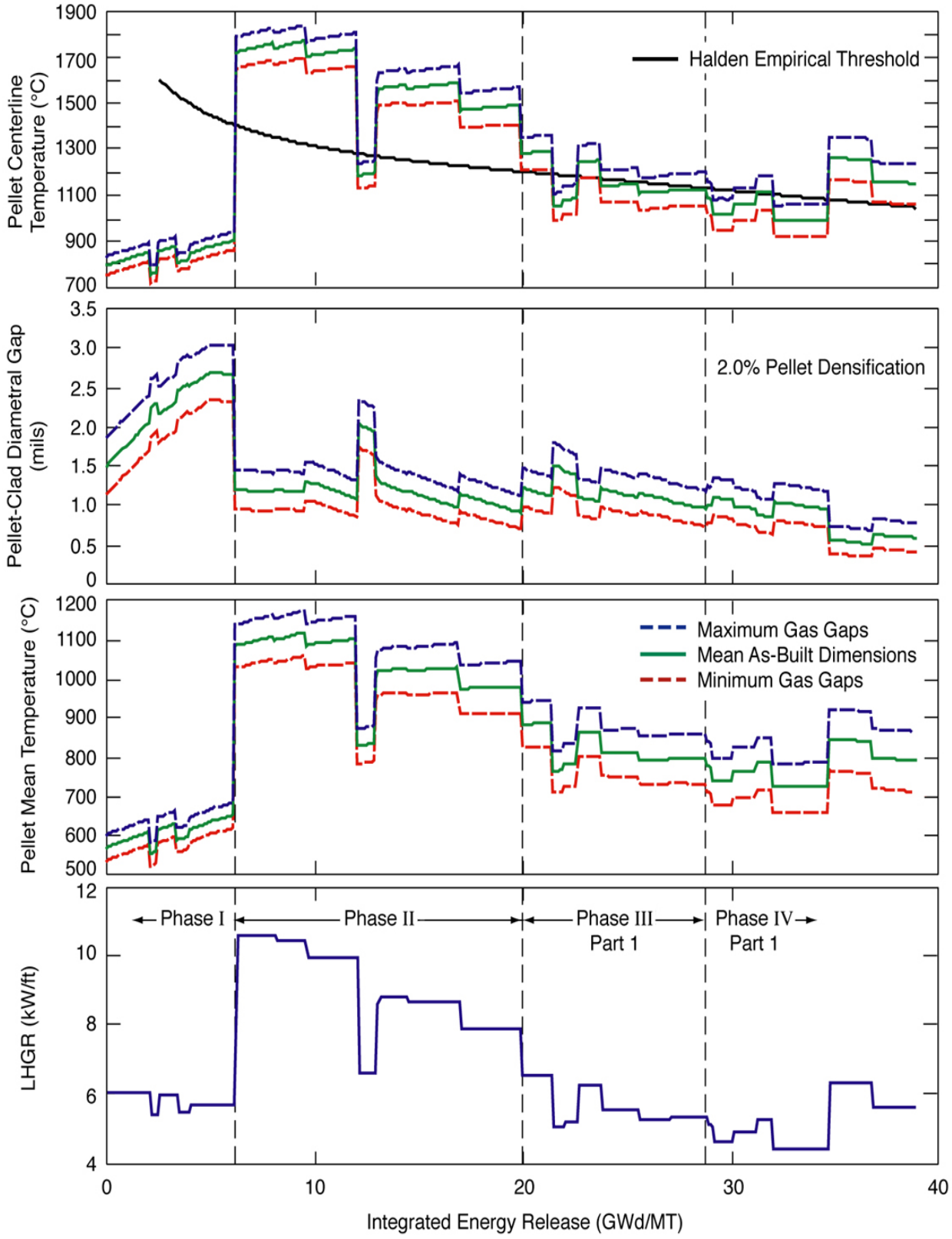

Fig. 7.1. CARTS post-PIE predictions for Capsule 4. Individual traces show results for maximum, mean, and minimum initial pellet-clad and clad-capsule gap widths.

internal energy release per unit heavy metal mass. The integrated energy release within the fuel includes power contributions other than fission (such as gamma heating by the ATR core) and thereby differs slightly from fuel burnup. In the interest of avoiding unnecessary clutter, the LHGR trace does not include spikes to near zero to mark the between-cycle reactor outages.

Three traces are shown in each of the temperature and diametral gap plots, illustrating results as calculated for minimum, mean, and maximum initial pellet-to-clad gap widths. As indicated, the diametral gap is predicted to have remained open throughout the irradiation, with a closest approach to closure (for the case of minimum initial gap) of about 0.47 (*0.52*) mil near the end of Phase IV Part 1.

Unless otherwise stated, the following discussion will reflect the mean-value traces as shown in Figure 7.1. The ranges between the minimum and maximum traces on the temperature and diametral gap plots indicate the variations associated with pellet-specific differences in the initial pellet-clad gap width.

With pellet densification of 2.0 percent completed before burnup reaches 10.0 GWd/MT, the pellet diameter initially decreases and remains smaller than its initial value throughout Phase I. This pellet shrinkage combined with outward cladding creep causes the predicted pellet-clad diametral gap to almost double [from 1.49 to 2.72 *(2.83*) mils) during this period.

The highest LHGR experienced by Capsule 4 (10.64 kW/ft) was imposed at the beginning of Phase II. As indicated in Figure 7.1, the accompanying increase in pellet thermal expansion due to high fuel temperatures [1775 (*1515*) °C] causes the pellet-clad gap to narrow to 1.23 (*1.60*) mils. Reduced LHGRs during the subsequent cycles lower the pellet temperature with corresponding reductions in thermal expansion that tend to increase the pellet-clad gap. This trend is countered, however, by monotonically increasing fuel swelling as burnup accumulates.

In the pre-PIE calculations, the gap width remained greater than its initial value until near the end of Phase III Part 1 (integrated energy release 27.2 GWd/MT). In the post-PIE simulations (Figure 7.1), the higher predicted fuel temperatures (by 160–270°C from the start of Phase II to the end of the irradiation) cause an increased thermal expansion of the fuel. Since the cladding temperature is determined by the coolant temperature and therefore is virtually the same for both the pre- and post-PIE calculations (thus the same thermal expansion), the pellet-to-clad gap is smaller for the post-PIE calculation. As shown in Figure 7.1, the gap width drops below the BOL gap at the beginning of Phase II and (except for one ATR cycle) remains below the BOL gap through the end of the irradiation.

The increased LHGRs during the last two cycles of Phase IV Part 1 were attained by the shift of the test assembly to the Southwest I-hole. The higher fuel temperatures and fuel thermal expansion during these cycles reduced the calculated gap width to its smallest value during the irradiation.

As shown in Figure 7.1, the calculated pellet temperatures increase during periods while the LHGR remains constant during the Phase I, II, and III irradiation cycles. This reflects (1) the decreases in gap thermal conductance that accompany both an increasing gap width and the

increasing inventories of low-conductivity fission gases and (2) the degradation of the fuel thermal conductivity with increasing burnup. The opposite (temperature decrease with shrinking gap under constant LHGR) occurs during the last two cycles of Phase IV Part 1.

The predicted temperatures are consistently higher for the calculation based on maximum initial pellet–clad gaps. This follows from the lower effective thermal conductance associated with wider gaps. Figure 7.1 shows that the highest predicted pellet centerline temperature [1841 (*1576*) °C] occurs at the end of the second irradiation cycle of Phase II (9.5 GWd/MT). Since this is more than 700°C below the melting temperature of the MOX fuel, there is no concern for the possibility of fuel melting.

No contact between fuel pin and capsule is predicted at any time during the irradiation.

These CARTS calculations have been compared with FRAPCON-3 simulations for Capsule 4 in Section 5.4 (Figure 5.12). There is good agreement between the predictions of CARTS and FRAPCON-3 through ~300 reactor days (a burnup of ~16 GWd/MT); thereafter, FRAPCON-3 predictions are generally lower than CARTS (by 170–190°C at the end of the irradiation). Together, the CARTS/FRAPCON-3 predictions probably bound the actual fuel temperature.

7.3.2 Results for Capsule 13

Previous PIE reports have presented irradiation histories as obtained from a single set of CARTS calculations based on the average LHGRs for the two capsules irradiated in symmetric positions. Capsules 4 and 13 were also irradiated in symmetric positions, but have been represented by independent CARTS calculations with separate input data sets based on the specific (measured) fuel pin and capsule dimensions and the individual LHGRs as calculated by the MCNP code at INEEL. Capsule 13 contains TIGR-treated fuel. The differences in the irradiation histories for Capsules 4 and 13 are small.

Figure 7.2 illustrates the cycle-by-cycle LHGRs as calculated by the MCNP code for Capsule 13, with the corresponding CARTS predictions of pellet mean and centerline temperatures and variations in pellet-clad diametral gap. These parameters are plotted against the integrated internal energy release per unit heavy metal mass.

Three traces are shown in each of the temperature and diametral gap plots, illustrating results as calculated for minimum, mean, and maximum initial pellet-to-clad gap widths

The irradiation behavior of Capsule 13 (predicted by CARTS) is very similar to that illustrated in Figure 7.1 and discussed in Section 7.3.1 for Capsule 4.

The highest LHGR experienced by Capsule 13 (10.75 kW/ft) was imposed at the beginning of Phase II. The increased LHGRs during the last two cycles of Phase IV Part 1 are due to the shift of the test assembly to the Southwest I-hole.

No contact between fuel pin and capsule is predicted at any time during the irradiation.

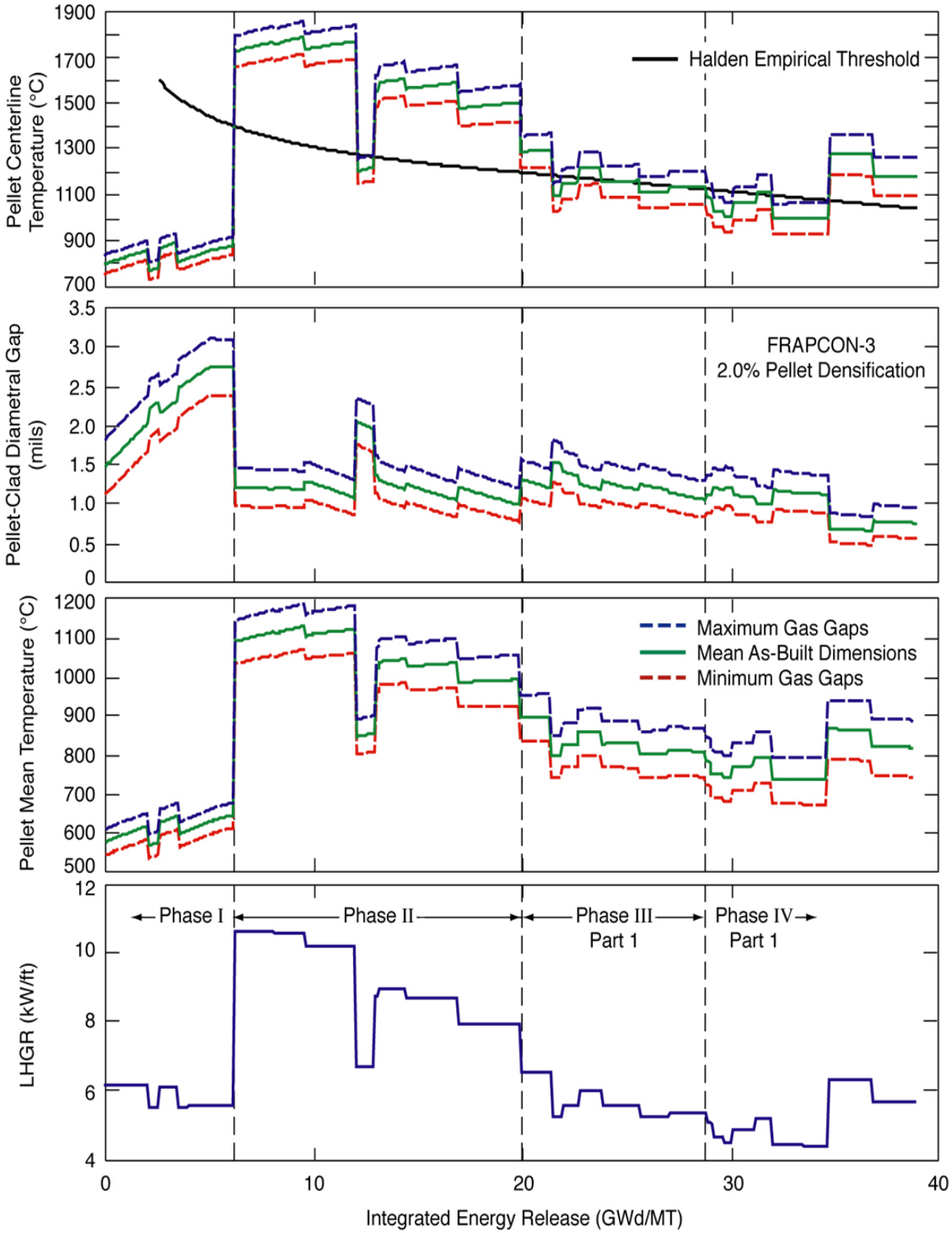

Fig. 7.2. CARTS post-PIE predictions for Capsule 13. Individual traces show results for maximum, mean, and minimum initial pellet-clad and clad-capsule gap widths.

7.3.3 In-Reactor Conditions at the End of Phase IV Part 1

Table 7.1 presents the results of the CARTS calculations for capsule conditions just prior to completion of the Phase IV Part 1 irradiation and withdrawal of Capsules 4 and 13 for PIE. Fuel burnup at this time was about 39.9 GWd/MT. As indicated in the last column of Table 7.1, none of these calculations predicts clad contact at the pellet midplane any time during the irradiation. Pre-PIE CARTS calculated results are given in red for comparison purposes.

Table 7.1. Results of CARTS calculations for Capsules 4 and 13 just prior to the end of Phase IV-Part 1

Capsule	Initial Pellet-Clad Clad-Capsule Gaps	Temperatures °C				Diametral Gap (mil)		Pellet-Clad Contact During Irradiation
		Pellet Centerline	Pellet Mean	Clad Wall	Capsule Wall	Pellet-to-Clad	Clad-to-Capsule	
4	Minimum	1040 884	697 613	217 219	98.1 97.7	0.47 0.51	1.53 1.79	Never
	Maximum	1206 1014	841 733	245 247	98.0 97.6	0.87 1.02	2.28 2.54	Never
13	Minimum	1090 896	739 619	209 222	98.5 98.3	0.58 0.50	1.27 1.79	Never
	Maximum	1255 1028	882 740	238 250	98.4 98.2	0.98 1.00	2.02 2.54	Never

As noted in Section 7.2, the post-PIE CARTS calculations use LHGRs for Cycle 127A (the last ATR irradiation cycle in Phase IV-Part 1) that are slightly higher than the pre-PIE simulations (~1.2% for Capsule 4 and ~0.7% for Capsule 13). Thus, the post-PIE calculated capsule wall temperatures are slightly higher than the pre-PIE calculated wall temperatures.

Although the calculated mean capsule wall temperature is virtually independent of assumptions with respect to the initial pellet-clad and clad-capsule gap widths, the calculated mean cladding temperature is higher for the pellets with maximum initial gaps. During reactor operation at the end of Phase IV Part 1, the temperature (about 240–250°C) of the cladding surrounding these pellets is much higher than that (about 98°C) of the capsule wall, where temperature is controlled by forced convection to the coolant flow at the outer surface.

Pre-PIE CARTS simulations employed a linear formulation for the cladding creep with no distinction between the TIGR- and non-TIGR-treated fuels; thus, the predicted diametral gas gaps for both Capsules 4 and 13 were approximately equal. The post-PIE calculations, however, use empirical models that replicate Figure 5.4 and differ for Capsule 4/Fuel Pin 7 (non-TIGR fuel) and Capsule 13/Fuel Pin 16 (TIGR-fuel). The creep for Fuel Pin 16 is greater than for Fuel Pin 7 and this difference is reflected in the end-state pellet-to-clad gaps. Also, the greater cladding creep yields smaller clad-to-capsule gaps.

As discussed in Section 7.2, the post-PIE CARTS calculations also employ a new MOX fuel thermal conductivity correlation (Reference 51) that yields a lower fuel thermal conductivity for the same fuel temperature and burnup. This model change produces the most significant differences (higher predicted fuel temperatures) between the pre- and post-PIE calculations. Even though there is greater predicted cladding creep in the post-PIE calculations, the higher fuel

temperatures result in greater fuel thermal expansion - offsetting the higher cladding creep and yielding pellet-to-clad gaps that are nearly the same as those predicted by the pre-PIE calculations.

Fuel thermal expansion and swelling are significant. Nevertheless, with fuel densification of 2.0 percent, clad contact is not predicted at the pellet midplane. As indicated in Table 7.1, the minimum pellet-to-clad diametral gap just prior to reactor shutdown from Cycle 127A is calculated to be about 0.47 mil.

For pellets with maximum initial gaps, Table 7.1 indicates the expected larger (≥0.87 mil) calculated pellet-to-clad gap at the end of the irradiation. Also, since larger gaps imply smaller effective gap conductances, the predicted temperatures for these pellets are higher.

In all cases, no cladding contact with the capsule wall is predicted at the pellet midplane throughout the irradiation. Table 7.1 indicates calculated clad-to-capsule diametral gaps of between 1.27 to 2.28 mils at the end of the irradiation.

Finally, it is of interest to note that while the pellet (centerline and mean) and capsule wall temperatures listed in Table 7.1 are lower for Capsule 4, the reverse is true for the cladding wall temperatures. This seeming paradox arises by a combination of factors. First, the LHGR of Capsule 13 (5.74 kW/ft) at this time is slightly higher than that (5.66 kW/ft) of Capsule 4, which causes the capsule 13 wall temperature to be higher (by 0.4°C). The fuel temperature is also higher, because in addition to the higher LHGR, the pellet-to-clad gap is larger and has a lower gap conductance (higher fission gas release). On the other hand, the clad-to-capsule gap is filled with helium, so here the gap conductance remains high in both capsules (the difference in gap widths having minor effect). In essence, the cladding wall temperature is lower in Capsule 13 because the difference in gap conductances between fuel and clad and between clad and capsule is greater for Capsule 13 than for Capsule 4.

7.4 Predicted Conditions for the Capsules in the Hot Cell

The final burnup advancement steps in each CARTS calculation represent conditions from the time that the capsules arrived at ORNL (April 2002) through the time that the fuel pins were opened (during the fuel pin gas pressure measurement). For these final calculation steps, the fuel pins are heated internally by decay power, while heat transfer from the outer capsule surface is by convection to the hot cell atmosphere.

Capsules 4 and 13 were introduced into the ORNL hot cell on April 22, 2002, about six weeks after completion of irradiation and their removal from the test assembly. The MOCUP protocol (coordinating calculations by MCNP and ORIGEN) was applied at INEEL to predict isotopic inventories and decay powers. During the period from mid-April to end-August, these results show that the pellet stack decay power fell from 4.0 to 1.7 watts (0.0080 to 0.0034 kW/ft). Fuel Pin 7 was opened on August 27 followed by Fuel Pin 16 on October 21.

The CARTS pre-PIE predictions for the capsule conditions at the expected time of opening were based on a decay power of 2.2 watts (0.0044 kW/ft), which corresponds to mid-July 2002

(~130 days after completion of irradiation). Heat transfer from the outer capsule surface is by free convection to the hot cell atmosphere. The natural convection heat transfer coefficient based on the capsule surface area directly over the pellet stack has been established as 27.5 W/m^2-°C (4.77 Btu/hr-ft^2-°F), based upon temperature measurements for the capsules examined in previous PIEs.

Table 7.2 presents the results of the CARTS calculations for conditions in the hot cell with decay heat corresponding to 170 days (0.0036 kW/ft) for Capsule 4 and 225 days (0.0032 kW/ft) for Capsule 13. The post-PIE calculated fuel temperatures are lower due to the lower decay heats at the time of capsule and fuel pin opening. Pre-PIE CARTS calculated results are given in red for comparison purposes.

Table 7.2. CARTS predictions for Capsules 4 and 13 under hot cell conditions

Capsule	Initial Pellet-Clad Clad-Capsule Gaps	Temperatures °C				Diametral gap (mil)		Fuel Pin Internal Pressure[1,2] psia
		Pellet Centerline	Pellet Mean	Clad Wall	Capsule Wall	Pellet-to-Clad	Clad-to-Capsule	
4	Minimum	43.3 45.6	43.2 45.5	42.2 44.7	42.1 44.6	2.41 2.14	1.45 1.73	121.9 66-196
	Maximum	43.6 45.8	43.5 45.7	42.2 44.8	42.1 44.6	3.31 3.04	2.25 2.53	108.1 66-196
13	Minimum	41.8 45.5	41.7 45.4	40.8 44.7	40.7 44.5	2.69 2.14	1.17 1.73	143.2 66-196
	Maximum	42.1 45.8	42.0 45.6	40.8 44.7	40.7 44.5	3.59 3.04	1.97 2.53	126.5 66-196

[1]Capsule 4/Fuel Pin 7, 114.8 psia (FPMA measurement)
[2]Capsule 13/Fuel Pin 16, 134.8 psia (FPMA measurement)

The fission gas release percentages employed in the post-PIE calculations for Capsule 4/Fuel Pin 7 and Capsule 13/Fuel Pin 16 are the PIE-measured 8.37% and 9.51%, respectively. Using "mean" initial gas gap dimensions, the helium release fraction was adjusted so that the post-PIE CARTS simulations would yield the same pressures [114.8 psia (Fuel Pin 7) and 134.8 psia (Fuel Pin 16)] as were measured via the FPMA (Section 4.5 of Volume 1). The final column of Table 7.2 indicates the predicted internal pressure within the fuel pins.

The pressure within the fuel pins (based on the combined volumes of the pellet-clad annular gap and the gas plenum associated with the actual stack length for these capsules) was predicted to be bounded between 66-196 psia in the pre-PIE CARTS simulations. The lower result was obtained by use of an assumed fission gas (krypton and xenon) release from the fuel matrix in accordance with the best estimate (4.2% at 45 GWd/MT) as discussed in Section 2.6.1.2 of the Quick Look Report. About 10.0 psi of the total pressure is contributed by helium created during the irradiation, half of which is assumed released to the fuel pin free volume. The higher result was obtained assuming an upper-limit fission gas release of ~16.7%.

At the time of capsule opening, the pellet-to-clad diametral gaps within the fuel pins are predicted to lie between 2.41 and 3.59 mils, a range of 1.18 mil. This range is higher than the pre-PIE predictions due to greater cladding creep. Within this calculated range, the individual gap widths associated with the 15 different pellets are determined by the relative width of each

pellet's initial cold diametral gap, which the design tolerances allow to lie between 2.0 and 3.5 mils.

From Section 5.2.5, the observed pellet diameter for Fuel Pins 7 and 16 ranged from 0.3258 to 0.3278 inches; the CARTS predicted pellet diameter ranged from 0.3270 to 0.3275 inches. For the pellet-to-clad diametral gap, CARTS predicts 2.41 to 3.59 mils at the pellet midplane; the measured equivalent gaps (Table 5.7) were 1.47 to 2.29 mils radial (2.94 to 4.58 mils diametral).

The diametral gap between the outer surface of the Zircaloy cladding and the inner surface of the stainless steel capsule is predicted to lie in the range from 1.17 to 2.25 mils (less than pre-PIE predictions due to greater outward cladding creep). The as-built tolerances for the cold clad-to-capsule initial diametral gap vary between 2.2 and 3.0 mils.

7.5 Summary and Conclusions from the CARTS Predictions

The results of the pre- and post-PIE calculations for Capsules 4 and 13 are summarized in Tables 7.1 and 7.2. Table 7.1 provides a comparison of the two sets of CARTS predictions for the period just prior to the end of the Phase IV-Part 1 irradiation. Table 7.2 compares the predictions under hot cell conditions. In general, the predictions obtained in advance of the PIE are found to have been reasonably accurate.

For Capsules 4 and 13 with burnups of 40 GWd/MT, the CARTS code predicts that the 15 pellets within each fuel pin exhibit, under hot cell conditions, individual pellet-to-clad diametral gap widths ranging from 2.41 to 3.59 mils. (Where internal cracks are present, the diametral gap is defined to include the free area within these open cracks.)

Contact with cladding at the pellet midplane is not predicted to have occurred at any time during the irradiation. Progressively increased cladding diameters have been observed in this and previous PIEs. This outward movement of the cladding adjacent to the pellet midplane is believed due to irradiation-induced creep under the impetus of internal gas pressure (see Chapter 6).

The diametral gap between the fuel pin and capsule is predicted to lie between 1.17 and 2.25 mils, which may be compared to the range of 2.2–3.0 mils for the initial cold capsule conditions.

The gas pressures within the fuel pins when opened in the hot cell were predicted to be between 66 and 196 psia. The measured fuel pin pressures were 114.8 and 134.8 psia, respectively, for Fuel Pin 7 and 13.

Fuel Pins 7 and 13 experienced more cladding creep than calculated in the pre-PIE simulations, but higher fuel thermal expansion offset this effect, yielding essentially the same pellet-to-clad gaps in the post-PIE CARTS calculations.

The most significant difference between the pre- and post-PIE CARTS calculations is the higher predicted fuel temperatures (by 160–270°C) in the post-PIE simulations. The difference is primarily caused by use of a new MOX fuel thermal conductivity correlation (Reference 51) that yields a lower fuel conductivity for the same temperature and burnup.

8. CONCLUSIONS

1. Mixed-oxide (MOX) fuel prepared with plutonium derived from weapons components has been irradiated to 40 GWd/MT under conditions more severe than will be encountered by Mission Fuel. Gallium is present within the test fuel at 1–5 PPM, much more than will be present in Mission Fuel.

2. The fuel examined in the current PIE experienced (during Phase II of the irradiation) LHGRs near 11 kW/ft. These are the highest LHGRs to be imposed on any capsules during this test irradiation. The associated pellet centerline temperatures are calculated to have exceeded 1600°C during Phase II. Evidence that fuel temperatures were in excess of 1200°C is provided by the axial smearing of the gamma-ray activity profile, a classic indication of the axial migration of Cs-137 (which is immobile at lower temperatures).

3. The release of fission gas is largely controlled by diffusion of the gas atoms, whose mobility (diffusivity) increases exponentially with temperature. Thus, fission gas release fraction is largely determined by the maximum temperature experienced by the fuel. The centerline temperatures of the current test fuels exceeded the Halden Threshold during irradiation and hence fission gas release in excess of one percent is to be expected. The actual fission gas release (about 9%) corresponds to the European experience for MOX fuel operated at axial powers (LHGRs) as high as those that have been imposed during this test irradiation.

4. The MOX test fuel was fabricated with a MIMAS-type process involving use of a master-mix produced by milling together all of the PuO_2 with a greater mass of UO_2. (This consumes only a small fraction of the total UO_2.) The milling produces an intimate mixing, but also modifies the powder physical characteristics (surface area, density, flowability) while electrostatic forces induce self-agglomeration. After milling, the master-mix was diluted (mixed) into the remainder of the UO_2 to form the secondary blend, from which the pellets were pressed. This secondary blending was less effective than intended in dispersing the master-mix into the UO_2 matrix. Consequently, a few relatively large residual agglomerates (clumps of master-mix) are evident in the irradiated fuel.

5. At 40 GWd/MT average fuel burnup, local burnups are about 100 GWd/MT within the agglomerates and only about 28 GWd/MT in the surrounding UO_2 matrix. Corresponding fuel lattice swelling (at 0.7% per 10 GWd/MT) is 2.8% overall, with 7% in the agglomerates and 2% in the UO_2 matrix. For agglomerates transformed to the high-burnup structure in the cooler outer regions of the pellet, gas escaping from the lattice is retained in local porosity, causing an additional local swelling of as much as 40%. Thus, the gas-retaining agglomerates visible in the current PIE have swollen by as much as 50% from their initial (preirradiation) sizes. For the largest single equivalent diameter now measured at 600 microns, this indicates an initial value of about 524 microns. Existence of a few particles with this initial size is consistent with the preirradiation measurements for this fuel.

6. Literature values for modern European commercial fuels indicate postirradiation agglomerate maximum equivalent diameters in the 250–400 micron range for fuel average

burnups in the vicinity of 45 GWd/MT. The current PIE results (and the measured preirradiation sizes) indicate that this test fuel began irradiation with a greater fraction of large agglomerates than is normally encountered in modern mixed-oxide fuels. Nevertheless, the subsequent swelling during irradiation has been in the proportions expected for the current burnup, and there have been no performance problems with the fuel. In particular, the fission gas release has been no greater than that expected from the European experience.

7. The halos surrounding each of the agglomerates are clear regions distinct from both the fuel matrix and the high-burnup structure. These regions are visible because athermal (fission recoil) diffusion of fission products from the agglomerate has altered the adjacent matrix in a manner that responds differently to polishing. Agglomerates of widely varying sizes display the halo, which comprises very small (nanometer-size) gas bubbles within the adjoining low-burnup UO_2 matrix grains. The presence of xenon in these regions has been confirmed by EPMA measurements in the current PIE.

8. The beginnings of high-burnup structure transformation for agglomerates in the central pellet region are first observed in the current PIE. Transformation requires locally high burnups at temperatures less than 1000°C. Temperatures this low did not prevail in this region until after irradiation Phase II (fuel average burnups > 20 GWd/MT). This explains the late appearances of these agglomerate outlines.

9. As succinctly stated in Reference 22 (Section 4.2, p. 178), "When stress is applied to a metal, it creeps, even if this creep rate is very slow. When this occurs under neutron flux, a much greater strain rate is observed at temperatures where thermal creep is not even measurable." Figure 4.26 of the companion PIE observations report (Reference 39) illustrates the radial displacement of Fuel Pin 16 at an internal pressure of about 135 psia. The corresponding wall hoop stress is about 5.4 MPa, and measurements before and after depressurization demonstrate the expansion of the cladding diameter at such low stresses. When the wall is strained in an irradiation field, creep will follow.

10. The test fuel pin cladding diameter has expanded by about 0.84 mil at 40 GWd/MT, an increase of 0.22%. This irradiation-induced outward creep occurred under the impetus of a tensile wall (hoop) stress that increased from zero to a little more than five MPa as fuel pin internal pressure increased during the irradiation. Although information on outward cladding creep is limited (most interest lies in creep down), some data are found as discussed in Section 6.3. As shown in Figure 6.5, the creep observed in the current test irradiation is compatible with the experience documented in the available literature.

11. ABAQUS code finite-element calculations performed for the zero-burnup initial heatup with as-built dimensions for the pellet, fuel pin, and capsule, and with the actual initial linear heat generation rate are documented for the 30-GWd/MT withdrawal in Chapter 6 of Reference 37. These calculations (not repeated for the 40 GWd/MT withdrawal) clearly predict pellet hourglassing (due to a greater axial thermal expansion along the pellet centerline) with cladding contact at the pellet ends. The applied stress is sufficient to induce local yielding. This explains the small local cladding deformations ("primary ridges") measured in the PIEs.

12. The empirical creep correlation (Equation 6-5) described in Section 6.4 represents adequately the outward relocation of the MOX test fuel pins. This correlation will be employed for the pre-PIE CARTS code predictions for the capsules to be withdrawn at 50 GWd/MT burnup.

13. The uneven and noncontiguous nature of the corrosion observed on the cladding inner surfaces is an artifact of the manner in which the pellet fragments came into contact with the cladding during irradiation. Inner surface oxidation requires that excess oxygen be available and that the fuel be in contact with the cladding to provide a path for solid-state athermal diffusion of the oxygen atoms. The thicker oxidation layers over the agglomerates follow directly from the narrower local pellet-clad gaps during irradiation. The observed clad corrosion patterns are in accordance with expectations based on the European experience.

14. The CARTS code FRAPCON-based calculations for the 40 GWd/MT Capsules 4 and 13 have been repeated with code input adjusted as necessary to conform to the current PIE results:

    a. Fuel densification is specified as 2.0% densification complete by 10.0 GWd/MT burnup. This model, first used in the previous (30 GWd/MT) PIE, was also found accurate for the 40 GWd/MT fuel pins.

    b. The burnup-dependent fission gas release fraction representation has been set to match the observations (at 40 GWd/MT) of 8.4% for Capsule 4 and 9.5% for Capsule 13.

    c. The models for clad diameter increase have been modified to reflect the observed clad expansion (Item 10 above).

    d. The CARTS predictions for capsule conditions in the hot cell obtained in advance of the PIE are found to have been reasonably accurate. The new CARTS calculations predict fuel structural dimensions that agree closely with the PIE observations.

15. The behavior of this weapons-derived fuel, evaluated at a burnup of 40 GWD/MT, is similar to the European experience with reactor-grade MOX fuel.

16. Nothing in the PIE findings challenges the adequacy of the existing safety analyses for irradiation of the remaining test capsules to 50 GWd/MT or beyond.

9. REFERENCES

1. R. N. Morris, C. A. Baldwin, and C. M. Malone, *MOX Fission Gas Pressure Measuring Apparatus*, ORNL/MD/LTR-176, Oak Ridge National Laboratory, January 2000.

2. J. A. Turnbull et al., *Measurement of ^{85}Kr As A Method For Assessing Fission Gas Release in CAGR Fuel Pins*, Nuclear Fuel Performance, BNES, 319–325, London, 1985.

3. S. A. Hodge, *Effects of Fission Gas Release and Pellet Swelling Within the LWR Mixed-Oxide Irradiation Test Assembly*, ORNL/MD/LTR-83, Revision 1, Oak Ridge National Laboratory, November 1997.

4. R. N. Morris and D. W. Heatherly, *MOX Fuel Pin Volume Measuring Apparatus*, ORNL/MD/LTR-232, Oak Ridge National Laboratory, September 2002.

5. Personal Communication. The estimated glove box conditions for the sealing of Fuel Pins 7 and 16 were provided by M. Bowidowicz (LANL Staff) on November 1, 2002.

6. P. Blanpain et al., *Recent Results From The In Reactor MOX Fuel Performance in France and Improvement Program*, Proceedings of the 1997 International Topical Meeting on LWR Fuel Performance, Portland, Oregon, March 1997, **American Nuclear Society,** 1997, pp. 39–45.

7. Y. Guerin et al., *Microstructure Evolution and In-Reactor Behaviour of MOX Fuel*, LWR Fuel Performance Conference, Park City Utah, April 10–13, 2000.

8. I. Kamimura et al., *Helium Generation and Release in MOX Fuels*, IAEA Symposium "MOX Fuel Cycle Technologies for Medium and Long Term Deployment," Vienna, 17–21 May 1999.

9. Takeshi Mitsugi et al., *Behavior of MOX Fuel Irradiated in a Thermal Reactor*, Proceedings of the 1997 International Topical Meeting on LWR Fuel Performance, Portland, Oregon, March 1997, **American Nuclear Society**, 1997, pp. 54–61.

10. R. N. Morris and C. A. Baldwin, *CCCTF Trap Table Calibration Curve for Krypton-85 Activity Determination*, ORNL/MD/LTR-246, Oak Ridge National Laboratory, June 2003.

11. "The Chemical Effects of Composition Changes in Irradiated Oxide Fuel Materials," Davies and Ewart, **Journal of Nuclear Materials**, 41 (1971), 143–155.

12. "Oxygen Potential in the Rim Region of High-Burnup UO_2 Fuel," Hj. Matzke, **Journal of Nuclear Materials**, 208 (1994), 18–26.

13. C. T. Walker, W. Goll, and T. Matsumura, *Further Observations on OCOM MOX Fuel; Microstructure in the Vicinity of the Pellet Rim and Fuel-Cladding Interaction*, **Journal of Nuclear Materials**, 245 (1997), 169–178,

14. "Internal Corrosion Layer in PWR Fuel," Lionel Desgranes, **OECD Proceedings, Seminar on Thermal Performance of High Burn-up LWR Fuel**, 3–6 March 1998, CEA, Cadarache, France, 187–195.

15. W. Goll et al., *Irradiation Behavior of UO_2/PuO_2 Fuel in Light Water Reactors*, **Nuclear Technology**, 102, April 1993, 29–46.

16. C. Vitanza et al., *Fission Gas Release From UO_2 Pellet Fuel at High Burn-up*, ANS Topical Meeting on Light Water Reactor Fuel Performance, Portland, Oregon, 29 April–3 May 1979.

17. W. Wiesenack, "Issues Related to High Burnup Utilization, and Experimental Results from the OECD Halden Reactor Project," Colloquium on High Burnup Fuels for LWRs: Benefits and Limitations, Massachusetts Institute of Technology, Cambridge, MA, January 23, 2003.

18. D. G. Kolman, M. E. Griego, C. A. James, and D. P. Butt, *Thermally Induced Gallium Removal From Plutonium Dioxide for MOX Fuel Production*, **Journal of Nuclear Materials**, 282 (2000), 245–254.

19. R. N. Morris, J. Giaquinto, and S. A. Hodge, *MOX Average Power Test Fuel Pellet Initial Gallium Content*, ORNL/MD/LTR-182, Oak Ridge National Laboratory, March 2000.

20. C. T. Walker, W. Goll, and T. Matsumura, *Effect of Inhomogeneity on the Level of Fission Gas and Cesium Release from OCOM MOX Fuel During Irradiation*, **Journal of Nuclear Materials**, 228 (1996), 8–17.

21. S. B. Fisher et al., *Microstructure of Irradiated SBR MOX Fuel and Its Relationship to Fission Gas Release*, **Journal of Nuclear Materials**, 306 (2002), 153–172**.**

22. H. Bailly, D. Menessier, and C. Prunier, Eds., *The Nuclear Fuel of Pressurized Water Reactors and Fast Reactors—Design and Behaviour*, Lavoisier Publishing Inc., Secaucus, NJ, 1999.

23. P. Blanpain, C. Callens, G. Chiarrelli, J. Guillet, and W. Goll, *MOX Fuel Performance and Development*, European Nuclear Society TOPFUEL Meeting, Stockholm, May 2001.

24. M. D. Freshley et al., *Behavior of Discrete Plutonium-Dioxide Particles in Mixed-Oxide Fuel During Rapid Power Transients*, **Nuclear Technology**, 15 August 1972, p. 239.

25. T. Abe, N. Nakae, K. Kodato, M. Matsumoto, and T. Inabe, *Failure Behavior of Plutonium—Uranium Mixed Oxide Fuel Under Reactivity-Initiated Accident Condition*, **Journal of Nuclear Materials**, 188 (1992), 154–161.

26. Draft ASTM Designation C 833–95a, "Standard Specification for Sintered (Uranium-Plutonium) Dioxide Pellets," dated November 2000.

27. Appendix D of *Fuel Qualification Plan* prepared by Framatome ANP for U.S. Department of Energy dated April, 2001.

28. B. S. Cowell, *Technical Specification: Mixed-Oxide Pellets for the Light-Water Reactor Irradiation Demonstration Test*, ORNL/MD/LTR-75, June 1997.

29. G. S. Chang, *Pu-rich MOX Agglomerate-by-Agglomerate Model for Fuel Pellet Burnup Analysis*, to be published, 2004 International Congress on Advances in Nuclear Power Plants, Pittsburgh, PA, June 13–17, 2004.

30. R. Manzel and C. T. Walker, *EPMA and SEM of Fuel Samples from PWR Rods with an Average Burn-up of Around 100 MWd/kg HM*, **Journal of Nuclear Materials**, 301 (2002), 170–182.

31. R. N. Morris et al., *MOX Average Power Intermediate PIE: 21 GWd/MT Final Report*, ORNL/MD/LTR-199, Oak Ridge National Laboratory, December 2000.

32. R. N. Morris et al., *MOX Average Power 30 GWd/MT PIE: Final Report*, ORNL/MD/LTR-212, Volume 1, Oak Ridge National Laboratory, November 2001.

33. L. Caillot et al., *Analytical Studies of the Behaviour of MOX Fuel*, Proceedings of the 1997 International Topical Meeting on LWR Fuel Performance, Portland, Oregon, March 1997, **American Nuclear Society**, 1997, pp. 62–69.

34. Personal Communication. These differences were noted by Mr. Tom Blair, who directly supervised the preparation of the MOX test fuel at Los Alamos National Laboratory.

35. R. E. Woodley, *Variation in the Oxygen Potential of a Mixed-Oxide Fuel with Simulated Burnup*, **Journal of Nuclear Materials**, 74 (1978), 290–296.

36. H. R. Peters and J. L. Harlow, "The Effect of the Trace Impurity Uranium on PWR Aqueous Corrosion of Zircaloy-4," *Zirconium in the Nuclear Industry: Eleventh International Symposium, ASTM STP 1295*, E. R. Bradley and G. P. Sabol, Eds., American Society for Testing and Materials, 1996, pp. 295–318.

37. S. A. Hodge, L. J. Ott, F. P. Griffin, and C. R. Luttrell, *Implications of the PIE Results for the 30-GWd/MT-Withdrawal MOX Capsules*, ORNL/MD/LTR-212, Volume 2, Rev. 1, Oak Ridge National Laboratory, February 2002.

38. R. N. Morris et al., *MOX Average Power Early PIE: 8 GWd/MT Final Report*, ORNL/MD/LTR-172, Oak Ridge National Laboratory, November 1999.

39. R. N. Morris et al., *MOX Test Fuel 40 GWd/MT PIE: Final Report*, ORNL/MD/LTR-241, Volume 1, Oak Ridge National Laboratory, August 2003.

40. R. N. Morris and C. A. Baldwin, *MOX Fuel Pin Measuring Apparatus*, ORNL/MD/LTR-209, Oak Ridge National Laboratory, March 2001.

41. R. N. Morris et al., *MOX Average Power Test 30 GWd/MT PIE: Quick Look*, ORNL/MD/LTR-208, Oak Ridge National Laboratory, February 2001.

42. Image-Pro Plus, Version 4.1, Media Cybernetics, 8484 Georgia Avenue, Silver Spring, Maryland 20910.

43. S. A. Hodge, *Fission Gas Release and Pellet Swelling Within the Capsule Assembly During Phase IV of the Average Power Test*, ORNL/MD/LTR-184, Oak Ridge National Laboratory, July 2000.

44. *ESCORE—The EPRI Steady-State Core Reload Evaluator Code: General Description*, EPRI NP-5100, Combustion Engineering, Inc., Windsor, Connecticut, February 1987.

45. G. A. Berna et al., *FRAPCON-3: A Computer Code for the Calculation of Steady-State Thermal-Mechanical Behavior of Oxide Fuel Rods for High Burnup*, NUREG/CR-6534, December 1997.

46. C. Ronchi and C. T. Walker, *Determination of Xenon Concentration in Nuclear Fuels by Electron Microprobe Analysis*, **J. Phys. D: Appl. Phys.**, 13 (1980), 2175–84.

47. M. A. McGrath, *In-Reactor Creep Behavior of Zircaloy Cladding*, International Topical Meeting on LWR Fuel Performance, American Nuclear Society, Park City, Utah, April 10–13, 2000.

48. A. Soniak et al., "Irradiation Creep Behavior of Zr-Base Alloys," *Zirconium in the Nuclear Industry: Thirteenth International Symposium*, ASTM STP 1423, G. D. Moan and P. Rudling, Eds., ASTM International, 2002, pp. 837–862.

49. M. Limback and T. Andersson, "A Model for Analysis of the Effect of Final Annealing on the In- and Out-of-Reactor Creep Behavior of Zircaloy Cladding,"

Zirconium in the Nuclear Industry: Eleventh International Symposium, ASTM STP 1295, E. R. Bradley and G. P. Sahol, Eds., American Society for Testing and Materials, 1996, pp. 448–468.

50. R. N. Morris et al., *MOX Average Power Test 40 GWd/MT PIE: Quick Look,* ORNL/MD/LTR-236, Oak Ridge National Laboratory, November 2002.

51. D. D. Lanning and C. E. Beyer, Revised UO_2 Thermal Conductivity for NRC Fuel Performance Codes, ANS Proceedings, Hollywood, Florida, June 2002.